PhD-FSTM-2024-090

Faculty of Science, Technology and Medicine

DISSERTATION

Defence held on 30^{th} October 2024 in Luxembourg

to obtain the degree of

DOCTEUR DE L'UNIVERSITE DU LUXEMBOURG

EN PHYSIQUE

by

Joana Andreia Ferreira Machado

Born on 15^{th} May 1995 in Pombal (Portugal)

Degradation Study of Co-evaporated Methylammonium Tin Iodide

Dissertation Defence Committee:

Prof. Alex Redinger, dissertation supervisor
Université du Luxembourg

Prof. Andreas Michels, chair
Université du Luxembourg

Prof. Susanne Siebentritt, vice-chair
Université du Luxembourg

Dr. Selina Olthof
Universität zu Köln

Dr. Robin Ohmann
Universität Siegen

"Unless someone like you cares a whole awful lot,
Nothing is going to get better. It's not."

– Dr. Seuss, The Lorax, 1971

"A menos que alguém como tu se preocupe a valer,
Nada vai mudar. Podes crer."

– Dr. Seuss, O Lórax, 1971

Acknowledgements

There are no words capable of describing how grateful I am for these four years of PhD. Being able to work in a laboratory and to meet so many awesome people, was a blessing.

First and foremost, I would like to thank my supervisor Prof. Alex Redinger. Thank you for having given me this opportunity and for having believed in me more than myself. In the hardest times, when experiments did not work, you always knew what to say, so that it would look brighter. Thank you for your time, your guidance, your feedback and for leaving me the freedom for experimentation. I am happy to have been part of the SPM group.

To Prof. Susanne Siebentritt, for your advices during the PV meetings and outside, for having accepted to be part of my PhD defense committee and specially for being such a role model as a scientist and as a woman, a big thank you. You truly are an inspiration for me.

To Prof. Phillip Dale, thank you for all the suggestions you gave me related to my PhD project and science communication. I am glad for being part of the "Energy Balance" team. Thanks to you I discovered science communication, which later became one of my favorite activities.

Thank you to my PhD CET members, Prof. Andreas Michels and Dr. Robin Ohmann for having followed me throughout the PhD and for the insightful questions you asked, that made me think further. Thank you Dr. Selina Olthof for accepting to be part of my PhD thesis committee and for your feedback.

Thank you Dr. Bernd Uder, Dr. Ulrich Siegel, Robert Himelrick and Nicolas Tournier for all the technical support. You were always ready to help me, even when I would come to your office knowing what I needed, but without any idea of how to make it happen.

To the SPM group, Jeremy and the alumni, Thibaut, Joe, Christian, Evandro, Jonathan and Himanshu, thank you for having shared your knowledge with me. Your help was essential during my PhD. Evandro, Jonathan, Uzair and Anastasios we had so many discussions, some

were insightful, others were just funny. You made me look at the world in such a different way. Thank you for contributing to my critical thinking. Elham and Mirco, I am so happy you joined the group! I hope you have fun there. Thank you all of you for your help and feedback during the rehearsals.

To the LPV and LEM groups, thank you for having welcomed me in your offices and labs. Michelle, Ricardo, Aline and Clara thank you for the time you spent helping me with different measurements in your labs.

A special thanks to Linda, my friend and mentor in science communication and in life. I am so grateful that our paths crossed. Aline and Louis, I was so lucky to have met both of you during my PhD. Thank you for the emotional support, the cakes, the discussions and all the fun that I had with you.

Cidália e Madrinha, quero-vos agradecer pela vossa presença e apoio durante o meu doutoramento. Podemos passar algum tempo sem dar notícias, mas mais tarde ou mais cedo sempre arranjamos um tempinho.

Obrigada à família Poeira por toda a voça ajuda. O vosso suporte foi essencial durante este meu percurso.

À minha mãe, ao meu pai e aos meus irmãos, obrigada pelo vosso amor e suporte incondicional. Mãe, obrigada pelos teus telefonemas, deram me muita força nestas últimas semanas. Pai, tu estás sempre pronto a ajudar, sei que se precisar tu vais lá estar. Meninos, muito obrigada por todos os abracinhos que me deram, eles trouxeram uma alegria enorme na minha vida. Diana, obrigada por teres arranjado maneira de me vir ver, quanto eu não pude ir ter contigo.

Finalmente, Ricardo, sem ti nada disto teria sido possível. Estiveste sempre lá ao meu lado. Sempre pronto para me apoiar e dar coragem. Viste tudo, os melhores e os piores momentos. Tenho imensa sorte em te ter na minha vida. Mal posso esperar para pelas nossas próximas aventuras.

Contents

Acronyms

HOIP Hybrid organic-inorganic metal halide perovskite

Pb Lead

Sn Tin

$MASnI_3$ Methylammonium tin iodide

GHG Greenhouse gas

PV Photovoltaic

CIGS Copper Indium Gallium Selenide

CdTe Cadmium Telluride

UHV Ultrahigh vacuum

PCE Power conversion efficiency

$CaTiO_3$ Calcium titanate

$MAPbI_3$ Methylammonium lead iodide

PVD Physical vapor deposition

CVD Chemical vapor deposition

MAI Methylammonium iodide

QCM Quartz crystal microbalance

$FAPbI_3$ Formamidinium lead iodide

XRD X-ray diffraction

UV-vis Ultraviolet-visible

AFM Atomic force microscopy

KPFM Kelvin probe force microscopy

XPS X-Ray Photoelectron Spectroscopy

DMSO Dimethylsulfoxide

DMF Dimethylformamide

TGA Thermogravimetric analysis

FWHM Full width at half maximum

PMMA Poly(methyl methacrylate)

V_{AC} AC voltage

CPD Contact potential difference

e elementary charge

PL Photoluminescence

$\mathbf{(PEA)_2SnI_4}$ Phenethylammonium tin iodide

PEAI Phenethylammonium iodide

Abstract

Hybrid organic-inorganic metal halide perovskites (HOIPs) have been under the spotlight since they were first used for solar cell applications. Since then, the power conversion efficiency of HOIP-based solar cells has increased significantly and the current record is 26.7 % on the laboratory scale [1], which is comparable to the record of more mature technologies such as silicon solar cells. Furthermore, HOIP solar cells are a low-cost alternative that is relatively easy to produce and can be easily adapted by changing the substrate or composition. The major drawbacks of HOIP based solar cells are that they tend to degrade when exposed to external stresses, and record efficiency devices contain lead (Pb). The latter may hinder the commercialization of this technology, because of the toxicity of Pb, which is of great concern to human health and the environment. A possible way to avoid Pb in HOIP-based solar cells is to replace it with tin (Sn). Which is a less toxic substitute for Pb and it is placed right above Pb in the periodic table, meaning that both elements have similar reactivity. Furthermore, Sn-based perovskite solar cells were demonstrated and yielded the best results in terms of stability and efficiency for Pb-free HOIPs. Nevertheless, Sn-based HOIPs are also prone to degradation under external stimuli and present an additional challenge compared to Pb-based perovskites: Sn is more prone to oxidation.

In this thesis, Sn-based HOIP, more specifically methylammonium tin iodide ($MASnI_3$) is synthesized using physical vapor deposition, as it is a solvent-free technique. The $MASnI_3$ films were exposed in a controlled environment to different external stimuli, such as light, water, and synthetic air in order to study the different degradation pathways. Light, air,

and water have been shown to degrade $MASnI_3$, but the degradation pathway is different for each of them. First, light-induced degradation is shown to result in the formation of majorly SnI_2, while the organic component leaves the surface. Second, water-induced degradation also mainly forms SnI_2, but further degradation into SnO_2 was observed. Third, synthetic air-induced degradation is shown to form SnO and an intermediate phase that was assumed to combine tin, iodine, and oxygen. Finally, the formation of SnI_4 was not detected for any of the stimuli, contrary to what is described in the literature.

Chapter 1

Introduction

Energy is deeply embedded in the functioning of modern society and is an essential element of daily life. From the electricity that lights our homes and charges our devices to the fuel that is used in transportation, energy enables everything from basic needs, such as a refrigerator at home, and advanced technologies, used for example by industries or in health care systems. Energy consumption has continued to increase since the industrial revolution. Currently, the yearly consumption is estimated to be 180 000 TWh, as shown in Figure 1.1, and is expected to increase further as more households gain access to basic energy needs [2, 3].

However, a large part of the currently used energy comes from the burning of fossil fuels (see Figure 1.1), which produces greenhouse gases (GHGs) such as carbon dioxide (CO_2) and methane (CH_4). GHGs are problematic because they stay in the atmosphere, reducing the quality of air and also contributing to climate change, which is usually quantified using the increase in temperature [4]. This leads to other phenomena such as a more frequent extreme weather events, the loss of ecosystems, and the rise of sea level. In a collective effort to mitigate climate change, 196 parties signed the Paris agreement in 2016, in which it is stated that temperatures should be kept "well below 2 °C" above pre-industrial temperatures

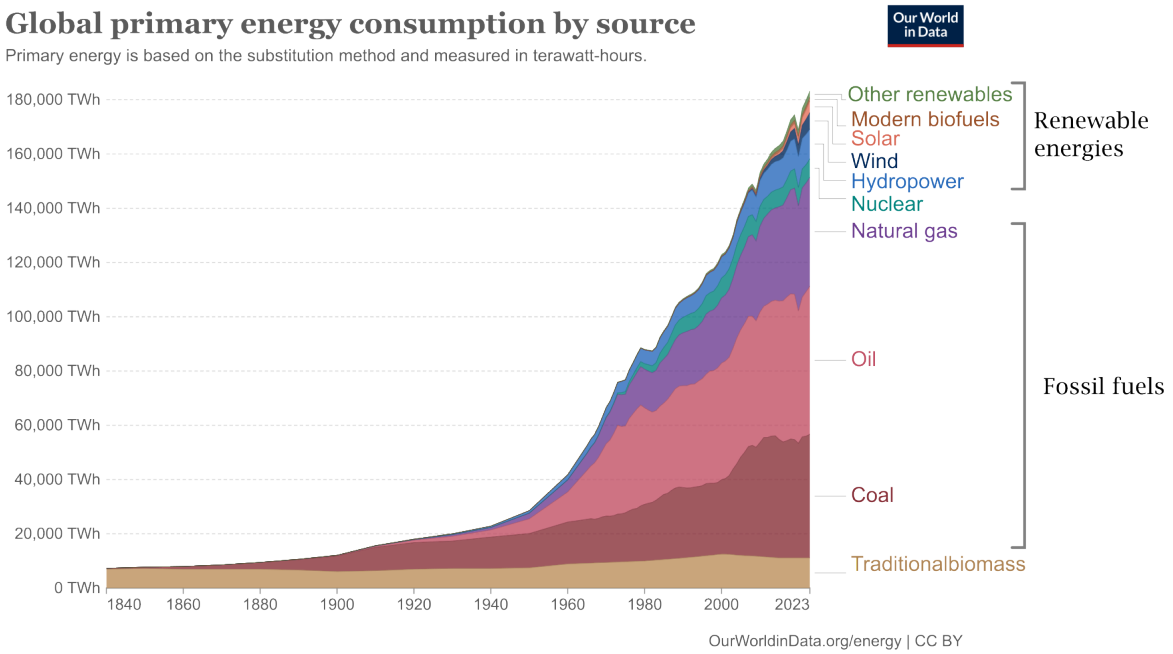

Figure 1.1: Energy consumption over time and its primary source [2].

and preferentially below 1.5 °C. In 2023 the temperature was already at 1.45 °C above pre-industrial levels [5].

Therefore, it is of great importance to continue to increase efforts to mitigate climate change and reduce GHGs emissions. This can be done by using renewable energy as the primary energy source, reducing and optimizing the consumption of energy, and by capturing GHGs, so that they can be stored in the long term.

Solar cells have proven to be a key element in this race to minimize the generation of GHGs. Their technology uses the photovoltaic (PV) effect, where a semiconductor layer (which is also called an absorber) absorbs incident light and converts it into electricity. These devices do not generate any GHGs during use. Solar cell technologies are categorized into three generations [6]. The first generation consists of thicker solar cells, such as polycrystalline and monocrystalline silicon cells. The second generation focuses on the thin-film solar cells, such as copper indium gallium selenide (CIGS) and cadmium telluride (CdTe). These devices have the advantage of requiring less material and have the potential of being of lower cost

compared to the first generation. Finally, the third generation of solar cells makes use of emerging materials, such as quantum dots or perovskites. They can target a large number of characteristics such as being low-cost, highly efficient, or easy to integrate into buildings.

The perovskites solar cells have been of special interest in the last decade, as it is a low-cost technology that is relatively easy to produce and, on the laboratory scale, can convert light into electricity in quantities comparable to those of more mature technologies such as silicon solar cells. Their main drawbacks are the low stability when exposed to external stresses and also the use of lead (Pb) in the record-breaking solar cells. Nevertheless, tin (Sn) can be used as a substitute for Pb in perovskites. This would be the logical choice because Sn is placed right above Pb in the periodic table, meaning that both materials have similar valence shells and similar reactivity. Nevertheless, the choice of Sn comes with a new major challenge, which is the tendency of Sn to oxidize, reducing the stability of the absorber. That is the main focus of this thesis, where Sn-based perovskite absorbers were exposed to different individual stresses in an attempt to understand their degradation pathway.

In Chapter 2, the background and state-of-the-art in terms of perovskites are presented. More specifically, the chapter starts with the basics of perovskites. Then a review of the literature is discussed in terms of perovskite degradation pathways and measurement techniques.

Chapter 3 summarizes the materials and the methods that were used in this work. Furthermore, it contains a detailed explanation of the analysis procedure for the quantitative composition measurement.

Then, in Chapter 4, the synthesis of Sn-based perovskites is discussed, with an emphasis on the importance of the growth conditions and the choice of precursor materials.

This is followed by four chapters on the degradation of the perovskite film. Namely, in Chapter 5 the focus is on the degradation that may be caused by the measurement of the samples. There, the sample is repeatedly measured in ultrahigh vacuum (UHV) in order to determine whether the UHV conditions and X-rays can degrade the sample.

Then, Chapter 6 discusses the light-induced degradation in Sn-based perovskites. Where a sample was exposed to 61 h of light in order to understand its degradation pathway.

The degradation induced by water on the $MASnI_3$ is studied in Chapter 7. There, different samples were individually exposed to liquid water or water vapor.

The last kind of external stress is synthetic air and is studied in Chapter 8. This chapter, uses the knowledge acquired in the previous chapter, to study the degradation caused by synthetic air (i.e. clean air without moisture). The degradation induced by air is also compared with the degradation induced by water.

The final chapter (Chapter 9) summarizes this thesis' main contributions and discusses further research that can be done to improve the stability of Sn-based perovskites.

Chapter 2

Literature review

Perovskite structure materials have been known since 1839 and have attracted attention because of their multifaceted properties. In fact, depending on their composition, they can have completely different physical properties such as being conductors, insulators, superconductors, or semiconductors [7–10]. Nevertheless, it was only in 2009 that the first perovskite solar cell was created by Kojima et al. [11]. The percentage of sunlight energy that the cell converts into usable electrical energy, known as the power conversion efficiency (PCE) of this cell, was only 3.8%, but it attracted the solar cell community due to its relatively inexpensive and easy way of production. Since then, research on perovskite solar cells has surged, and now, 15 years later, the PCE of perovskite solar cells on the laboratory scale has increased to 26.1% [1, 12, 13]. This is very close to solar cells made with silicon, which is a more mature material in the context of solar cells, where the record PCE is 27.1% also in the laboratory scale [1, 14].

2.1 Perovskite: the structure and the absorber

2.1.1 The perovskite structure

The first material to ever be named "perovskite" was calcium titanate ($CaTiO_3$). This mineral was first studied in 1839 by Gustav Rose and had a crystalline structure that no one had previously reported [15, 16]. Rose named the mineral perovskite after the mineralogist Lev Alekseyevich von Perovski. Figure 2.1 shows a picture of $CaTiO_3$ taken by Katz [15].

Figure 2.1: $CaTiO_3$ perovskite sample, from [15].

Today, the name "perovskite" refers not only to the mineral $CaTiO_3$, but also to other materials that have the same crystalline structure (see Figure 2.2). That is, the composition of the crystal is ABX_3, where A and B are cations, and X is an anion. The typical perovskite has a cubic structure. The arrangement of the ions is such that six X anions surround the smaller B cation. This structure can be described as an octahedron. The X octrahedra connect to each other at the corners, forming a cube that, in turn, contains the larger cation at the center.

In order for this structure to occur, two major requirements should be met: 1) the relative size and 2) the charge balance of the ions [18]. Starting with the relative size of the ions, the Goldschmidt tolerance factor and the octahedral factor are often used to estimate

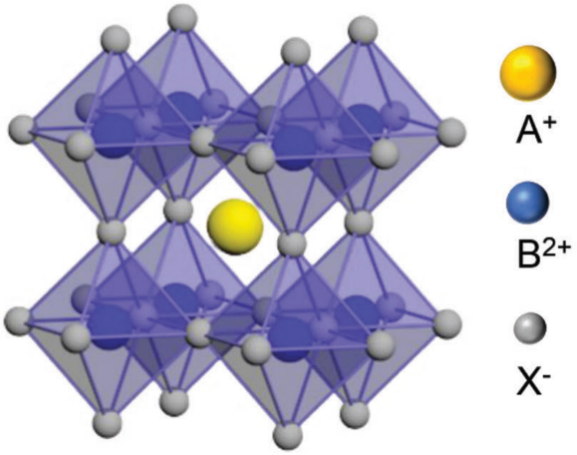

Figure 2.2: Perovskite crystal structure taken from [17].

whether certain ion combinations can form a stable perovskite. The Goldschmidt tolerance factor t takes into account the cube geometry and the radii of each ion. It is given by

$$t = \frac{R_A + R_X}{\sqrt{2}(R_B + R_X)} \tag{2.1}$$

Where R_A, R_B and R_X are the radii of A, B, and X, respectively. A value of t between 0.8 and 1, means that there is a high probability of forming perovskite phase. Values outside this range form other topologies like ilmenite or hexagonal structures [18, 19]. To complement this parameter, the octahedron parameter μ estimates whether the cation B fits in the anion octahedron, it is given by

$$\mu = \frac{R_B}{R_X}. \tag{2.2}$$

In terms of charge balance, the material should be electrically neutral, meaning that the negative charge of the anion should compensate for the charge of the cations. This can be expressed as

$$q_A + q_B = 3q_X. \tag{2.3}$$

When q_A, q_B and q_X are the charges of A, B, and X, respectively. By integrating different elements into the perovskite crystal structure, it is possible to create materials with a variety of properties, such as superconductivity, dielectric characteristics, and semiconducting behavior. The latter is particularly interesting for the fabrication of light-emitting diodes (LEDs) and solar cells. In the context of this project, the focus is on perovskites for solar cell applications, which will be explained in the next section.

2.1.2 Perovskites in solar cells

Hybrid organic-inorganic metal halide perovskites

In terms of solar cells, the most studied perovskite materials are hybrid organic-inorganic metal halide perovskites (HOIPs), which are often called just perovskites for simplicity. In solar cells, the role of HOIP is to absorb light and form electron-hole pairs. When combined with the right charge transport layers, it has the ability to generate electricity. For this reason, the HOIP layer in a solar cell is also called the absorber layer.

In HOIPs, the anion X is the halide, the most commonly used halides are iodide (I^-), bromide (Br^-) and chloride (Cl^-) [20–22]. The cation B is the metal that generally corresponds to lead (Pb^{2+}), tin (Sn^{2+}) or germanium (Ge^{2+}) [20, 23, 24]. Together, the anion X and the cation B form the inorganic part of the perovskite. The cation A is the organic component of HOIP, it is a small organic molecule, such that it can fit the perovskite structure. Usually methylammonium (MA^+) or formamidinium (FA^+) is used as A cation [20, 25]. As will be explained later, the organic component can be a source of instability in perovskites. Therefore, there is research in all inorganic halide perovskites, where the organic part is replaced by cesium (Cs^+) [21].

The ability to combine different compounds is one of the major assets of perovskites, because it is possible to fine-tune their composition to obtain the desired characteristics. For example, Noh et al. showed that by replacing some of the iodine with bromine in methylammonium lead iodide ($MAPbI_3$), it is possible to continuously increase the bandgap of the absorber from 1.5 to 2.3 eV [26]. To illustrate the change in bandgap as a function of composition, Figure 2.3 shows pictures of $MAPb(I_xBr_{1-x})_3$ samples with different compositions, where the x was varied from $x = 0$ to $x = 1$. The change in color is an indicator of the change in bandgap.

Figure 2.3: Sequence of pictures of $MAPb(I_xBr_{1-x})_3$ for different x values from $x = 0$ to $x = 1$. Figure taken from [26].

Another positive aspect of perovskites is the multiple ways that can be used to synthesize them. Synthesis methods go from solution processing, such as spin coating and coat blading, to vapor deposition methods, such as physical vapor deposition (PVD) and chemical vapor deposition (CVD) [27–30].

HOIPs still have two major drawbacks, hindering their commercialization. First, the presence of lead in most efficient solar cells [31–33]. This is a problem because of lead toxicity. The second drawback is the perovskite stability. These materials tend to degrade when exposed to light [34, 35], water [36, 37], oxygen, and heat [38–40], which corresponds to the stresses to which solar panels are usually exposed when deployed in the field. Although major improvements have been made in the past years in the perovskite stability, the material has to remain stable for a minimum of 25 years in order to have a similar lifetime warranty to Si solar cells.

Therefore, in order to make perovskites available to use as soon as possible, it would be ideal to move away from the Pb component and improve the stability of perovskites.

Particularities of $MASnI_3$

Until now, the most studied HOIPs have been $MAPbI_3$, which contains MA^+ as cation A, Pb as cation B, and I as the anion X [23]. For this reason, when choosing an lead-free HOIP, it seemed logical to stay closer to a well-known material to take advantage of all the research that has already been performed. In this regard, $MASnI_3$ is the closest in composition to $MAPbI_3$. The cation A and the anion X remain the same, and only the cation B changes. Furthermore, Pb and Sn both belong to the carbon group in the periodic table, where Sn is placed just above Pb, meaning that both elements have a similar valence shell. Moreover, the band gap of $MASnI_3$ is 1.3 eV, which is close to the maximum intensity of the Shockley-Queisser limit [41]. That is, it is the ideal bandgap for solar cells, because a high PCE is expected.

The first time $MASnI_3$ was reported was in 1990 by Yamada et al. where its crystal structure was studied [42]. The next publication on $MASnI_3$ comes only four years later, in 1994 where Mitzi et al. study the transport, optical and magnetic properties of $MASnI_3$ in the context of superconductivity [43]. In this study, $MASnI_3$ is described as a low carrier density metal, which is not superconductive. Only in 2013, Stoumpos et al. identified $MASnI_3$ as a semiconductor and suggested its use for photovoltaic application [23]. Approximately one year later, Hao et al. reported the first $MASnI_3$ solar cell, in an effort to create Pb-free HOIP devices [44]. This device had a PCE of 5.23 %. Nowadays, Sn-base perovskites have exceeded 14 % PCE [45, 46].

However, it was quickly realized that $MASnI_3$ and other Sn-based perovskites degraded even faster than Pb-based perovskites. One of the main pitfalls is that Sn tends to oxidize rather easily, which is not the case for Pb [47]. This oxidation has been said to cause high

p-doping levels (through the formation of additional charge carriers) and to trigger cyclic degradation [48].

It is clear that in order for perovskites to become commercially available, they have to become more stable and preferentially lead-free. Furthermore, they must remain affordable and be done with abundant materials, so that they can be competitive with more mature technologies. Numerous publications study the degradation of Sn-based perovskites and try to improve stability and efficiency as it will be discussed in Section 2.4.

2.2 Physical Vapor Deposition

Physical vacuum deposition (PVD) is commonly used for thin film fabrication. It consists of four main phases: (1) Vaporize the source, (2) transport of the evaporated material, (3) deposition of the material on a substrate, and (4) rearrangement of the atoms [49]. Different PVD techniques exist, such as sputtering, electron beam evaporation, or ion deposition, but here the focus is on thermal evaporation.

Thermal evaporation consists of heating the source material in a vacuum environment (see Figure 2.4), so that the material vaporizes and condenses on the substrate. The use of vacuum is essential in the transport phase, because it minimizes sample contamination and increases the mean free path of molecules, so that molecules travel in line of sight towards the substrate, allowing clean surfaces to be produced [49]. It should be noted that during the transport phase, the material atoms form an evaporation cone, which follows the cosine law of vapor emission [49]. In the case of a flat substrate, this results in a higher quantity of material deposited towards the evaporation symmetry axis of the material source.

When the atom reaches the substrate, it first adsorbs to the substrate, then diffuses within the substrate surface, and finally incorporates in the crystal lattice [50]. Atoms can also desorb from the substrate. Therefore, the adsorption flux should be greater than the desorption flux in order to form a film.

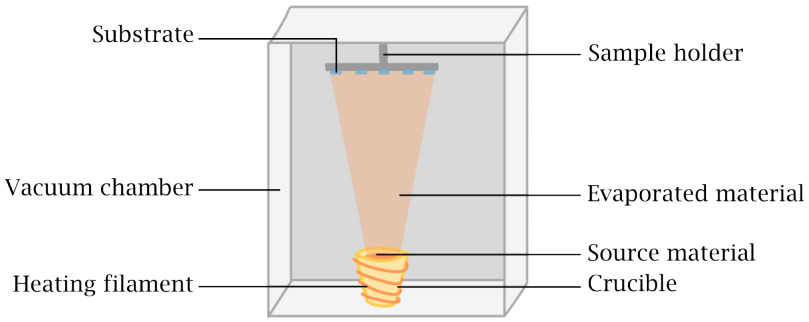

Figure 2.4: Schematics of a thermal evaporation chamber.

The Hertz-Knudsen formula can predict whether a material can evaporate or condense [49]. This equation gives the rate of vaporization, which describes the transition of the molecules in the solid (or liquid) phase to a gaseous phase

$$J_{vap} = \alpha \frac{P_{eq} - P}{\sqrt{2\pi m k_B T}} \tag{2.4}$$

where J_{vap} is the rate of vaporization, α is the sticking coefficient, which gives the probability that a molecule adsorbs onto a surface. P_{eq} is the equilibrium vapor pressure of the material at temperature T, P is the vapor pressure of the surrounding gas. Finally, m is the mass of a molecule of the considered material and k_B is the Boltzmann constant. Note that depending on P and P_{eq}, J_{vap} can be positive or negative. In fact, a $P_{eq} - P > 0$ means that the considered material evaporates, but $P_{eq} - P < 0$ means that the material condenses.

2.2.1 Physical Vapor Deposition of HOIP

There are two main ways of synthesizing perovskites: solvent-based and evaporation techniques. The main difference between both methods is that evaporation techniques are solvent-free dry techniques. Solvent-based methods, as indicated in the name itself, include solvents in material processing, which is the case for multiple synthesis methods, such as spin coating [11], spray coating [51], and inkjet printing [52].

In the famework of this project, evaporation was the method of choice, because it provides more homogeneous films and does not produce solvent waste [53]. Furthermore, the findings made on evaporated perovskites films could be more beneficial for industry, as evaporation techniques are already widely used in the photovoltaic thin film industry and it is likely that this will be the method of choice when industries transition to the production of perovskite solar cells [54].

Thermal evaporation of HOIPs itself includes multiple variants, such as

- single source evaporation [55]: where the HOIP powder is evaporated
- multistep evaporation [56]: which consist of evaporating multiple layers of different precursors alternated
- co-evaporation [57]: where multiple precursors are evaporated simultaneously.

Here, the focus is on co-evaporation. Typically, in the synthesis of HOIP, there are two evaporation sources, the first is the organic salt, typically methylammonium iodide (MAI), and the second is the metal halide, usually PbI_2 (see Figure 2.5). The advantage of this method is that the composition in the film is relatively easy to control and does not require post-deposition treatment, such as annealing. In this figure, three possible reactions paths, namely (1) The reaction of the MAI and the PbI_2 after condensing onto the substrate, (2) the reaction of the excess PbI_2 in the substrate with the MAI in the gas phase and (3) the reaction of PbI_2 and MAI before condensing onto the substrate.

Quartz crystal microbalances (QCMs) are usually used to monitor the evaporation rate of the different materials in co-evaporation. However, it is not possible to measure the evaporation rate of MAI with QCMs [57–60]. The issue being that MAI has a low sticking coefficient, which results in non-directional deposition (see Figure 2.5). To avoid this problem, it is possible to either use the temperature of the MAI as an indicator of the evaporated quantity [57] or the partial pressure of the MAI [58–60]. The latter assumes that the evaporation of the

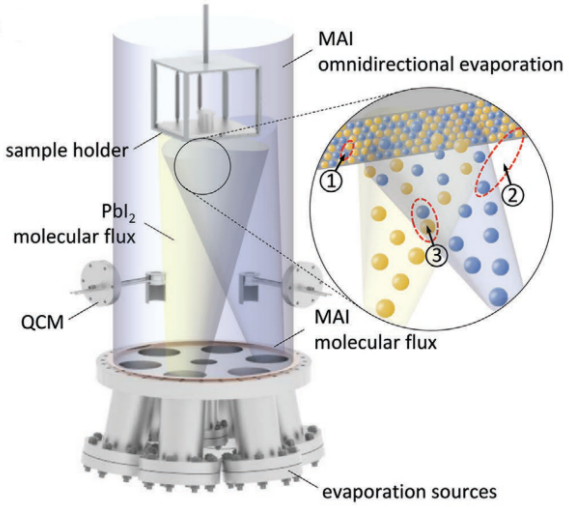

Figure 2.5: Schematics of a co-evaporation of $MAPbI_3$ and inset with possible reaction processes. (1) The reaction of the MAI and the PbI_2 after condensing onto the substrate, (2) the reaction of the excess PbI_2 in the substrate with the MAI in the gas phase and (3) the reaction of PbI_2 and MAI before condensing onto the substrate [58].

metal halide is effusive, meaning that its partial pressure would be negligible and therefore the pressure in the chamber can be considered as the partial pressure of the MAI.

2.3 Measurement and Identification of Degradation Mechanism in HOIP

Ultraviolet–Visible–Near Infrared Spectroscopy

Ultraviolet-visible (UV-vis) spectroscopy is a measurement technique used to obtain the transmission and the reflection of materials. For semiconductor materials, it is also possible to estimate the optical band gap from the absorption spectrum. Furthermore, it is possible to identify the presence of molecules and structures in the sample from their different characteristic absorption peaks [61].

UV-vis measurements of different Sn-based perovskites during prolonged light exposure (1000 h) showed that the absorbance of the films decreases significantly, in some cases reaching almost 0 % absorbance [62]. Moreover, Lanzetta et al. showed that the absorbance of Sn-based perovskites does not decrease upon exposure to 90 % humidity for 30 minutes, does decreases when exposed to dry air instead. [48]. Furthermore, they showed that the effect is enhanced, when the sample is exposed to air with humidity of 90 %. The characteristic absorption spectrum of SnI_4 was also used to identify its presence in Sn-perovskites after exposing the sample to I_2 [48, 63].

X-Ray Diffraction

X-ray diffraction (XRD) is a measurement technique that gives crystalline information about the bulk of the sample, such as interatomic distances, crystal orientation, or secondary phases [64]. Secondary phases include phases with a different composition from that of the main phase and phases with the same composition as the main phase but a different crystalline structure.

Studies of degradation in a nitrogen glovebox at 90 °C, showed the formation of an SnI_2 secondary phase [62]. However, light degradation resulted in a reduction of the sample's crystallinity, which was assigned to the formation of metallic tin. Gong. et al, identified the formation of a double perovskite secondary phase upon exposure of the Sn-based perovskite to dry air. In formamidinium lead iodide ($FAPbI_3$), XRD measurements were used to identify the formation of a secondary phase [65].

Atomic Force Microscopy and Kelvin Probe Force Microscopy

Atomic force microscopy (AFM) is a measurement technique that is capable of measuring a map of the topography of the surface of a sample, with a height with atomic resolution.

Furthermore, this technique can be executed simultaneously to Kelvin probe force microscopy (KPFM), which, when calibrated, measures the workfunction at the sample surface [66].

The light-induced degradation of $FAPbI_3$ was studied using AFM and KPFM. The AFM measurements of the degraded sample showed some grains with rough topography [34]. The KPFM measurements revealed that these rougher topography regions had a greater work-function than the rest of the sample. These regions were deduced to be PbI_2. In a different study, KPFM measurements were performed on a $FAPbI_3$ sample degraded by humidity and the non-perovskite secondary phase was observed [67].

X-Ray Photoelectron Spectroscopy

X-Ray Photoelectron Spectroscopy (XPS) is a measurement technique that is used to obtain information on the composition of materials and the oxidation state of the different elements within the material. It can measure the sample in the near-surface region, making it ideal for thin films [68].

XPS measurements were performed on thermally annealed $MASnI_3$ [62]. The results show that after 200 h of annealing at 90 °C, no nitrogen signal was detected in the measured spectrum, which means that no $MASnI_3$ was present. These measurements were complemented with XRD which showed that the sample degraded into SnI_2. The same publication reported a similar result for light-induced degradation in $MASnI_3$, where after 1000 h of exposure to light, the nitrogen peak was barely visible. A different study revealed that exposure of a $MASnI_3$ sample to dry air for 1 h results in the oxidation of 94.6 % of the tin present in the surface of the sample [69]. Additionally, for the lead counterparts, the formation of metallic lead due to vacuum-induced degradation of Pb-based perovskite was also observed with XPS measurement [70].

In this section a list of some of the characterization techniques used on perovskites was presented. The next sections focus on studies done on perovskites for intrinsic and

extrinsic degradation of perovskites. For the latter, the focus will be on light, water, and oxygen degradation. In addition, the last section summarizes the degradation effects of the measurement techniques.

2.4 Degradation of Sn-based HOIPs

As mentioned above, one of the major pitfalls of HOIPs is the degradation over time, which is even more accentuated when perovskites contain tin. The causes of degradation in perovskites can be separated into two main categories: intrinsic and extrinsic causes. The intrinsic causes are related to the composition of the perovskite and to impurities, such as impurities from the used precursors or eventually residues of solvent that remained in the film due to the synthesis technique. In contrast, extrinsic causes are external stresses such as exposure to light, heat, water, and oxygen.

2.4.1 Intrinsic degradation of HOIPs

In terms of intrinsic causes for degradation, one of the reasons put forward is the use of Sn itself. In fact, in the perovskite structure, Sn must be in the (2+) oxidation state. Nevertheless, unlike Pb, Sn does not have lanthanide contraction. That means that the electrons in the last shell can leave more easily, which in turn results in the oxidation of Sn(2+) into Sn(4+) [71]. This is harmful to the device, because the presence of Sn(4+) is associated with excess p-doping in the device, which in turn reduces the carrier lifetime and therefore the device performance [72].

The Frost diagrams of Sn, Pb and I, that is, the Gibbs free energy plots as a function of the oxidation state, are shown in Figure 2.6 [17]. The plots show how stable each oxidation state is; the lowest value corresponds to the most thermodynamically stable oxidation state. In Figure 2.6, it is clear that the oxidation state Sn(4+) is extremely close to Sn(2+), especially compared to Pb(2+) and Pb(4+). This explains why in the literature the Sn(4+)

state is often detected in Sn-based perovskites but not for Pb-based ones. It should be noted that I(1-), which is the expected oxidation state in perovskite, is close to I(0), which is the oxidation state of I_2. This means that I in the perovskite can easily form I_2.

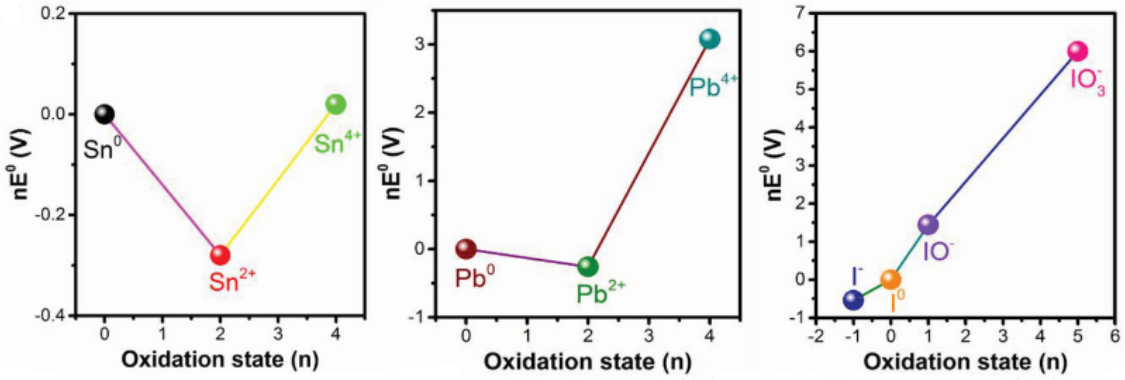

Figure 2.6: Frost–Ebsworth diagrams of tin, lead and iodine [17].

Another intrinsic source of degradation is the perovskite synthesis method. In fact, many groups use solvent based methods, where SnI_2 is dissolved in dimethylsulfoxide (DMSO) or in a mixture of solvents containing DMSO. Figure 2.7 shows a solution of $FASnI_3$ freshly dissolved into DMSO and another solution prepared with dimethylformamide (DMF) [73]. On the left of each group of pictures is the fresh solution and on the right is the solution after aging for 5 h at 120 °C. The DMSO solution underwent a significant change in color after it was aged, whereas the DMF solution showed almost no change in color. The different color was attributed to the presence of Sn(4+). That means that traces of DMSO in the perovskite film, due to incomplete evaporation, could oxidize Sn(2+) into Sn(4+). Furthermore, DMSO has already been shown to be an oxidation agent for Sn(2+) [74]. Therefore, the use of DMSO should be avoided in the film synthesis process.

Another intrinsic source of degradation could be the precursors that are used. One of the main contaminants of the SnI_2 powder is SnI_4 [75]. This is even more problematic because SnI_4 and I_2 are believed to promote degradation in the perovskite by contributing to the formation of SnI_4 [75]. Lanzetta et al. suggested a degradation mechanism with water and

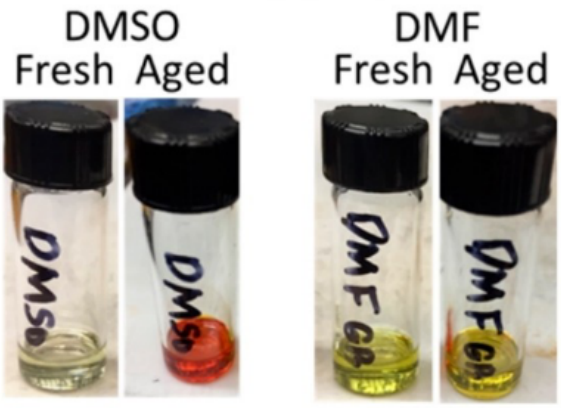

Figure 2.7: Picture of two $FASnI_3$ solutions, with DMSO (left) and DMF (right) as fresh and after aging for 5 h at 120 °C [73].

oxygen as external stresses, where the products of the degradation of Sn-based perovskites contribute to a cyclic degradation of the sample (Figure 2.8) [48].

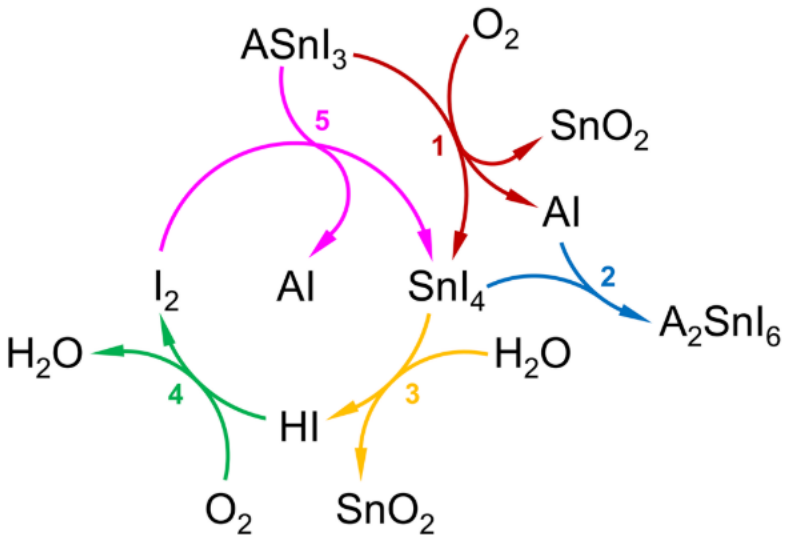

Figure 2.8: Cyclic degradation of Sn-based perovskites suggested by Lanzetta et al. [48].

In addition to intrinsic degradation, perovskites suffer from degradation induced by external stresses. The next sections will discuss studies that are present in the literature, starting with light-induced degradation.

2.4.2 Light-induced degradation

Starting with light-induced degradation, for Pb-based, Sn-based, and for mixed metal perovskites, published reports agree that the organic component tends to leave the surface of the sample, especially when the organic component is MA^+ [62, 76, 77]. However, the reaction products formed during degradation are not yet clear. Different reports agree that Sn(4+) is formed upon illumination of Sn-based perovskites [62, 78, 79], but disagree on additional effects. For example, Sn-based perovskite solar cells have been reported to increase their efficiency when exposed to light [79], but the formation of metallic tin has also been observed [62], which would result in shunt and therefore a decrease in efficiency.

2.4.3 Water-induced degradation

The water-induced degradation on $MAPbI_3$ and $MASnI_3$ has been associated with the MA^+ group, which has a hydrophilic compound (NH_3^+) and has a strong interaction with water molecules [80]. Yet, it is especially difficult to pinpoint the degradation mechanism of perovskites when exposed to water vapor or moisture (i.e., water vapor in air), and numerous different models have been reported [36, 81–84]. The first model, by Frost et al., suggests that one water molecule is enough to trigger perovskite degradation [81]. Initially, MA^+ loses a proton, which bonds with a water molecule to form H_3O^+ then, in the presence of excess water, the perovskite further degrades into HI, CH_3NH_2 and PbI_2. In a different study, $MAPbI_3$ was found to form hydrocarbons (-CH_2-) upon exposure to water, together with NH_3, HI and PbI_2 [83], and a similar mechanism was found for $MAPbBr_3$ [36]. When exposed to moisture $MAPbI_3$ samples, degrade in two steps (1) the absorber reversibly forms perovskite mono-hydrates ($CH_3NH_3PbI_3 \bullet H_2O$) and di-hydrates ($(CH_3NH_3)4PbI_6 \bullet 2H_2O$), (2) once the grain is fully converted into hydrate, irreversible degradation occurs and PbI_2 is formed [85].

One of the reasons for the discrepancy between the models is probably that water degradation depends on the termination of the facet [37]. In fact, it was experimentally observed

that after exposure of $MAPbI_3$ to moisture, MAI terminated facets first form perovskite mono-hydrates followed by the formation of PbI_2, while in PbI terminated facets, deprotonation occurs and PbI_2 is formed [86].

Although multiple models exist, they all have a common point: $MAPbI_3$ water-induced degradation produces PbI_2 [81, 85, 87]. This is also the case when the perovskite is exposed to liquid water. In fact, Hailegnaw et al. found that, when $MAPbI_3$ is exposed to liquid water, PbI_2 forms on the substrate [88], while MAI decomposes into HI and CH_3NH_2. This result was obtained by pouring water on a $MAPbI_3$ film to replicate rain and dipping $MAPbI_3$ films in water.

There are relatively few studies on moisture (which here corresponds to the water present in air) and water vapor degradation in Sn-based perovskites. In multiple publications, the degradation mechanisms for lead-based perovskites and tin-based perovskites are assumed to be similar [89, 90], with the additional oxidation of Sn(2+) to Sn(4+) pathway [47]. When comparing the degradation of $MAPbI_3$ with the degradation of $MASnI_3$, simulations have shown that although water molecules adsorb more easily in $MAPbI_3$ than in $MASnI_3$ [91], $MASnI_3$ degrades faster because the SnI_2 terminated facets dissolve more easily than the PbI_2 terminated facets.

2.4.4 Oxygen-induced degradation

Oxygen-induced degradation studies on Sn-based perovskites using thermogravimetric analysis (TGA), between 100 °C and 600 °C in air, showed that Sn-perovskites form SnI_4 and SnO_2 when exposed to heat [63]. This result was later confirmed by Wei et al. who observed that Sn-based perovskites decomposed into organic salt (MAI and FAI), SnI_4 and SnO_2 [92]. However, in $FASnI_3$ perovskites, it has been shown in $FASnI_3$ perovskites that oxygen-induced degradation depends on the termination of the grain surface. In fact, the O_2 molecule does not adsorb onto a FA/I terminated surface due to the distance between the

surface of the perovskite and the water molecule, while on the Sn/I terminated surfaces, the oxygen atoms can form a bond with Sn [17, 48].

2.4.5 Measurement-induced degradation

Previous reports have studied the vacuum-induced degradation of lead perovskites. Most studies agree that the perovskite loses the organic cation in vacuum [70, 93–95]. However, there is no clear agreement on products of the degradation that remain on the substrate. Different pathways have been observed as formation of Pb(0) [70], formation of PbI_2 [95], or the octahedral rearrangement of the lattice [93]. Guo et al. showed that vacuum fosters light-induced degradation, compared to N_2 atmosphere [96]. In the report, they show that light-induced degradation in vacuum causes phase segregation, lattice shrinkage and morphology deformation, whereas light-induced degraded perovskite in N_2 only shows lattice shrinkage. They associate this difference with a larger energy barrier for lattice distortion in N_2 than in vacuum.

Similarly, for the effect of exposure to X-rays, multiple studies were performed on lead perovskites. Most reports seem to agree that there is a formation of defects due to exposure to X-rays [97, 98], but it is not clear what the composition of the sample after exposure is, as it has been reported that there was almost no compositional change [97], the evaporation of the organic cation [98, 99] and the formation of Pb(0) [98].

To date, no studies of XPS and vacuum-induced degradation in $MASnI_3$ have been found. However, Kim et al. reported that oxidized $PEASnI_4$ is reduced when placed under vacuum, and this process is reversible [100].

In general, in degradation studies of perovskites, there is a divergence in the results. This can be justified by the lack of a standard degradation method, such as different exposure times, different conditions (temperature, water concentrations, light intensities, vacuum level), and the lack of well-documented procedures to transfer the sample to the measurement

setup. Additionally, here, one of the assets of perovskites, i.e. the fact that their composition can be fine-tuned to optimize their properties, comes as a challenge. More specifically, different composition absorbers with different components may have different degradation mechanisms.

2.5 Challenges and Objectives

Perovskite films are usually synthesized using solvent-based techniques. In the case of Sn-based perovskites, this is a problem because some of the solvents used were identified as oxidation agents for Sn. Here, the method of choice for synthesizing Sn-based perovskites was PVD, which is a solvent-free technique. In this way, it is ensured that the observed degradation is caused by external stimuli and not by the solvent remaining in the film after synthesis.

Only a small portion of the literature studies were performed on $MASnI_3$. However, often Pb-free devices contain a combination of MAI and FAI as organic components. Furthermore, MAI is known, from Pb-based perovskites, to leave the surface of the sample. Therefore, it is important to understand the degradation of a simpler composition-wise system such as $MASnI_3$, to unravel the effects of the use of MAI and FAI. This thesis focuses only on the least studied $MASnI_3$.

Given that no literature about the XPS- and vacuum-induced degradation was found, in this work, measurement-induced degradation was studied. To do so, $MASnI_3$ samples were measured in UHV repeatedly using KPFM and XPS. Complementary measurements were also performed using the PL system and a stylus profilometer.

Light-induced degradation studies on Sn-based perovskites in the literature showed contradictory results. In this thesis, the impact of light-induced degradation on $MASnI_3$ composition is studied using XPS.

Finally, in most studies of air-induced degradation of HOIPs, air contains both oxygen and moisture. Here, the aim was to disentangle the degradation induced by oxygen from the degradation induced by water. To do so, $MASnI_3$ perovskites were individually exposed to air or water and then measured in XPS. Note that the samples were carefully transferred between measurements in order to avoid unwanted exposure to air or light.

Chapter 3

Materials and methods

3.1 Sample preparation and degradation

3.1.1 Physical Vapor Deposition of $MASnI_3$

The samples were deposited in a PVD chamber that was placed in a N_2 glovebox. In this way, after deposition, the samples were directly in an N_2 environment, which avoided exposure to air and moisture. The base pressure of the PVD was $1-3\cdot10^{-7}$ mbar. Usually, this pressure was reached after waiting over night. Figure 3.1 shows a schematic representation of the PVD chamber.

The PVD contained three source positions, namely for SnI_2, MAI, and the third source, which was not used in the framework of this thesis, contained either PbI_2 or phenethylammonium iodide (PEAI). The source position consisted of a metallic container with a location for the crucible. On the walls of the container was placed a metallic wire, which heated up the source during deposition. For better temperature control, the source was also connected to a water cooling system. Each source also contained a shutter to close the source when not in use. The powders were placed in heat resistant ceramic crucibles.

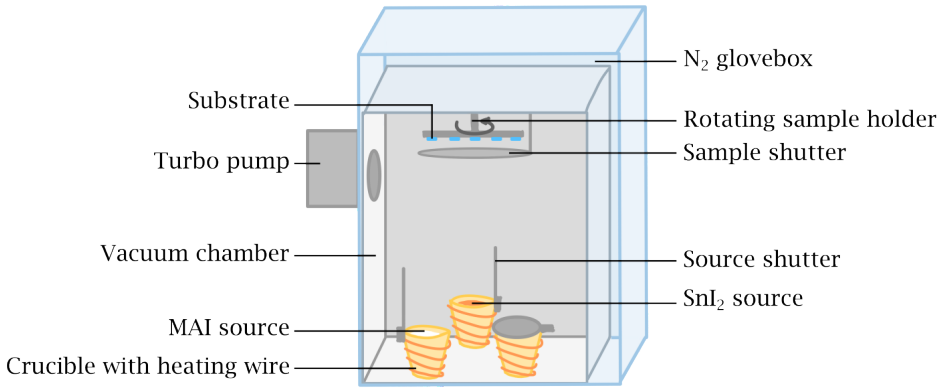

Figure 3.1: Schematic representation of the PVD chamber.

The substrate holder was placed at the top of the PVD, and it was connected to a rotating motor for better deposition homogeneity. A sample shutter was placed below the substrate holder. This shutter remained closed at all times except during deposition.

The PVD was connected to a turbo pump which was supported by a rotary pump. In addition, a cooling trap was placed between the PVD chamber and the turbo pump. The cooling trap served to condense the pumped gas onto the walls by cooling it down. This was used to extend the longevity of the turbo pump. The cooling trap should be switched on 10 minutes prior to deposition so that it cools down to at least -16 °C.

The substrates were quartz and ITO substrates provided by Ossila. They were cut to a square of approximately 8 mm so that they would fit the UHV sample holder in the characterization phase. The substrate cleaning procedure was adapted from [101]. The substrates were cleaned with six different solutions/solvents with an ultrasonic bath at 50 °C for four minutes each solvent. First was a 2 w% solution of Helmanex (provided by Ossila), then deionized water twice, then acetone, followed by isopropanol, and finally clean water again. After which, the substrates were N_2 blown and cleaned with an ultraviolet ozone cleaner for 15 minutes.

For the chamber preparation, the substrates were placed in the sample holder. The powders were not replaced but were always refilled to the same mass. The mass of the SnI_2

powder with the crucible included was 9.550 g (± 0.003 g) and the MAI powder 8.720 g (± 0.003 g).

There were two main deposition procedures followed for the samples studied in this thesis. The first is the procedure followed for most samples in Chapter 4, the second method was used for the samples in the other chapters. Here, the first method will be described and then a small comment with the differences between both methods will be made.

The first deposition method consisted of starting with warming the SnI_2, up to 265 °C with a heating rate of 20 °C/min. In the mean time, the MAI source was kept at 50 °C with an heating rate of 8°C/min. Once the SnI_2 source reached the right temperature, the MAI temperature was set at 95 °C, keeping the heating rate unchanged. After the MAI source reached the right temperature, its temperature was slowly increased, in increments of 2 °C until the chamber pressure reached the right pressure. Unless explicitly mentioned, the samples were deposited at a pressure of $1 \cdot 10^{-5}$ mbar. Every five minutes, it was necessary to check the pressure in the chamber and eventually decrease the MAI temperature to keep the chamber pressure constant. The depositions lasted 90 minutes resulting in 600 nm.

The second procedure has three main differences. First, the sources were heated simultaneously and the MAI heating rate was changed to 7.2 °C/min, so that both sources reached the good temperature simultaneously. The initial chamber pressure was the same, meaning $1 \cdot 10^{-5}$ mbar, but once that pressure was reached, the MAI temperature was no longer modified. This resulted in an increase in pressure with time. In order to keep the pressure in the range advised by the PVD chamber's manufacturer, the samples were deposited only for 45 minutes. This procedure was created later in the project in order to avoid SnI_2 secondary phases, as explained in Chapter 4.

In both procedures, the SnI_2 powder was provided by TCI and the MAI powder was also provided by TCI except if mentioned otherwise.

For the deposition of SnI_2 films, the used procedure was similar to the one used for $MASnI_3$, except that the MAI source was kept at a temperature of 80 °C.

3.1.2 Sample transport

To avoid exposure to air and moisture, the samples were transported in a vacuum/N_2 suitcase. The suitcase consisted of various vacuum parts with closing valves that could keep the sample in high vacuum. The suitcase could be connected to the glovebox and to the vacuum systems, so that the samples could be moved directly from the glovebox to the suitcase and from the suitcase to the vacuum systems. The suitcase also contained a small manipulator which allowed to hold, introduce or remove the sample. In this project, two different suitcases were used, the one-slot suitcase and the four-slot suitcase. The one-slot suitcase could only transfer one sample each time and was perfect to connect to the gas dosing system (see next section). The four-slot suitcase included an additional stacked sample placement and could transport up to four samples at once. This suitcase was ideal for the transport of multiple sister samples into the UHV systems.

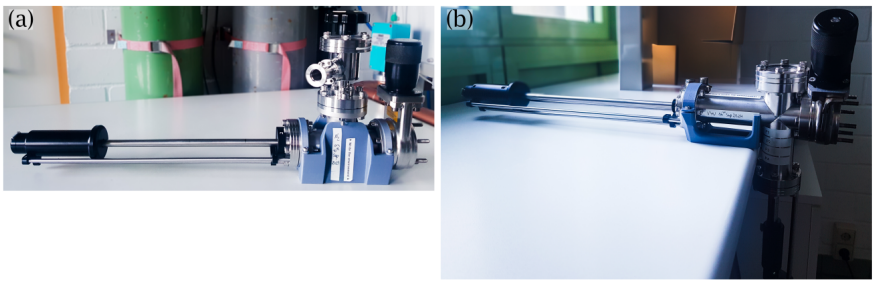

Figure 3.2: Pictures of the suitcases. (a) One-slot suitcase and (b) four-slot suitcase.

3.1.3 Gas dosing system

The gas dosing system was specifically built for this project. It was designed and built with the help of Dr. Bernd Uder and Dr. Ulrich Siegel. It consisted of a small vacuum chamber with a mechanical pump capable of reaching a vacuum level of the order of 10^{-3} mbar, some valves, to control the quantity of introduced gas, and a pressure gauge (see Figure 3.3).

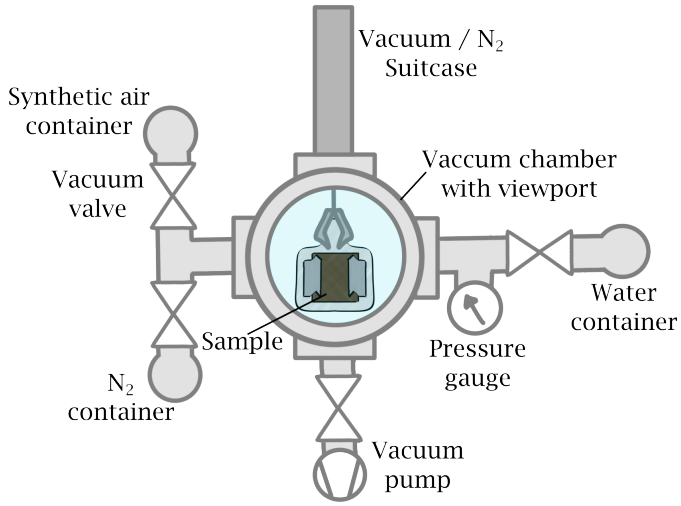

Figure 3.3: Schematics of the gas dosing system (top view).

The system was compatible with the suitcase. Therefore, the sample was brought in the suitcase, and during exposure, the sample remained on the manipulator of the suitcase, which was long enough to reach the center of the dosing gas system.

The gas dosing system had two modes of exposure: synthetic air and water vapor mode. Note that synthetic air consists of N_2 and O_2 without water vapor. For the exposure of the sample to synthetic air, a small synthetic air gas bottle, namely CANgas with 99.999% of purity and supplied by Messer, was attached to the setup. The sample was exposed to approximately 1000 ($\pm$5) mbar of synthetic air for different periods of time.

For water vapor exposure. A glass container for vacuum use was filled with water. In order to purify the water and remove any air dissolved in the water, at least pumping cycles

were performed. Each pumping cycle lasted until the water froze. Once the water was ready, the samples were exposed to 20 ($\pm$5) mbar of water vapor for different periods of time.

3.2 Characterization

3.2.1 X-ray photoelectron spectroscopy

Basic Principles

This section is based on [68, 102–104].

X-ray photoelectron spectroscopy (XPS) is a powerful technique that measures the composition of samples and determines the chemical state of the different components. The key principle uses the photoelectric effect to extract electrons from the sample using X-ray radiation. Typically, XPS is performed under ultra-high vacuum (UHV), in part to decrease the collisions between the electrons and any gas particles. The probing depth of XPS is between 8 nm and 10 nm.

The equipment consists of three main parts: an X-ray source, an analyzer, and a detector. The X-rays are generated in the X-ray gun, where electrons are accelerated against a metal (usually magnesium or aluminum). The X-rays are then directed towards the sample.

When an X-ray photon hits an electron in the sample, the electron is ejected to the vacuum with a kinetic energy E_{kin}. After ejection, the electron is usually called a photoelectron. The photoelectrons are then slowed down, in the lens tube, to the pass energy E_{pass} before reaching the hemispherical analyzer (Figure 3.4). The analyzer is a set of two concentric hemispheres of different radii with a voltage difference of ΔV. Hence, when a photoelectron enters the analyzer, its trajectory deviates into a curved trajectory. This allows selecting the photoelectrons that correspond to the right E_{kin} with a tolerance window ΔE around the E_{pass}. Electrons that are too slow, deviate too much, and hit the inner hemisphere. Electrons

that are too fast, do not deviate enough, and hit the outer hemisphere. Finally, the electrons in the right E_{kin} window reach the detector, whose output is the count of electrons as a function of the kinetic energy. More details on the functionning of XPS can be found on [68]

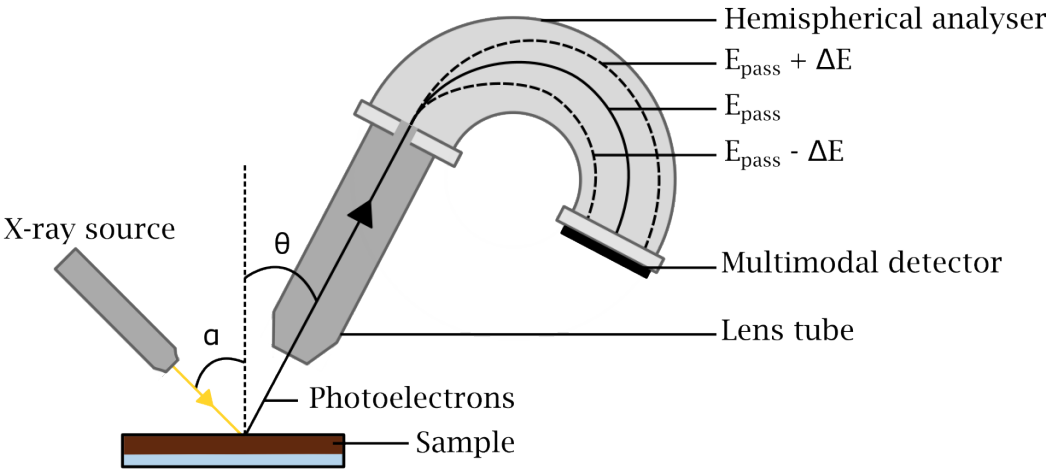

Figure 3.4: Schematic representation of the cross-section of an XPS analyser.

The value of interest when an XPS measurement is performed is the binding energy E_{bin} of the electrons that leave the surface of the sample. This can be calculated using

$$E_{bin} = h\nu - E_{kin} - \phi \tag{3.1}$$

where $h\nu$ is the energy of the X-ray light and ϕ is the workfunction of the spectrometer [68]. The advantage of using E_{bin} instead of E_{kin}, is that E_{bin} is specific to each element and does not depend on the X-ray light energy. Different oxidation states and different chemical environments result in E_{bin} shifts, which will be important in the study of $MASnI_3$ degradation.

For the measurements present in this thesis, the Prevac EA15 analyzer was used at UHV pressures between $5 - 9 \cdot 10^{-10}$ mbar. A MgK_α non-monochromatic source with the

main emission line at 1253.6 eV was used. The intensity of the XPS is regularly calibrated by the XPS users in order to ensure an accurate quantification. To calibrate the equipment, different pure metals are used such as tin, copper, gold, and silver.

Quantification analysis

A typical spectrum of $MASnI_3$ is shown in Figure 3.5. The regions of greatest significance for degradation studies are highlighted in blue. Note that iodine, tin, nitrogen, and carbon are part of the perovskite composition. Therefore, they should be present in specific quantities in an ideal perovskite. On the other hand, oxygen is considered one of the major causes of perovskite degradation when the film is exposed to water and air, and therefore, it is essential to follow the presence of oxygen too. In Figure 3.5, the anotation for each element includes the element name as in the periodic table, followed by the electron quantum number n, the orbital angular moment quantum number l, and eventually the total angular momentum j, for example, for iodide the notation is I3d3/2 or I3d5/2.

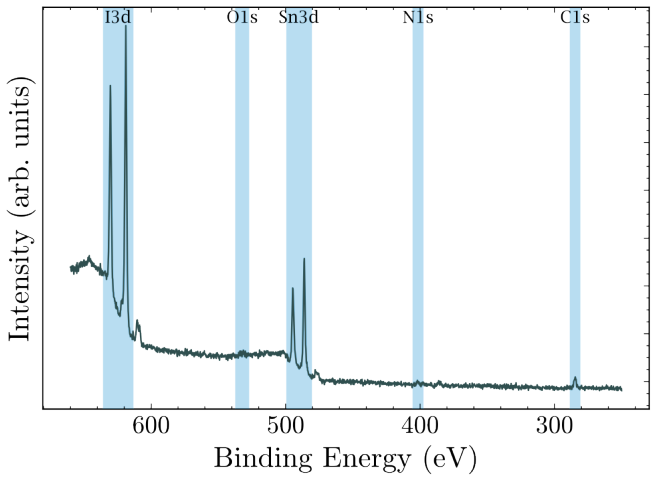

Figure 3.5: Full survey of $MASnI_3$, the components of interest in the framework of this thesis are highlighted in blue.

The different elements can be identified by their binding energies. The expected binding energies for each element are tabulated in databases such as the U.S. National Institute of

Standards and Technology (NIST) XPS database and also the Handbook of X-ray Photoelectron Spectroscopy by Moulder [102, 105].

The measured intensity peak area I_x of an element x, can be described as [68]

$$I_x = \sigma_x W_x G_x \frac{I_{h\nu}}{cos\alpha} N_x \lambda_x cos\theta. \tag{3.2}$$

In this equation, the values with x in subscript are dependent on the element x or its binding energy ($E_{bin,x}$). More precisely, σ_x is the photoionization cross section of element x as described by Scofield [106], W_x is the angular asymmetry factor of the electron subshell of x, G_x is the analyzer efficiency at $E_{bin,x}$, N_x is the density of atoms of element x in the sample and λ_x is the attenuation length of the photoelectrons of x at $E_{bin,x}$. The values that depend on the configuration of the spectrometer are the X-ray intensity $I_{h\nu}$, the angle between the X-ray source and the normal of the sample α, and the angle between the normal of the sample and the detector θ (the angles are shown in Figure 3.4).

Typically, in XPS one does not extract the absolute number of atoms of an element but the ratio between two elements, allowing the simplification of all the equipment related variables. For simplicity, let $S_x = W_x G_x \lambda_x$, then the intensity ratio of element x and element y is given by

$$\frac{I_x}{I_y} = \frac{S_x}{S_y} \frac{\sigma_x}{\sigma_y} \frac{N_x}{N_y}. \tag{3.3}$$

Therefore, the value of interest, the ratio between the atom density N_x/N_y is given by

$$\frac{N_x}{N_y} = \frac{S_y}{S_x} \frac{\sigma_y}{\sigma_x} \frac{I_x}{I_y}. \tag{3.4}$$

The Scofield photoionization cross sections σ are tabulated [106], in the framework of this thesis, the value $S_x(E_{bin,x})$ was obtained by calibrating the measured intensity using well-known simpler reference samples such as metallic tin, copper, gold, silver and SnI_2. This calibration was performed by multiple people in the group.

In addition to intensity calibration, it is important to know the position of the E_{bin} and the full width half maximum (FWHM) of each of the elements studied, and in the case of degradation studies, it is also important to know the E_{bin} of each oxidation state.

In the case of tin and iodide, the orbital with the highest signal is the 3d orbital. For any orbital besides the s orbitals, there is spin-orbit coupling, which yields two peak contributions in XPS. For the 3d, the angular momentum of the split levels is $j = 3/2$ and $j = 5/2$. Figure 3.4 (a) shows the XPS measurement of an oxidized metallic tin plate and (b) a measurement of an SnI_2 film. The two peaks visible in each scan are due to the spin-orbit coupling and are marked as 3/2 and 5/2.

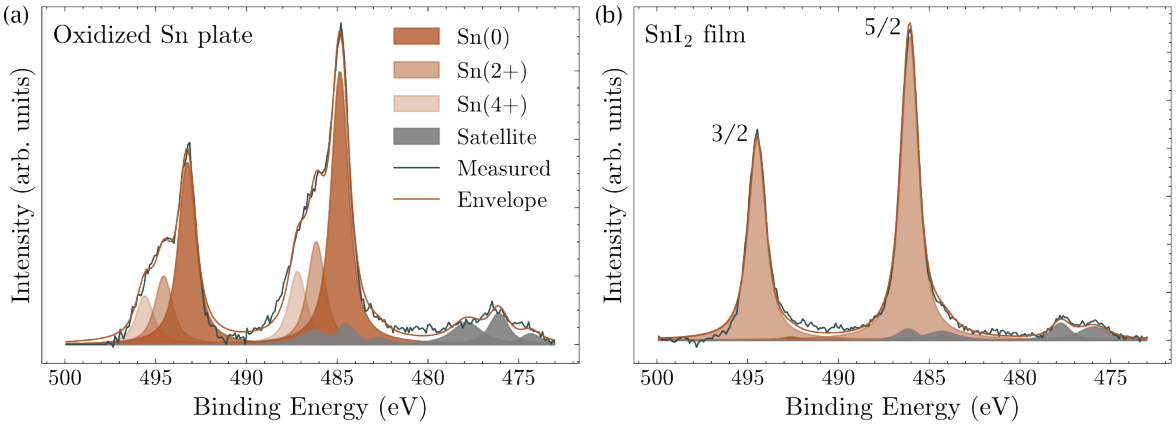

Figure 3.6: Spectra of (a) an oxidized Sn plate and (b) and SnI_2 film in the E_{bin} region of Sn3d.

In order to estimate the FWHM of the Sn3d peaks, a pure metallic Sn plate was sputtered in UHV and measured [107]. Note that the FWHM of the peak of the same element is constant for every sample measured in the same analyzer. An increase in FWHM usually indicates the presence of another oxidation state, a secondary phase with a different chemical environment,

or a measurement artifact. Therefore, it is important to use extremely clean samples as a reference.

The position of the different oxidation states of Sn could be determined by measuring an oxidized Sn plate. Since the FWHM was already known from the sputtered plate, it was possible to deconvolute the three oxidation states (Sn(0), Sn(2+) and Sn(4+) visible in Figure 3.6 (a)).

In addition to the different oxidation states, six satellite peaks are visible. This is due to the use of a non-monochromatic X-ray source. Therefore, satellite peaks, generated by the additional emission lines from the X-ray source, are visible in the measurement. These peaks are an artifact and their approximate values are estimated in the literature [68]. In the case of tin and iodide, these satellite peaks interfere with phase identification and quantification because the 3d3/2 satellite peaks overlap with the 3d5/2 main peak (see Figure 3.6 and 3.7). Therefore, it is necessary to include the satellite peaks in the peak model for a more precise quantification.

It should be noted that metallic Sn has a different chemical environment than $MASnI_3$. Therefore, an E_{bin} shift could be present in $MASnI_3$ compared to metallic Sn. For this reason, an SnI_2 film, which has a chemical environment closer to that of $MASnI_3$, was also used as a reference sample to determine the E_{bin} of the Sn(2+) peak. Furthermore, the ideal stoichiometric ratio I_I/I_{Sn} of SnI_2 is 2. Therefore, the I_I/I_{Sn} ratio (from now on denoted I/Sn) allowed the verification of the intensity calibration of the equipment. Whenever the measured ratio of SnI_2 had an error larger than 2 % (for example, after maintenance), the SnI_2 film would be used to calibrate the iodine intensity in the perovskite measurement.

The SnI_2 film was also used to determine the E_{bin} and FWHM of the I3d peaks. Figure 3.7 shows the detailed spectrum in the I3d binding energy region.

When multiple oxidation states of an element are present in a sample, the different oxidation peaks may overlap, and in that case it is necessary to deconvolute the peaks. To

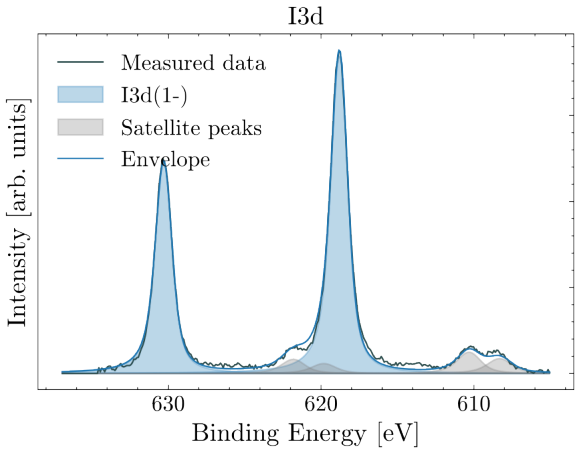

Figure 3.7: XPS spectrum of SnI_2 in the I3d region.

do so, there are a some constrains that can be used, in order to make a realistic peak model:

- The FWHM of an element is the same for every oxidation state within the same orbital.

- In case of spin-orbit coupling, the intensity ratio of the peak of each angular momentum is approximately the ratio between their degeneracy states. For example for 3d3/2 and 3d5/2 the ratio is 2/3.

- The difference in the binding energy ΔE_{bin} between two orbit-spin coupling peaks is constant and depends on the element. The values for different elements are well documented [102]. Here, the used value for Sn3d was 8.41 eV and for I3d was 11.5 eV.

- The expected binding energy for peaks of different elements and different oxidation states should also be limited within an energy interval. This interval usually depends on the XPS resolution. Ideally, the binding energy position is determined with a reference sample.

Note that the line-shape of the peak fitting is important to remain constant for each element when analyzing across different samples. Different line-shapes yield different FWHM, which could have an impact on the quantification. Here, three line-shapes were used:

1. SGL(a) is a sum of Gaussian and a Lorentzian contribution. Where a=0 results in a pure Gaussian and an a=100 in a pure Lorentzian;

2. LA(a, b, m) is a Lorentzian convoluted with a Gaussian where a and b relate to the degree of asymmetry in the low E_{bin} energy region. Values such that $a > b$ result in an extended tail of the XPS peak signal. The parameter m defines the width of the Gaussian in the convolution. In this thesis, the parameter m was not used;

3. TLA(a, b, m) is the product of a Lorentzian with the inverse of a tangent convoluted with a Gaussian. The parameter a affects the contribution of the Lorentzian, a large a results in a strong Lorentzian contribution. The parameter b affects the curve asymmetry. A large b means a strong contribution from the inverse tangent, which results in a tail on the low-energy side of the peak. Similar to LA, the parameter m defines the width of the Gaussian in the convolution.

The line-shape parameters were chosen such that they would best fit the perovskite peaks. Table 3.1 summarizes the fitting parameters used for each element and a tolerance inter was given to the E_{bin} and FWHM values (i.e. ± 0.1 and ± 0.01 respectivily) For more information on the line-shape and the corresponding formulae, the reader is invited to refer to [108, 109].

	Sn3d	**I3d**	**C1s**	**N1s**	**O1s**
Background	W Tougaard	U 2 Tougaard	Shirley	Shirley	Linear
Line shape	LA(1,85)	TLA(1,0.66,141)	SGL(10)	SGL(10)	SGL(10)
FWHM [eV]	1.16	1.33	1.60	1.5	1.45

Table 3.1: Summary of the fitting parameters for the peak model.

As previously mentioned, the position of the Sn3d5/2 peaks was determined using metallic Sn and SnI_2, and the position of the I3d5/2 peak was determined using SnI_2. However, the E_{bin} of C1s and N1s were determined using the average energy of multiple measurements

of different $MASnI_3$ samples. When building the peak model, one should give an interval of values for the E_{bin} of the main peaks. This was determined by calculating the standard deviation of the measured peak position from multiple fresh samples.

Last but not least, the errors of the ratios were estimated by repeatedly measuring a sample in XPS (see Figure 5.2) and calculating the standard deviation of the measured ratios. For components that were absent from that sample, such as oxygen or the second iodine component (which will be discussed in further chapters), the error was estimated to be 10% of the maximum value measured in the series.

3.2.2 X-Ray Diffraction

X-ray diffraction (XRD) gives information about the crystalline structure of a crystal. This technique can be used to estimate the lattice parameter of crystals, the orientation of different grains, and the identification of secondary phases.

The XRD's working principle is based on Bragg's law. Given that in a crystal atoms are arranged in a lattice, they form different periodic planes. When the X-ray light hits the sample, it is scattered by the planes. Constructive interference of the scattered light occurs at specific angles, depending on the distance d between two planes. The angles at which constructive interference occurs follow the Bragg's Law [110],

$$n\lambda = 2dsin\theta, \tag{3.5}$$

where n is the order of the diffraction, λ is the wavelength of the X-ray and θ is the angle of incidence of the X-ray light (see Figure 3.8 (a)).

Each material has specific reflection angles. To identify the measured material and eventual secondary phases, one can compare the obtained spectrum with the spectra in crystallography databases such as [111].

In this project, the XRD configuration used was the $\theta - 2\theta$ configuration, this is the most commonly used XRD technique. In this technique, the angle between the beam of incidence and the detector is twice as large as the angle of incidence θ between the sample surface and the beam (see Figure 3.8 (a)). The advantage of this technique is that it is bulk-sensitive and has a relatively high resolution. All measurements shown in this thesis were made in the $\theta - 2\theta$ configuration.

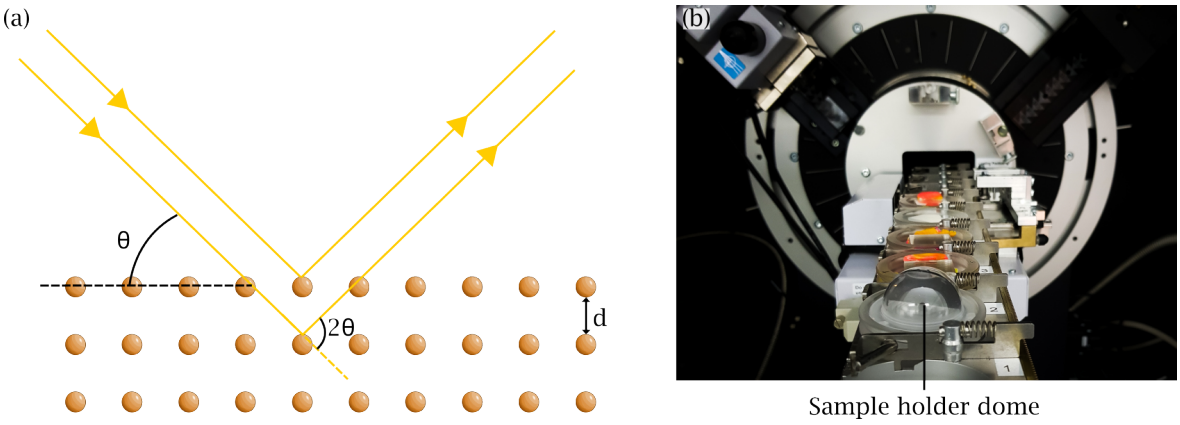

Figure 3.8: (a) Schematic representation of the Bragg's law. (b) Picture of the sample holder dome in the diffractometer.

For samples with a high XRD signal, a Poly(methyl methacrylate) (PMMA) dome was used so that the sample was not exposed to air during measurement (see Figure 3.8 (b)). Nevertheless, for samples that had low XRD signal, the dome was removed so that a greater signal could be obtained.

In the framework of this thesis a Bruker D8 Cu K_α diffractometer was used. The X-ray source was set to a voltage of 40 kV and a current of 40 mA.

3.2.3 Stylus Profilometer

The stylus profilometer is typically used to measure rough samples. Its maximum step size in height is approximately 1 mm. This technique consists of a diamond stylus which scans the surface of the sample in a straight horizontal line while in contact with it. The

vertical movements are recorded and paired with the horizontal movements to form a height profile. More information about the stylus profilometer technique can be found in [112]

Here, this technique was used mainly to measure the thickness of the sample after deposition. The machine used was a Bruker Dektak stylus profilometer, with a tip of 2 μm radius. The force applied by the tip on the surface of the sample was generally set at 3 mg, and the speed was set at 100 μm·s^{-1}. During these measurements, the samples were exposed to air.

To measure the thickness of the $MASnI_3$ films and SnI_2, before the deposition, kapton tape was placed on one of the substrates. The tape was then removed after the deposition, revealing the substrate underneath. The height profile was then measured orthogonally to the kapton tape mark. The error was calculated by repeating the measurement in three different points and calculating the standard deviation. The largest standard deviation of each measurement series was considered the error.

3.2.4 Atomic Force Microscopy and Kelvin Force Probe Microscopy

Atomic force microscopy (AFM) measurements provide a high-resolution, 3D image of the topography of the sample. The operating principle relies on the interaction of an atomically sharp tip with the sample. There are multiple operating modes to this technique, namely the contact mode, the intermittent mode, and the non-contact mode. Here, the mode used was the non-contact mode, which is less damaging to the $MASnI_3$ film. In the non-contact mode, the machine operates in the attractive regime of the Lennard-Jones potential. More specifically, a mechanical oscillation is applied onto the tip within that regime, and the tip-sample interaction is tracked with a lock-in amplifier through the changes in the frequency of resonance of the tip. The AFM measurements were performed in frequency modulation (FM) because the measurements were performed in UHV and the FM mode provides the highest resolution.

Kelvin force probe microscopy measurements (KPFM) were performed simultaneously with the AFM measurements. This was possible by using a second independent lock-in amplifier and applying an AC voltage (V_{AC}) to the tip. The basic working principle of KPFM is based on minimizing the electrostatic force between the tip and the sample. This is done by applying a DC voltage between the tip and the sample that is of the same intensity as the contact difference potential (CPD) between the tip and the sample. The CPD is directly related to the workfunction of the sample ϕ_{sample}. The latter can be calculated using the equation,

$$CPD = \frac{\phi_{sample} - \phi_{tip}}{e}, \tag{3.6}$$

where e is the elementary charge and ϕ_{tip} is the tip workfunction. ϕ_{tip} can be estimated by measuring a clean standard sample of known workfunction. In this case, HOPG was used as a reference sample. The measurements were performed in KPFM FM mode, which tracks the tip-sample force gradient rather than the force itself. This method is slower, but it is less prone to artifacts that are caused by signals from the cantilever.

AFM measurements were performed on the ScientaOmicron variable temperature scanning probe microscope (VT-SPM) UHV system at a pressure in the low 10^{-10} mbar. The KPFM measurements were made in FM-KPFM sideband mode, with an AC voltage of 0.4 V and an oscillation frequency of 965 Hz.

3.2.5 Photoluminescence

Photoluminescence (PL) is a measurement technique that gives information about the optoelectronic properties of materials, especially when it comes to semiconductors. In this thesis, PL was used to measure the bangdap energy and to track sample degradation. Photoluminescence occurs when the material absorbs light, by excitation of an electron from the valence band to the conduction band. In the case where the photon has a higher energy

than the bandgap of the semiconductor, the excited electron loses energy through thermalization. Finally, the electron relaxes back to the valence band and emits a photon of energy corresponding to the bandgap of the semiconductor.

Two setups were used to perform PL measurements. The first setup is the imaging PL. There, the sample was illuminated with a green pulsed laser with a wavelength of 532 nm. The PL signal was then filtered by a liquid crystal tunable bandpass filter, to a range of wavelength intervals, such that a spectrum could be measured. The filtered signal was captured by an InGaAs camera. The advantage of this setup is that it allowed an image of an area of 1 cm×1 cm in the sample. However, this technique shows a lower spectral resolution and the wavelength interval in which it was possible to measure was from 900 nm to 1100 nm, which resulted in an incomplete spectrum of $MASnI_3$. During the measurements, the sample was placed in a box, filled with nitrogen and with a quartz window.

For this reason, a complementary setup was used. This setup had a laser of wavelength 600 nm, and the emitted light from the sample was captured by an InGaAs detector. The detection range of this setup was from 900 nm to 1600 nm which allowed for a more complete PL spectrum of the $MASnI_3$. The advantage of this setup is the good spectral resolution. However, the measured area is one point of radius 1 mm. Additional information about this setup can be found in this article [113].

Chapter 4

Physical Vapor Deposition of $MASnI_3$ and Storage

Perovskites are known to be a relatively easy material to synthesize because complex synthesis methods are not necessarily required. The most common techniques only require spin-coating the precursors and then annealing them in a hot plate [101, 114], which requires a minimal amount of equipment. However, one major drawback of this method is that it requires the use of solvents, which has been correlated with the degradation in perovskite [73].

For this reason, a method that ensures the synthesis of a pure phase directly from the precursors, without the use of solvents, would be of interest. In this context, the use of physical vapor deposition (PVD) is of great interest because it ensures the growth of samples in a pristine environment, with low growth pressures, which allows for meticulous control of the growth conditions.

The aim of this chapter is three-fold:

1. Investigate the impact the growth control parameters, namely the powder's evaporation temperature, the chamber's pressure, have on the grown perovskite ma-

terial by studying their final crystalline structure and their optoelectronic properties.

2. Additionally, the importance of powder purity is highlighted and how this may influence the growth parameters required to achieve similar layer's properties. For this, different powders from different companies were tested.

3. Investigate whether the quality of the stored samples in the glovebox remains stable and quantify the degradation from the storage itself.

4.1 Impact of the co-evaporation parameters

Using PVD, the growth of $MASnI_3$ films is achieved by simultaneously evaporating MAI and SnI_2 powders onto a substrate. The two materials combine to form $MASnI_3$.

As discussed in Chapter 3, during thermal evaporation, MAI has two contributions: the effusion, which is directional, and a second non-directional component. Due to the second component and the low sticking coefficient of MAI, controlling the evaporation rate with QCMs is not possible, and instead the pressure in the chamber was used as the main indicator of the MAI evaporation rate. In fact, the partial pressure of MAI contributed to most of the pressure in the chamber, as evaporating SnI_2 alone at 265 °C, yields a pressure in the chamber of only $7 \cdot 10^{-7}$ mbar which is negligible compared to the pressure obtained when evaporating MAI. Therefore, in this section, the amount of SnI_2 in the chamber during deposition will be discussed in terms of SnI_2 temperature, while the amount of MAI will be discussed as pressure in the chamber (or MAI pressure). All the samples in this section were deposited for the same interval of time, i.e. 90 minutes.

4.1.1 Temperature of SnI_2

To study the effect of the evaporation SnI_2 temperature in the crystalline structure of $MASnI_3$, XRD measurements were performed on freshly deposited $MASnI_3$ samples. A series of four depositions was performed. The pressure of the chamber (i.e. the partial pressure of MAI) was approximately the same during each deposition ($1 \cdot 10^{-5}$ mbar). However, the temperature of SnI_2 was changed from one deposition to another, with temperatures between 260 °C and 275 °C.

XRD measurements are summarized in Figure 4.1. Independently of the SnI_2 temperature, the four deposited films show a strong intensity signal at the angles 14.2 ° and 28.6 °, which correspond to cubic $MASnI_3$ according to the database (PDF-00-064-0961). According to the database, cubic $MASnI_3$ should have more diffraction peaks, here it is not the case because the film grew with preferred orientation. This effect is common in thin films, depending on the growth method [64], and it has also been observed in vapor-deposited $MAPbI_3$ films [56].

The sample for which there was a major difference in the crystalline structure is the one that was deposited with a SnI_2 temperature of 260 °C. In fact, other crystal orientations are visible, namely directions (1 1 1), (2 1 0) and (2 2 0), suggesting less preferential growth. Furthermore, a secondary phase of methylamonium iodide appears, which means that there is excess methylamonium in the crystal that could not react with SnI_2. Excess methylamonium iodide was also previously detected in PVD grown $MAPbI_3$ when using the same MAI powder [59].

On the other hand, the film grown with the highest SnI_2 temperature, 275 °C , had additional peak at $2\theta = 40.1$ °, which according to the database could belong to a monoclinic secondary phase.

Figure 4.2 (a) shows the thickness of the films as a function of the temperature of the SnI_2 source. The thickest film had a thickness of 479 nm and the thinnest was 285 nm, which

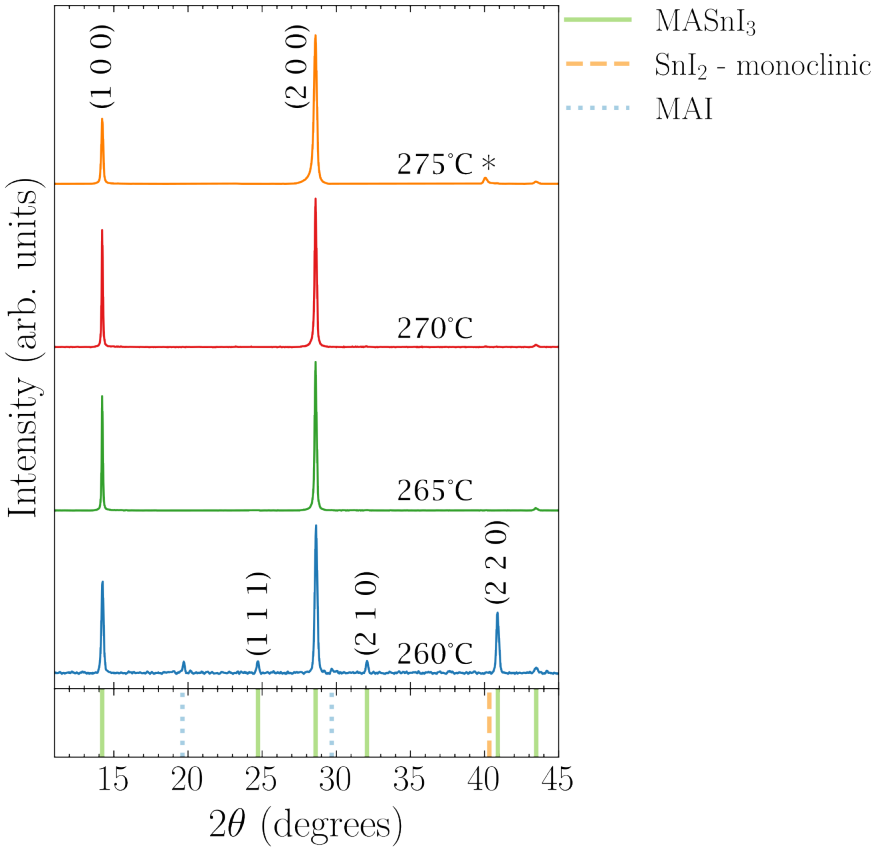

Figure 4.1: Minimum to maximum normalized XRD spectra of $MASnI_3$ deposited with different SnI_2 temperatures and at constant chamber pressure (database files: PDF-00-064-0961, PDF-00-025-0975, [115]).

corresponds to a variation of approximately 40%. As expected, for higher SnI_2 temperatures, the samples were thicker than for lower temperatures.

PL measurements performed on the $MASnI_3$ samples are shown in Figure 4.2 (b). It is visible that the PL peak was approximately at 1.3 eV, which coincides with the optical bandgap reported for $MASnI_3$ [23, 116]. This confirms the observations from Figure 4.1. Furthermore, although for SnI_2 temperatures between 265 °C and 275 °C the PL intensity did not change significantly, for 260 °C, the intensity was significantly lower, showing that there is an optimal range of SnI_2 temperature, below which the PL yield of the film decreases.

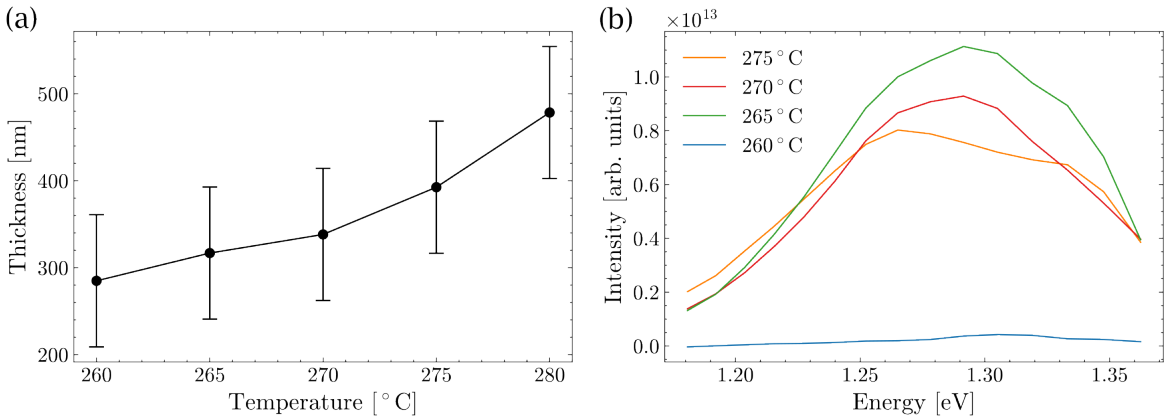

Figure 4.2: (a)Thickness of the $MASnI_3$ film as a function of the temperature of the SnI_2 source. (b) PL of the $MASnI_3$ films for different temperatures of the SnI_2 source.

From this set of measurements, it is clear that $MASnI_3$ was deposited using PVD, both from the XRD signal and the position of the PL peak. Furthermore, it was shown that it is possible to grow films with excess of SnI_2, for high SnI_2 temperature, and with excess of MAI, for low SnI_2 temperature. The film thickness also strongly depended on the temperature of SnI_2. Finally, the PL yield also had a strong dependence on the temperature of SnI_2, as for a low SnI_2 temperature the PL yield reduced significantly.

4.1.2 Pressure in the PVD chamber

The impact of the temperature of SnI_2 during the deposition was studied in the previous section. It was visible that the temperature of SnI_2 affected the crystalline structure, the thickness, and the optoelectronic properties of the film. Here, a similar experiment was performed, where the focus was on the effect of the quantity of MAI in the film. As seen in Chapter 3, although it was not possible to measure the flux of MAI with QCM, the pressure in the chamber could be approximated as the partial pressure of MAI, which was a direct indication of the quantity of MAI in the chamber.

First, XRD measurements were performed to study the impact of the different partial pressures of MAI on the crystalline structure of $MASnI_3$. Figure 4.3 shows the XRD spectra

of four different films all deposited with different MAI pressures, but with constant SnI_2 temperature (265 °C).

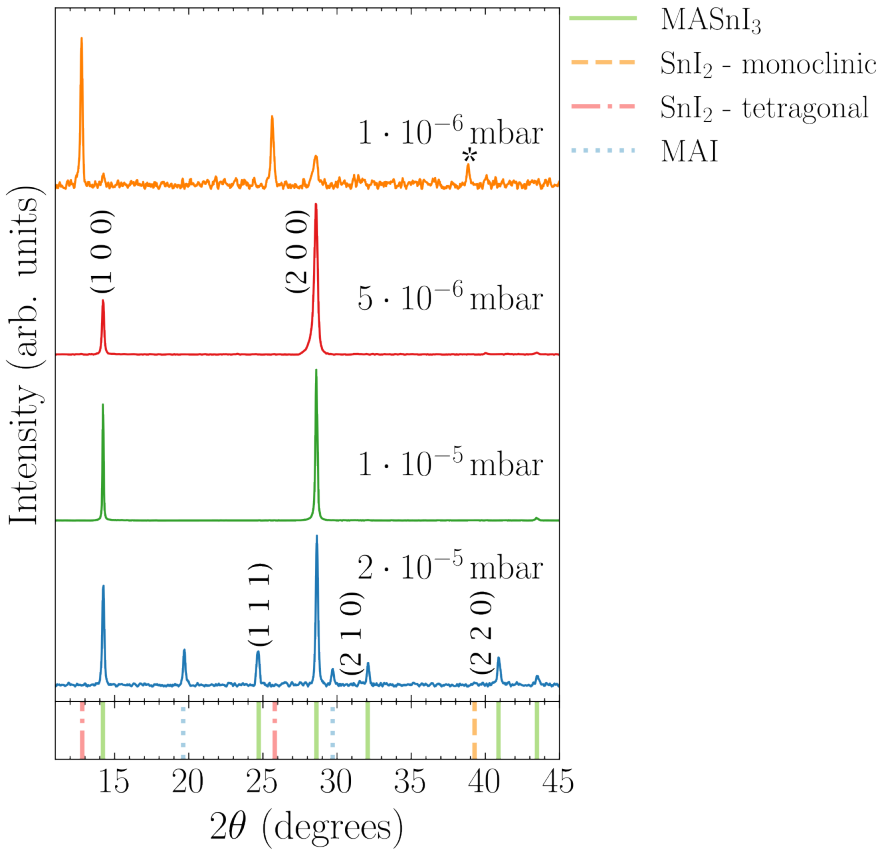

Figure 4.3: Minimum to maximum normalized XRD spectra of $MASnI_3$ deposited at different chamber pressures and with constant SnI_2 temperature (database files: PDF-00-064-0961, PDF-00-025-0975, 00-056-0088, [115]).

Similarly to the series of SnI_2 temperature, here there was a clear preferential growth of the $MASnI_3$ in the (1 0 0) and (2 0 0) planes. For a high MAI pressure, other $MASnI_3$ peaks became visible, namely the (1 1 1), the (2 1 0) and the (2 2 0) directions. In addition, a secondary MAI phase became evident. The behavior of the $MASnI_3$ crystalline structure for a low SnI_2 temperature and for a high MAI partial pressure was similar (Figures 4.1 and 4.3). This suggested that for high pressures, the important point was not the SnI_2 temperature, nor the MAI partial pressure, but instead the ratio of MAI/SnI_2 content in the chamber.

In contrast, for a low MAI pressure, the crystalline structure of the film showed new features. Not only there was the monoclinic SnI_2 secondary phase, but also a strong tetragonal SnI_2 secondary phase. Notice that the monoclinic SnI_2 secondary phase, appeared in both cases (temperature and pressure series) in relatively small quantity. It could be that this was the phase that formed at the interface with the substrate or at the surface of the sample, while the tetragonal phase would be SnI_2 a secondary phase in the bulk, incorporated within $MASnI_3$ grains. As visible, the $MASnI_3$ typical peaks (1 0 0) and (2 0 0) were still visible, but with less intensity.

From the profilometer measurements in Figure 4.4 (a), it was visible that the thicknesses of the deposited $MASnI_3$ films also increased with the MAI pressure. This makes sense because even though MAI had a low sticking coefficient, from the XRD measurements, it was clear that it was possible to deposit MAI in excess, meaning that more material should have deposited on the sample.

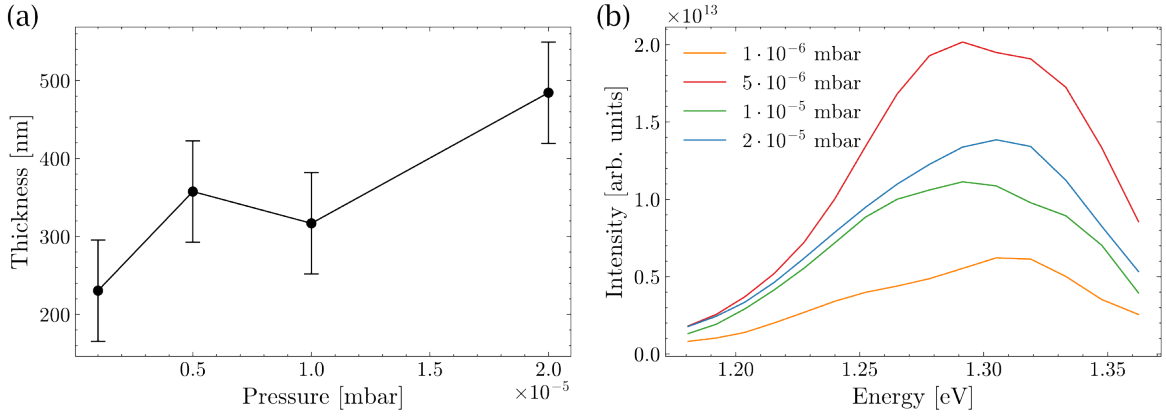

Figure 4.4: (a)Thickness of the $MASnI_3$ film as a function of the the chamber pressure. (b) PL of the $MASnI_3$ films for different chamber pressures.

In the PL measurements Figure 4.4 (b), all samples showed a maximum PL yield intensity of approximately 1.3 eV. Furthermore, the PL yield intensity for all samples was within the same order of magnitude. This means that, when it comes to PL, no significant change was observed.

In this section, it was shown that the crystalline structure of $MASnI_3$ also depends on the MAI partial pressure at constant SnI_2 temperature. However, the results suggest that there is an optimal ratio of MAI/SnI_2 quantities in the chamber. This was clear because the changes in crystalline structure in the SnI_2 temperature measurement series and in the MAI partial pressure measurement series were very similar. The film thickness of $MASnI_3$ also depends on both the SnI_2 temperature and the partial pressure of MAI, but the PL measurements did not show a strong dependence on MAI.

4.2 Comparison of MAI powders from different providers

To study the effect of different powders, three $MASnI_3$ films were deposited with MAI powders from different suppliers. The deposition parameters were similar for each sample, that is, the temperature of the SnI_2 source was kept at 265 °C and the pressure in the chamber was kept at approximately $1 \cdot 10^{-5}$ mbar. Figure 4.5 shows the XRD spectrum of each of the films.

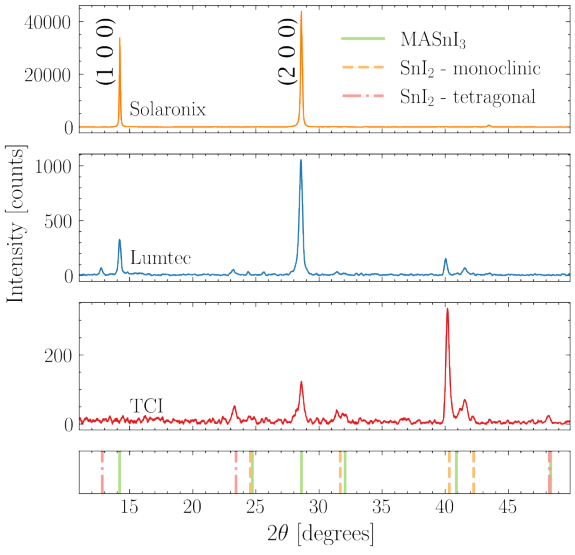

Figure 4.5: XRD of $MASnI_3$ films deposited with powders from three different suppliers (database files: PDF-00-064-0961, PDF-00-025-0975, 00-056-0088).

As visible in Figure 4.5, the spectra of the films of each powder showed considerably different crystalline structures for each sample. The powder provided by Solaronix showed the highest signal and also the strongest preferential direction of growth. However, the other two powders (Lumtec and TCI) resulted in samples with significantly lower signal. Furthermore, both powders show SnI_2 secondary phases. The TCI powder is the powder that produced the sample with the lowest $MASnI_3$ signal and highest SnI_2 secondary phase.

Although the TCI powder resulted in the worst XRD results, it was the powder of choice for the rest of the results in this thesis. The reason was that the TCI powder was reported to be the cleanest powder, which is prioritized here to avoid any contaminants that could degrade the film [117]. Furthermore, it has been reported that tin-based perovskites can show low XRD signal on the same day of deposition, compared to 30 days later [114]. In this case, all samples were measured relatively fresh.

When using the TCI powder, the SnI_2 secondary phase was present in the film for all combinations of parameters that were tested. In order to mitigate the formation of an SnI_2 secondary phase, the deposition method was slightly changed. Instead of keeping the pressure in the chamber constant, by continuously reducing the MAI temperature, the MAI temperature was kept constant after reaching the target chamber pressure. With this method, the pressure of the chamber continuously increased. As a result, the secondary phase in the SnI_2 film decreased significantly but did not fully vanish.

4.3 Effects of a seed layer

In the previous section, the effects of the PVD parameters on the $MASnI_3$ film were studied. As well as the effects of utilizing different MAI powders. It was shown that the MAI powder provided by TCI has significantly less XRD signal than the other two powders. This section studies whether a SnI_2 seed layer would contribute to a higher $MASnI_3$ XRD signal.

In this experiment, an SnI_2 seed layer with a thickness of 100 nm was deposited on a quartz substrate (see Figure 4.6 blue curve). The chamber was then opened to remove half of the substrates with the SnI_2 seed layer for characterization, which were replaced by clean substrates. Therefore, half of the substrates in the sample holder were clean and the other half contained an SnI_2 seed layer. The next step consisted in depositing the $MASnI_3$ film on the substrates. The orange curve shows the $MASnI_3$ sample that was deposited on a seed layer, and the red curve shows the sample that was deposited on a quartz substrate without seed layer. Both samples were deposited during the same deposition. The curves are not normalized for easier comparison. Because all samples were positioned at the same height and measured on the same day, variations due to sample placement and X-ray intensity variation can be ignored.

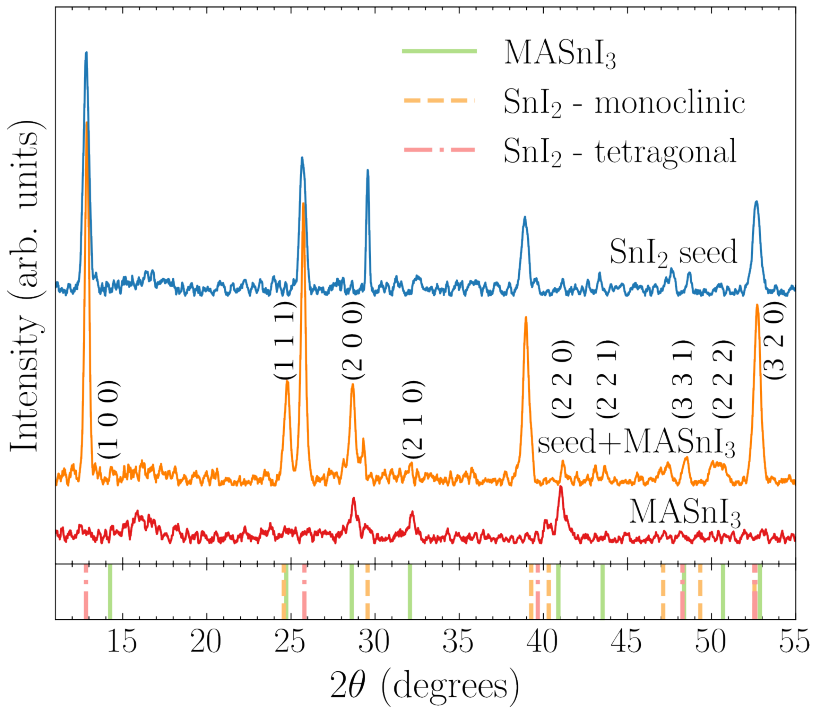

Figure 4.6: Deposition of $MASnI_3$ with and without seed layer. Blue: SnI_2 seed layer. Orange: $MASnI_3$ deposited on top of the seed layer. Red: $MASnI_3$ without seed layer. Both seed layers were deposited simultaneously. Both $MASnI_3$ films were deposited simultaneously (database files: PDF-00-064-0961, PDF-00-025-0975, 00-056-0088).

The SnI_2 seed layer (blue curve) shows two SnI_2 phases, namely a monoclinic phase and a tetragonal phase. The $MASnI_3$ film, deposited on the clean substrate (red curve), shows mainly $MASnI_3$ signal, with a small contribution of monoclinic SnI_2 at $2\theta = 40.32\,^{\circ}$. The XRD signal in this film is considerably low.

Interestingly enough, after depositing MAI on the SnI_2 seed layer film, the SnI_2 signal of the tetragonal phase increased considerably, whereas the signal of the monoclinic phase decreased. Suggesting that the tetragonal phase is more prone to react with MAI to form perovskite compared to the monoclinic phase. Furthermore, the fact that the tetragonal SnI_2 signal increased could indicate two different phenomena: (1) Due to the tetragonal phase of SnI_2 already present in the film, it was not favorable for the MAI to react with the MAI and only SnI_2 was formed, or (2) $MASnI_3$ grew epitaxially to SnI_2, contributing to the SnI_2 peak signal.

Concerning the $MASnI_3$ peaks, for the sample containing a seed layer, it was visible that $MASnI_3$ grew with a different orientation, compared to the sample without seed layer. More specifically, $MASnI_3$ peaks that had reflections close to those of SnI_2 (at 24.7° and 28.6°) had a greater signal in the sample containing a seed layer. Nevertheless, peak that were further away from reflections of SnI_2 vanished or were present in a significantly lower intensity. This means that the use of a seed layer can contribute to the crystal orientation of $MASnI_3$.

In this set of measurements, it was seen that $MASnI_3$ can grow on a SnI_2 seed layer. Although there were some changes in the $MASnI_3$ crystalline structure, this experiment did not result in a strong increase in the XRD signal.

4.4 Presence of PEAI in the $MASnI_3$

Some of the samples used in this thesis were contaminated with PEAI, because this PVD setup was also used for the deposition of samples of phenethylammonium tin iodide ($(PEA)_2SnI_4$). The samples that were studied for the degradation induced by the measure-

ments, water and synthetic air, were contaminated with PEAI (Chapter 5, 7 and 8). This was visible thanks to compositional measurements performed with XPS. This section shows how contamination can be avoided using a preconditioning of the PVD chamber.

4.4.1 Chamber preconditionning

When using the same PVD setup to deposit different materials, it is important to keep in mind the possibility of cross-contamination. To avoid it, a chamber preconditioning might be necessary between the deposition of materials that require different precursors.

To demonstrate the impact of preconditioning of the deposition chamber, the composition of the deposited $MASnI_3$ absorbers was compared for two cases: On the one hand, $MASnI_3$ samples were deposited after a deposition of $(PEA)_2SnI_4$, without any preconditioning. Note that $(PEA)_2SnI_4$ is a 2D-perovskite which uses PEAI as the organic component. On the other hand, $(PEA)_2SnI_4$ was deposited, after which an intermediate step, i.e. preconditioning, was performed before the deposition of $MASnI_3$. The preconditioning consisted in evaporating SnI_2 material for about 1 h, which reacted with the excess PEAI in the chamber and coated the walls of the chamber with SnI_2.

Because $(PEA)_2SnI_4$ presents a stoichiometric ratio of I/Sn=4, $MASnI_3$ samples which contaminated with PEAI were expected to show a I/Sn ratio higher than 3. Figure 4.7 shows the XPS ratios of the samples for which no conditioning was performed prior to their deposition and the samples for which conditioning was performed.

The sample deposited in a non-preconditioned chamber showed a ratio I/Sn = 3.4, which indicates cross-contamination, because the ratio is larger than the stoichiometric ratio of $MASnI_3$ (I/Sn=3)). In contrast, the sample deposited in a preconditioned chamber had a ratio I/Sn=2.3, which was similar to the samples deposited before the introduction of PEAI in the PVD chamber.

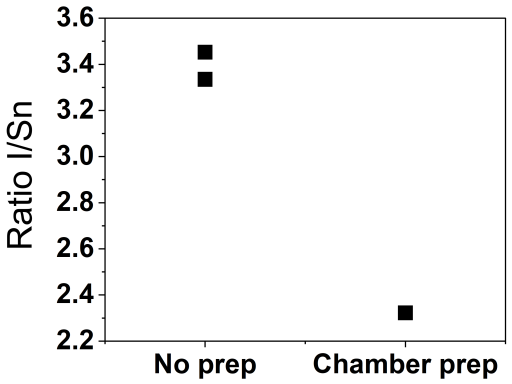

Figure 4.7: Comparison of I/Sn ratio of $MASnI_3$ whith and without chamber preconditioning.

This result highlighted the contamination risk that evaporating material with low sticking coefficients implies for subsequent deposition processes, i.e. the phase purity is compromised. Nevertheless, it was demonstrated that preconditioning the PVD chamber has an impact on the composition of the subsequently grown absorbers.

4.5 Sample storage in a glovebox

The composition of the sample is affected not only by the deposition parameters but also by the storage. As mentioned in Chapter 2, hybrid perovskites are sensitive to oxygen, water, light, and heat. Therefore, it is important to store them such that they are protected from such stresses. For that reason, in the context of this project, all samples were stored in an N_2 glovebox, which was assumed to protect the samples from moisture and oxygen. Note that the glovebox was equipped of O_2 and H_2O sensors and the levels were usually kept below 5 ppm for O_2 and below 2 ppm for H_2O.

To verify this assumption, a study of the compositional evolution of the stored $MASnI_3$ samples, as a function of the glovebox storage time, was carried out. For this, seven sister samples, all from the same deposition, were transferred to XPS in different days after the deposition. The XPS composition ratios of these samples were summarized in Figure 4.8 as

a function of the storage in the glovebox (denote GB) time. During the first 15 days, no major change in the Sn(2+) and Sn(4+) content was observed (see Figure 4.8 (a)). After 23 days in the glovebox, the composition changed noticeably: the Sn(2+) content decreased from approximately 92% to 87% of the total amount of Sn. After 34 days, the Sn(2+) content decreased further to 78%. Looking at Figure 4.8 (b), it is clear that the content of Sn(4+) increased at the same rate that Sn(2+) relative to the total amount of Sn (Sn(tot)) decreased, which means that Sn(2+) converted into Sn(4+).

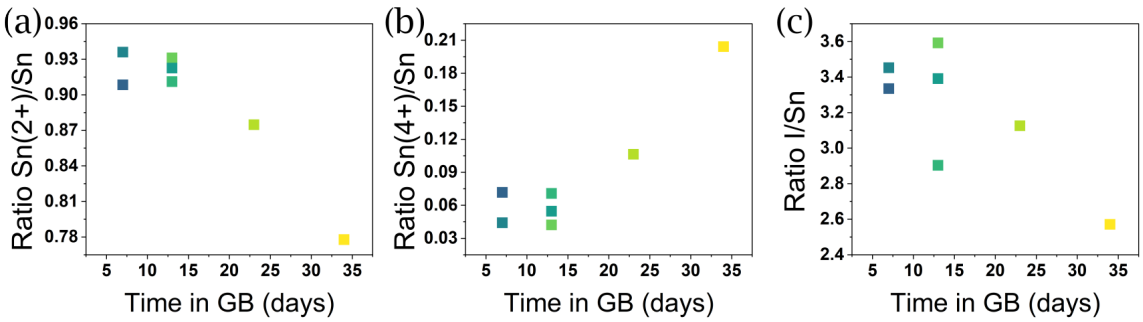

Figure 4.8: Evolution of $MASnI_3$ composition when stored in the glovebox. Evolution of (a) Sn(2+) content, (b) Sn(4+) content and (c) I/Sn ratio.

The iodine content shows more variations in composition, even when the samples remained in the glovebox for the same amount of time. However, in general, the iodine content tends to decrease as a function of the time that the samples remained in the glovebox.

In literature, the formation of Sn(4+) in tin-based perovskites is often associated with the formation of SnI_4 and SnO_2 [63, 92]. Figure 4.8 (c) shows that the I/Sn content tends to decrease as a function of time. If SnI_4 was formed, the I/Sn ratio would have increased because the I/Sn ratio of SnI_4 is 4. Therefore, the compound most likely to form in the glovebox is SnO_2.

In this section the storage of the sample in the glovebox and its impact was discussed. The XPS concentration ratios of the $MASnI_3$ samples were shown to remain at an acceptable composition for the first two weeks. For this reason, samples younger than two weeks are assumed to be ideal for performing experiments, as they have a lower probability of being degraded beforehand.

4.6 Summary

In this chapter, the synthesis of perovskites with various MAI powders and glovebox storage were studied. It is clear that the quality of the crystal and the surface composition are affected by the MAI powder used. Furthermore, it was seen that a low signal in XRD does not necessarily mean a bad surface composition. Cross-contamination was identified and fixed. The glovebox was shown to preserve the $MASnI_3$ samples for approximately 15 days. Most importantly, this chapter justifies the use of the TCI MAI powder in the rest of the thesis.

Chapter 5

Measurement induced degradation of $MASnI_3$

In the previous chapter, it was demonstrated how the deposition parameters influence the composition and crystalline structure of coevaporated tin perovskite. In addition, it was shown that the impact of long-term sample storage in a supposedly inert atmosphere still leads to the degradation of the perovskite material.

The purpose of this chapter is to assess whether the measurement techniques and conditions reported in this thesis lead to the degradation of the measured samples. This is important because one must know how the measurements themselves affect the samples before drawing conclusions.

In the following chapters, samples were repeatedly measured in order to study the degradation of the sample as a function of exposure time to external stresses. Therefore, in this chapter, samples are measured repeatedly, without any external stress other than the measurement conditions, such as X-rays and UHV.

5.1 Vacuum-induced degradation

The first study discussed is a time series in UHV (in the low 10^{-10} mbar) where $MASnI_3$ samples were repeatedly measured in KPFM and XPS directly after deposition and after multiple days of storage in UHV.

Figures 5.1 (a) and (b) show the topography of the sample the same day it was transferred to UHV and after 6 days of storage in UHV, respectively. In both measurements, flat grains of varying sizes were visible. Nevertheless, no significant changes were observed between the two topography measurements.

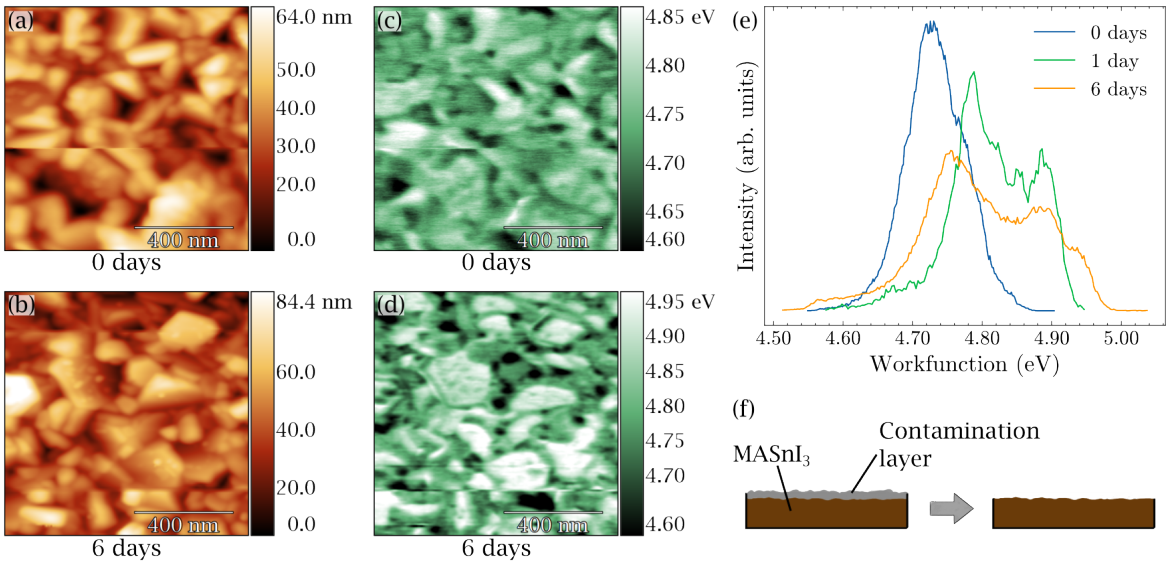

Figure 5.1: AFM measurement of $MASnI_3$ (a) on the day it was moved to UHV and (b) six days later. (c) and (d) KPFM measurements performed simultaneously to the AFM measurements. (e) Normalized workfunction distribution (such that curve integral = 1) of measurements done on day 0, 1 and 6 after placing the sample in UHV. (f) Schematic model that explains the change in the workfunction.

Regarding the workfunction, shown in Figures 5.1 (c) and (d), differences were observed. First, the workfunction in the measurement performed the same day of the transfer (Figure 5.1 (c)) showed a lower facet contrast than the measurement taken after 6 days of storage in UHV (Figure 5.1 (d)). That is, in the latter, the flat surfaces show a higher workfunction

than the rest of the sample. This is not the case for the measurement that was performed on the same day of the transfer. This observation is more clearly visible in Figure 5.1 (e) where the normalized workfunction distribution of the sample was plotted for the same day the sample was placed in UHV and for 1 and 6 days later. Here, it is clear that on the day of the transfer the sample had a lower and narrower workfunction, and already after one day of storage in a UHV, the workfunction shifted to a higher energy and stayed approximately the same values even six days later. The broader distribution was due to the greater contrast that is visible between the different facets of the grains in the sample 5.1 (d).

In fact, as mentioned in the literature, a contaminant layer can significantly change the electronic structure of the surfaces, and as a consequence, the measured KPFM signal [118, 119]. In this case, the sample was initially in N_2 atmosphere and then transferred to UHV. One could hypothesize that a layer of contaminants from the less pure N_2 atmosphere (during glovebox storage) adsorbed onto the surface of the sample reducing the workfunction facet contrast, i.e. the narrow distribution of the workfunction. Upon storage in the cleaner UHV environment, this contaminant layer desorbed from the sample (as depicted in Figure 5.1 (f)), leading to a greater workfunction facet contrast. Thus, the sample does not seem to degrade when stored in UHV; instead, it seems to lose external contaminants, via the desorption of molecules that were adsorbed in the glovebox. Therefore, a $MASnI_3$ sample was measured with XPS on different days after it was stored in UHV. Figure 5.2 shows the evolution of the XPS spectra and ratios as a function of the time the sample stayed in UHV.

Figure 5.2 (a) shows the Sn3d of the sample on the day it was introduced to the UHV (top) and 35 days later (bottom). In between measurements, the sample was always kept in the load-lock chamber (with a pressure of $8 \cdot 10^{-10}$ mbar) with a covered viewport so that there was no stray light in the chamber. The color filled areas correspond to the peak fittings, the lightest brown is for Sn(2+), darkest brown for Sn(0), the color in between for Sn(4+) and gray for the satellite peaks. The envelope is the brown line and the measured data is black.

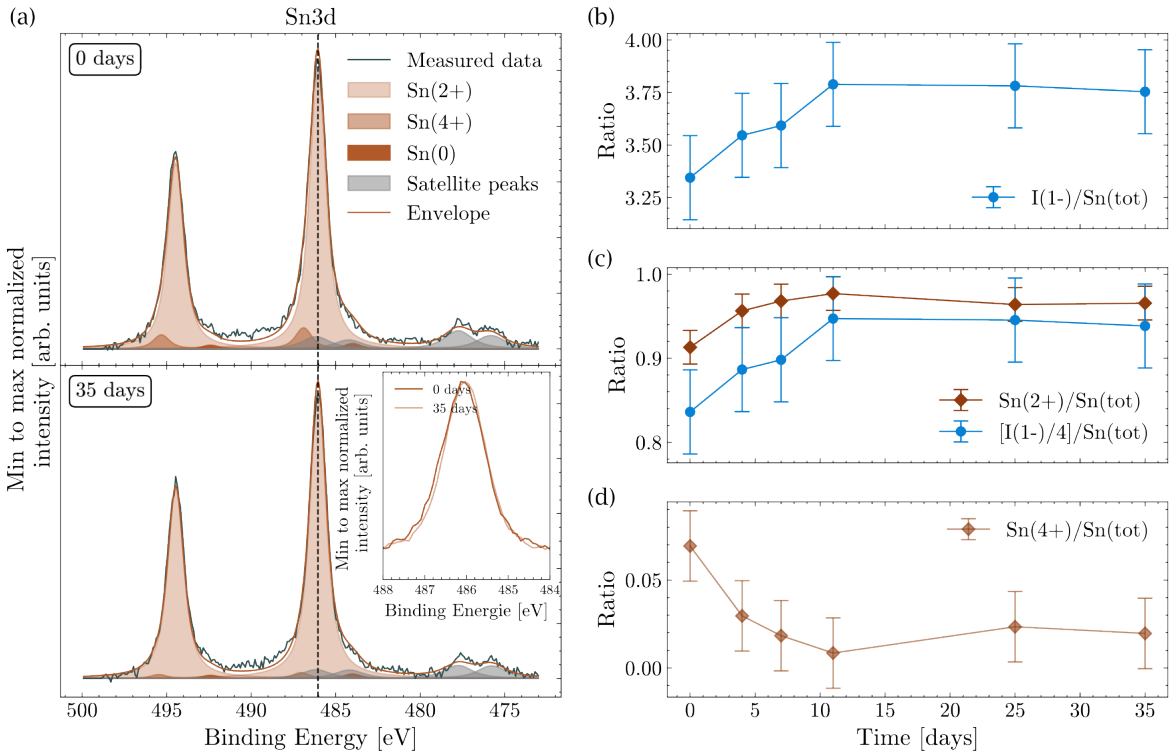

Figure 5.2: $MASnI_3$ vacuum degradation tracked with XPS. (a) Fitting comparison of the first day in vacuum and 35 days later in the Sn3d core level. (b) Evolution of ratio I(1-)/Sn(tot) as a function of storage time in UHV. (c) Comparison of evolution of ratio Sn(2+)/Sn(tot) as [I(1-)/4]/Sn(tot) as a function of storage time in UHV. (d) Evolution of ratio Sn(4+)/Sn(tot) as a function of storage time in UHV.

The main contribution had a value of 486 eV, which corresponds to the binding energy of the Sn oxidation state (2+). This is the oxidation state expected for of Sn in the $MASnI_3$ perovskite. Note that initially the sample already contained some amount of Sn(4+) on its surface. This could be due to contamination in the glovebox. As previously discussed (Chapter 2), in literature, Sn(4+) has been attributed to the presence of SnO_2 or SnI_4 in the material [63, 120]. However, the quantity of Sn(4+) decreased to nearly 0 after 35 h in vacuum. This behavior has previously been observed in 2D perovskites [100] and was attributed to the reduction of Sn(4+) to Sn(2+), which means that the presence of the Sn(4+) oxidation state could be due to contaminants at the surface that later desorbed in the clean UHV atmosphere, as also observed in Figure 5.2. From this there are three different hypothesis,

1. The sample initially contained SnI_4, which in the UHV converted into SnI_2 and I_2;

2. The sample initially contained SnO_2, which converted into SnO + O_2. In this case, Sn would be in the (2+) oxidation state.

3. A contaminant layer from the glovebox adsorbed onto the sample, changing the chemical environment of the topmost perovskite layer.

These spectra are not enough to disentangle the three hypothesis and they will be discussed further later in this section.

For easier comparison, the inset in Figure 5.2 (a) shows the background subtracted raw data on day 0 (blue) and day 35 (orange), without any fitting. We can see that the KPFM measurement performed on the day of the transfer (0 days) had a larger workfunction FWHM than the measurement carried out 35 days later. Since there was no charging in the measurements, i.e. no collective energy shift of all the element peaks, nor any random energy shift between successive sweeps, this slight increase in the workfunction FWHM is evidence of the presence of an additional peak at higher binding energies.

The Sn(0) content is present in negligible amounts, which means that the fitting was equally acceptable regardless of whether the Sn(0) component was considered or not. The Sn(0) peak was kept in the peak fitting for consistency in the analysis of different samples. Interestingly, the Sn(0) peak does not increase significantly, compared to Sn(2+), after 35 days in UHV. This is a surprising behavior, because studies in lead-based perovskites show that in vacuum the absorber tends to form PbI_2 and Pb(0) [70, 95].

In order to disentangle the three hypothesis above, it may be useful to look at the evolution of the different elements of $MASnI_3$ over time, this is shown in Figures 5.2 (b)-(d).

Note that in Figure 5.2 (b), initially the ratio $I/Sn(tot)$ has a value of 3.3 and increases to a value higher than 3.7 after 10 days; after this, the ratio remains mostly constant at a value between around 3.7. This observation must be explained before moving on. Moreover,

it is important to keep in mind that this sample may have suffered cross-contamination during the deposition process, because the PVD chamber was used not only for $MASnI_3$ evaporation, but also for $(PEA)_2SnI_4$, as already discussed in Chapter 4.

For stoichiometric $MASnI_3$, the expected ratio $I/Sn(tot)$ is 3. So, at first glance, the fact that $I/Sn(tot)$ increases to the value of 4 could mean that the material is forming SnI_4, which has a ratio $I/Sn = 4$. However, this contradicts the observations made in Figure 5.2 (a), where the Sn(4+) contribution is small and even decreases with time in vacuum. Moreover, when looking at the ratio $Sn(2+)/Sn(tot)$ (Figure 5.2 (b)), we see that this ratio also increases with time, which also contradicts the formation of SnI_4, in which case the Sn(2+) contribution would be converted to the oxidation state Sn(4+). In fact, this observation is also supported by the fact that the ratio $Sn(4+)/Sn(tot)$ (Figure 5.2 (c)) tends to decrease over time.

Given the possibility of cross-contamination with $(PEA)_2SnI_4$, it is hypothesized that this sample suffered cross-contamination during the cooling down time after the deposition process, when all evaporation sources are switched off. In which case, the contamination would have been caused by the remaining PEAI on the chamber wall. This makes sense because, as discussed in Chapter 4, the PVD chamber is used not only for $MASnI_3$ evaporation, but also for $(PEA)_2SnI_4$. As a consequence, the sample may contain a top layer of $(PEA)_2SnI_4$ on the surface and the expected ratio $I/Sn(tot)$ for the stoichiometric $(PEA)_2SnI_4$ is 4 with Sn in the oxidation state (2+). This explains the higher than expected $I/Sn(tot)$ ratios for $MASnI_3$. A contamination in the bulk does not seem probable, because the PEAI needs to be heated up to higher temperatures than MAI in order to evaporate. Therefore, the vapor pressure in the chamber during the deposition is probably too high for the PEAI to desorb from the walls of the chamber.

To go further, in $(PEA)_2SnI_4$, each Sn atom is bounded to four I atoms and has an oxidation state of (2+). Thus, for pure $(PEA)_2SnI_4$, the following relation between the measured I signal and the Sn(2+) contribution should be verified:

$$\frac{I/4}{Sn(tot)} = \frac{Sn(2+)}{Sn(tot)}. \tag{5.1}$$

For easier comparison, both ratios are plotted in Figure 5.2 (c), where it is clear that both ratios follow the same trend and are very close to each other. The fact that $\frac{I}{4}/Sn(tot)$ is slightly lower than $Sn(2+)/Sn(tot)$ can be explained by the presence of $MASnI_3$ in the sample, which lowers the value of the ratio. Indeed, in the case of pure $MASnI_3$, the following relation holds instead:

$$\frac{I/3}{Sn(tot)} = \frac{Sn(2+)}{Sn(tot)}. \tag{5.2}$$

Returning to the three hypotheses mentioned above. The first hypothesis suggested the presence of SnI_4 from the beginning, which would convert into SnI_2 and I_2 in UHV. Nevertheless, the I_2 is known to leave the perovskites' surface in UHV [34, 35, 121], and therefore, a decrease in iodide content would be expected. However, the iodide content increased, meaning that the first hypothesis can be discarded.

Unfortunately, from these measurements it was not possible to disentangle the second hypothesis (i.e. SnO_2 converting into SnO and O_2) from the third hypothesis (i.e. the presence of a contamination layer that interacted with Sn, slightly changing its binding energy). Oxygen was observed in the film with an approximate ratio $O/Sn(tot) = 0.2$ (see Figure A1), but its evolution does not follow the evolution of Sn(4+) close enough to justify the second hypothesis. Similarly, the presence of a contaminant carbon species was detected, with an approximate ratio of $C/Sn(tot) = 1.2$ (see Figure A1), but its trend did not follow that of Sn(4+) close enough. Therefore, it is possible that the combination of both hypotheses is the reason for the variations observed.

From the KPFM and XPS measurements, one can conclude that there is no clear evidence of degradation due to UHV. More precisely, in both cases, the sample seemed to get

rid of contaminants that might have adsorbed during storage in the glovebox. Once the contaminants left the surface, the composition of the sample did not change, this has also previously been observed in literature [97]. Furthermore, it was observed that the sample was contaminated with PEAI. Samples from the same batch were used in later chapters, namely Chapters 7 and 8.

5.2 X-ray induced degradation

On the basis of the above analysis, XPS seems to be a good technique for tracking perovskite degradation. First, it is a surface sensitive technique and, second, from the measurements seen in Figure 5.2, the sample composition does not show any evidence of degradation in the sample due to the measurement technique. However, XPS does not give any information about the bulk or about defects, and therefore this technique can be complemented with PL measurements.

The sample that was used, in the previous section, to study the vacuum degradation, was repeatedly measured in XPS. Similarly, samples that were exposed to other external stimuli, such as water and oxygen, were also repeatedly measured in XPS. The UHV sample holder, used for XPS measurement, contained two stainless steel clamps that hold the sample in place (see Figure 5.3 (a)). Therefore, part of the sample was under the clamps and shielded from X-rays, while it was in UHV. Only the border of the clamps was in contact with the sample, so a gap would remain between the sample and the rest of the clamp, as illustrated in Figure 5.3 (a). Consequently, when the sample was removed from the holder, two regions were distinguishable: (1) the region under the clamp (protected from X-rays) and (2) the rest of the sample (exposed to X-rays).

The different colors were difficult to capture in an optical image, but they were clearly visible in the PL imaging setup. Figure 5.3 (b) shows the PL map of the sample used for the UHV stability experiment, discussed above (Figure 5.2). The relative location where the

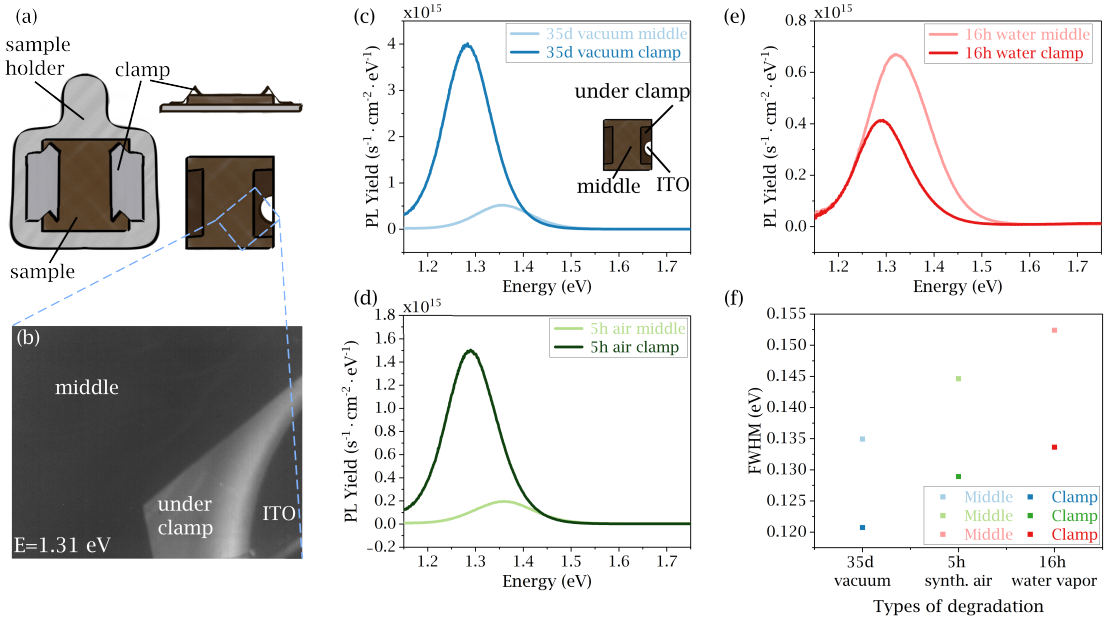

Figure 5.3: PL measurements performed after XPS. (a) XPS sample holder, top view (left), bottom view (top right), different color zones after XPS measurement (bottom right). (b) PL image of the X-ray-induced degradation sample after XPS measurements with spectrometer set to $E = 1.31\,\text{eV}$. (c)-(e) PL measurement below the clamp and at the center of the sample after different degradations and XPS measurement. (f) FWHM of the PL peak for each spectrum in (c)-(e).

measurement was taken is also shown in (a) with a blue outline. The map was acquired with liquid crystal filter set to E=1.31 eV to highlight the contrast between the two regions of interest. Clearly, the region under the clamp has the photoluminescence that is greater than that of the rest of the sample. To compare the photoluminescence yield between the two regions, intensity-calibrated PL was measured from the two regions of interest and the resulting spectra are plotted in Figure 5.3 (c). Here, a pronounced reduction of the PL yield is observed at the center of the sample (light blue spectrum), compared to that observed in the region under the clamp (dark blue spectrum). Additionally, a peak shift toward higher energies is noted. Furthermore, two additional samples from the same batch as the previous sample were exposed to different stresses, namely 5 h of synthetic air and 16 h of water vapor, measured with XPS and then measured in PL (Figures 5.3 (d) and (e) respectively). Both samples show an energy shift of the PL peak towards higher energies at the center of

the sample, comparatively to the region under the holder's clamps, independently of their previous degradation.

Furthermore, Figure 5.3 (f) shows the FWHM of the PL spectra of the three sister samples in the region below the clamp (darker color) and at the center of the sample (lighter color). The FWHM were extracted using a Gaussian fitting. Here, it is clear that, independently of the type of degradation, the FWHM of the PL peak further increases when the sample is exposed to X-rays. Typically, a change in the PL peak position and a variation in the FWHM mean that the film's composition changed, but in the XPS it was shown that the composition of the sample did not vary significantly (Figure 5.2). However, one should keep in mind that in order to perform PL, the sample underwent multiple transfers, which could have exposed the sample to small amounts of air and moisture. To better understand the observations in PL, profilometer measurements were performed on the sample that was exposed to synthetic air for 5 h (see Figure 5.4).

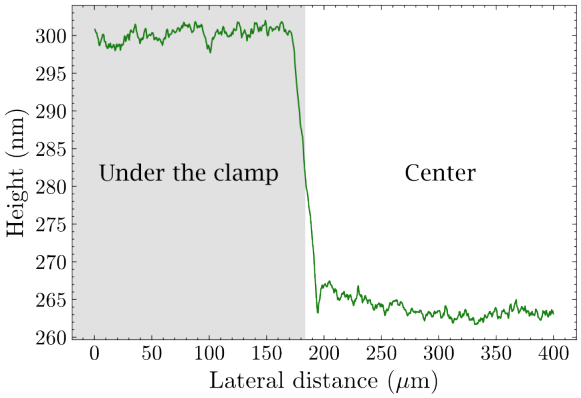

Figure 5.4: Profilometer of perovskite in the region shielded from X-rays (under the clamp) and in the region exposed to the X-rays (center).

Notice that the part of the sample that was below the clamp, and shielded from the X-rays, was thicker than the region that was exposed to the X-rays. The difference in thickness was approximately 35 nm. That is, the uncovered part of the film evaporated during exposure to X-rays. Due to this evaporation, vacancies could have formed in the sample, making it more vulnerable to degradation. This goes in the same direction of what is observed in

the literature [97, 98], where the exposure of perovskites to X-rays have been linked to the formation of defects. Recalling that to perform PL on the sample, multiple transfers were implied, some of which were in N_2 atmosphere, it could be that the sample was exposed to oxygen and water in small amounts. This would result in oxidation of the sample, leading to a change in composition, which could explain the PL peak shift and the observed change in FWHM.

From this set of measurements, it is clear that X-ray exposure causes evaporation of the sample, without causing a significant change in the composition of the sample. Furthermore, the sample evaporation, combined with the multiple transfers, resulted in the degradation of the sample, which was identified through a decrease in PL yield, a PL peak shift, and an increase of the FWHM of the PL peak.

5.3 Summary

In this chapter, it has been shown that even in the N_2 glovebox and in the PVD, the sample is not fully protected from contaminants. Indeed, the latter adsorbed onto the sample surface and contributed to workfunction and the composition measurements signal. According to XPS measurements, the contaminant signal can take up to 10 days to vanish if the sample is kept in UHV. KPFM measurements and UHV itself were not observed to degrade the tin perovskite, and X-ray exposure has been shown to not change the surface composition significantly. However, the thickness of the samples that were exposed to X-raz radiation reduced through evaporation, making the sample more prone to contamination.

Chapter 6

Light induced degradation of $MASnI_3$

In the previous chapters, degradation induced by the storage and measurement techniques was studied. It was concluded that the degradation induced by the measurements did not have a significant impact in the measured composition of sample and that when stored in the glovebox, the sample would undergo significant degradation 15 days after the deposition. After which, the formation of Sn(4+) was detected. With this knowledge, XPS and KPFM seem to be the appropriate techniques to study the degradation induced by exposure to light.

Why is light degradation interesting and why should it be studied? If Sn-based perovskites are ever employed as absorbers in solar cell devices, it is crucial that they do not degrade upon illumination, in order to guarantee their performance in the long term. Currently, the perovskite community agrees that MA^+ is leaving the surface upon illumination [62, 76, 77], but there is no clear consensus on which degradation products remain on the sample [62, 78, 79]. Thus, it is of great interest to understand the light-induced degradation mechanism of Sn-based perovskites.

For this, composition measurements were performed after the sample was exposed to light for different intervals of time. In total, the sample was illuminated for 61 h in UHV. The composition measurements revealed the presence of SnI_2 in the sample from the beginning. With this in mind, the light degradation study is performed and modeled on the basis of a bilayer model. Finally, the light-induced degradation mechanism observed here in Sn-based perovskites is compared to that of Pb-based perovskites.

6.1 Light-induced degradation of $MASnI_3$

To study the light-induced degradation of $MASnI_3$, a pristine sample was measured in XPS and then exposed to light for different time intervals. The light used for degradation was a white light (the QTH10 from Thorlabs) and the irradiance was of 16 mW/cm^2 which corresponds to 0.16 suns. Between each interval of exposure, the sample was measured in XPS.

Note that the sample was exposed to light in the XPS chamber. There were no transfers and the sample was not moved for the full duration of the experiment. Therefore, reducing the chances of carbon and nitrogen contamination. For this reason, in this chapter, the nitrogen (N1s) and carbon (C1s) peaks were taken into account.

First, the pristine sample mainly showed the oxidation state Sn(2+) at $E_{binding}$ = 486.1 eV (see Figure 6.1 (a) (top)). Surprisingly, after exposure of the sample to light for 61 h, the binding energy of tin remained the same, which meant that tin was mainly in the oxidation state Sn(2+) (see Figure 6.1 (b) (bottom)). Only a slight increase in the Sn(0) quantity was detected, which is highlighted in the inset of the figure. Note that no Sn(4+) formation was detected.

When considering the I3d signal (see Figure 6.1 (b) (top)), the pristine sample showed the main peak at the binding energy $E_{binding}$ = 618.8 eV, which is expected for $MASnI_3$. Nevertheless, the ratio $I/Sn(tot)$ was especially low, with a value of 2.3 instead of 3. As

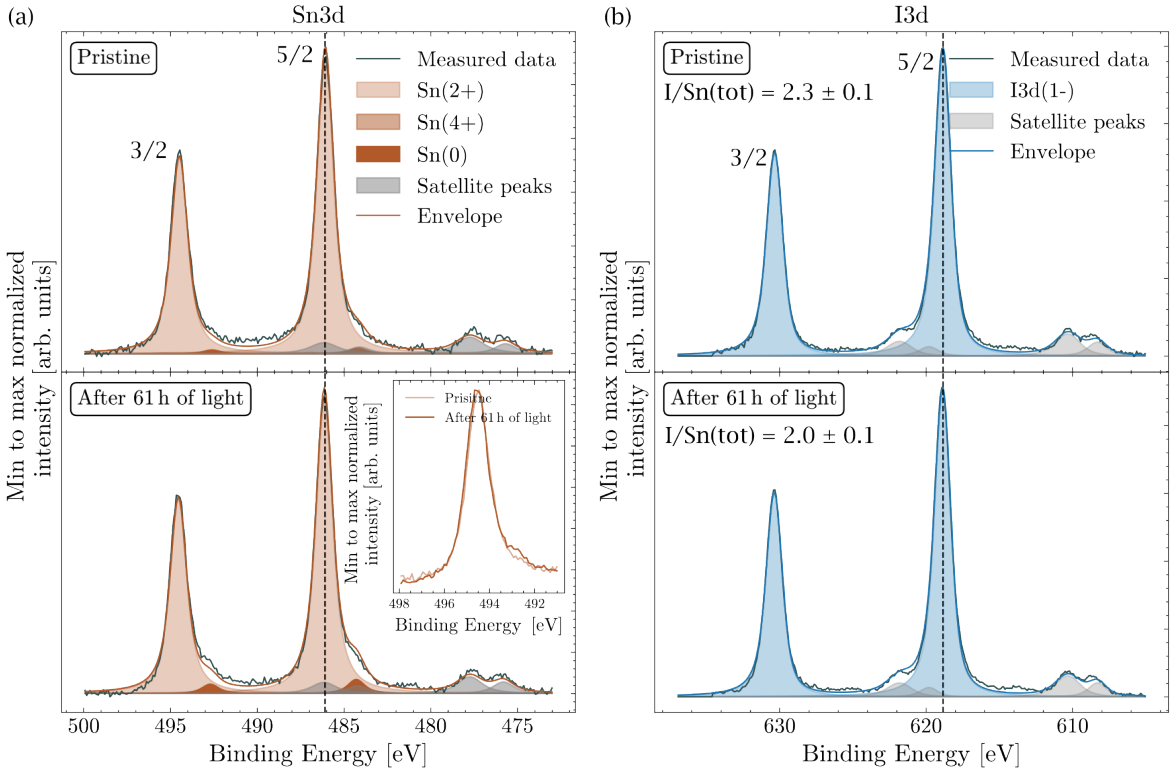

Figure 6.1: Spectra of pristine $MASnI_3$ (top) and light exposed $MASnI_3$ (bottom). (a) Spectrum in the Sn3d energy region and (b) in the I3d region.

mentioned in the deposition chapter (Chapter 4), this was assigned to the presence of SnI_2 in the film, and it will be discussed in more detail in the next section. After illumination (Figure 6.1 (b) (bottom)), no difference in the spectrum was detectable, however, the ratio $I/Sn(tot)$ decreased to 2.0, which could be an indication of the formation of SnI_2. Recall that the oxidation states Sn and I are identical for $MASnI_3$ and for SnI_2, as a consequence, it is not possible to deconvolute the two contributions.

The nitrogen spectrum showed the most visible change after exposure to light. Figure 6.2, shows the nitrogen spectra before and after light exposure. As seen in Chapter 4, the pristine sample shows two nitrogen peaks. Nevertheless, the low energy nitrogen peak was also observed in SnI_2 films. Therefore, the highest binding energy peak (denominated N_{high}) was assigned to the perovskite signal, while the lower binding energy peak (N_{low}) was attributed to contamination. Note that after exposure to light, the intensity of the N_{high}

peak decreased, suggesting a decrease in the MA^+ content and as a consequence, a decrease in perovskite content, again indicating the formation of SnI_2. Note that this is in agreement with literature, as MA^+ has been reported to leave the perovskite's surface upon illumination both in Sn- and Pb-based perovskites [62, 76, 77]

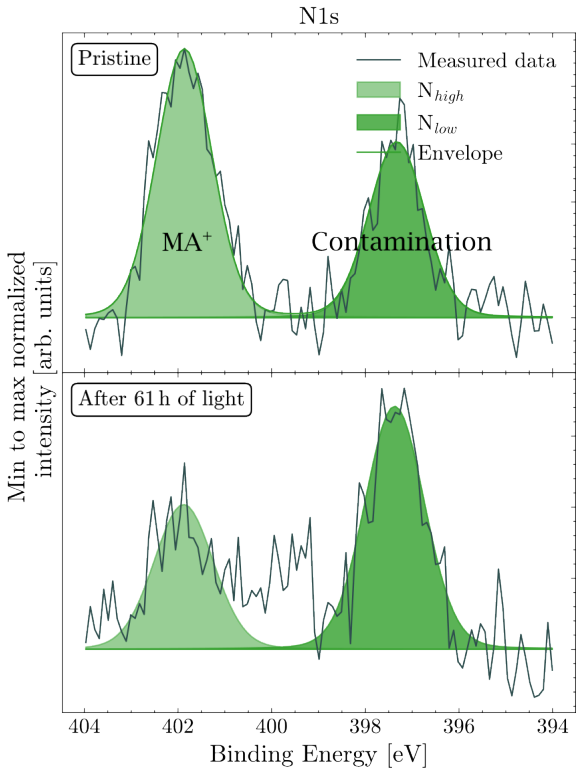

Figure 6.2: Spectra of pristine $MASnI_3$ (top) and light exposed $MASnI_3$ (bottom) in the N1s energy region.

KPFM has previously been used in the literature to detect secondary phases in perovskites [59]. Here, the XPS measurements indicated that a secondary SnI_2 phase was present in the sample. In this case, regions with two distinct workfunctions (SnI_2 and $MASnI_3$) were expected to be apparent in the KPFM measurement. However, this was not the case (see Figure 6.3).

In fact, not only there is no clear sign of a secondary phase in the sample, but the average workfunction of the degraded sample only varies by 20 meV compared to the pristine sample.

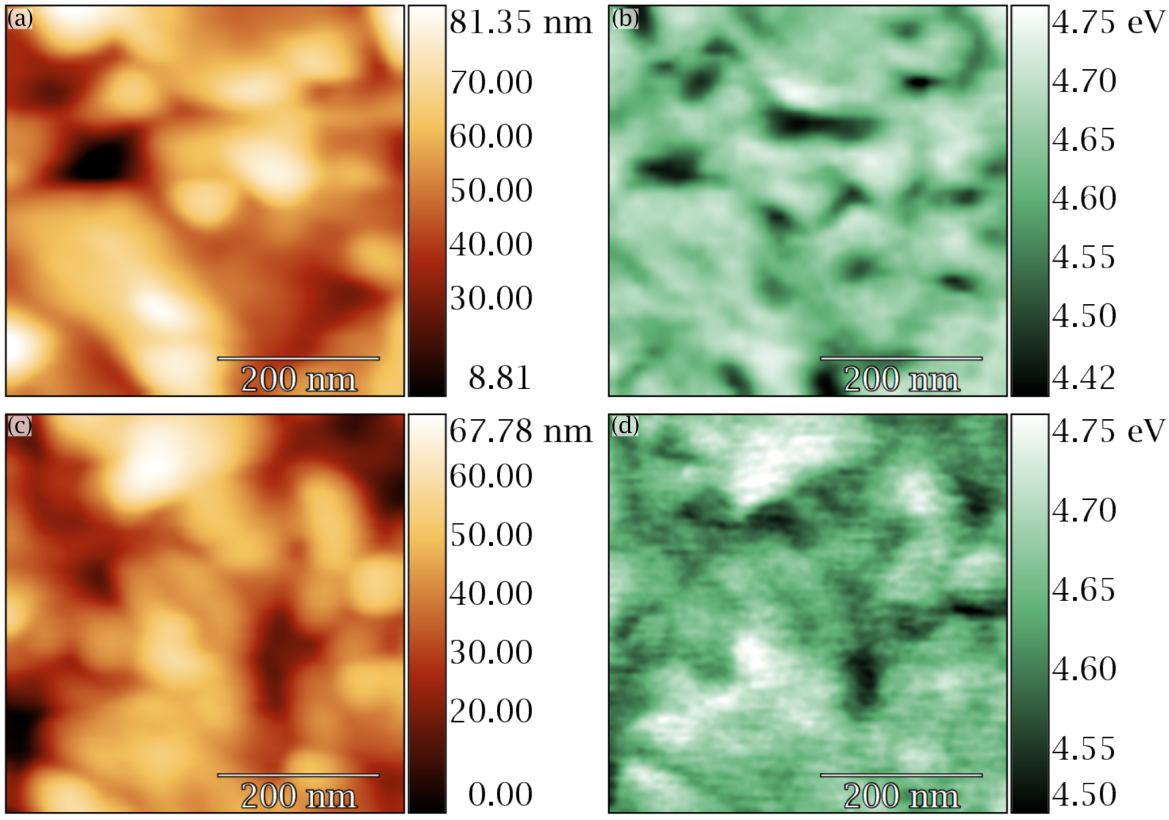

Figure 6.3: (a) Topography and (b) workfunction maps of a pristine $MASnI_3$ sample. (c) Topography and (d) workfunction maps of a light exposed $MASnI_3$ sample.

More precisely, the average workfunction of $MASnI_3$ goes from $4.63eV$ in the pristine sample to 4.61 eV after illumination.

Assuming that SnI_2 and $MASnI_3$ do not have the same workfunction and given that the secondary phase is not detectable in the KPFM measurements and both samples have the same workfunction, it is safe to assume that the pristine sample had an SnI_2 top layer at the beginning of the experiment. During exposure, this layer increased in thickness, reducing the $MASnI_3$ signal. In this case, a bilayer model could describe the increase in thickness of the SnI_2 layer. In the next section, a layer-by-layer degradation of $MASnI_3$ is assumed in order to derive a bilayer model that is adpated to this system.

6.1.1 Bi-layer model

Assuming that $MASnI_3$ degrades layer-by-layer into SnI_2 starting from the surface, one can estimate the evolution of the layer thickness as a function of time. To do so, it is necessary to look at the evolution of the ratios I(1-)/Sn(tot), N_{high}/Sn(tot), and C/Sn(tot), which are plotted in Figure 6.4.

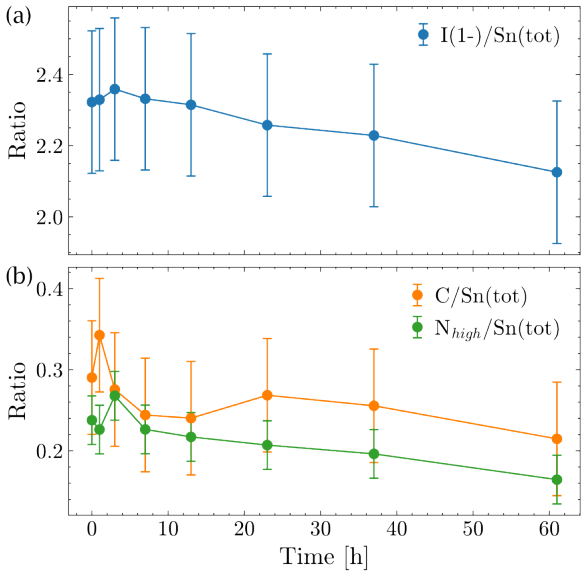

Figure 6.4: (a) Evolution of I(1-)/Sn(tot) (b), C/Sn(tot) and N_{high}/Sn(tot).

When $MASnI_3$ sample is exposed to light, the ratios I(1-)/Sn(tot), N_{high}/Sn(tot), and C/Sn(tot) decrease as a function of time. This could be explained by MAI, which leaves the surface of the sample, and by the formation of SnI_2 as a product of the reaction. The chemical reaction of the degradation would go as follows.

$$MASnI_3(s) \xrightarrow{h\nu} MAI(g) + SnI_2(s). \tag{6.1}$$

Note that in the first 5 h the ratio increases; this was previously observed (in Chapter 5) and was attributed to a layer of external contaminants that desorb from the surface of the sample when the sample is placed in vacuum.

The data in Figure 6.4 can be used to estimate the evolution of the thickness of the SnI_2 layer as a function of time. To do so, it is necessary to derive a bi-layer model that can describe this system. In the following, the bi-layer model is derived in order to describe the decrease of the different ratios.

Suppose that the $MASnI_3$ sample has a homogeneous layer of SnI_2 at the surface. Then, for a layer that is thinner than the probing depth of the XPS (i.e. approximately 8 nm to 10 nm), the XPS signal contains two contributions: one contribution from the surface material (here SnI_2) and another one from the bulk material ($MASnI_3$ in this case). Here, the aim is to use the bi-layer model to estimate the thickness d of the SnI_2 layer as a function of time. From the book by Hofmann and Siegfried, the corrected intensity of Sn I_{Sn} measured in XPS is given by [68]

$$I_{Sn} = I_{Sn}^{s}\left[1 - \exp\left(\frac{-d}{\lambda_{Sn}\cos\theta}\right)\right] + I_{Sn}^{b}\exp\left(\frac{-d}{\lambda_{Sn}\cos\theta}\right). \tag{6.2}$$

Here, I_{Sn}^{s} is the mole fraction of Sn in the surface material and I_{Sn}^{b} the mole fraction of Sn in the bulk, θ is the angle between the analyzer lenses and the sample surface normal and λ_{Sn} is the attenuation length of Sn electrons in the surface material. The attenuation

length includes the elastic scattering and the inelastic scattering; nevertheless, here it is approximated by the inelastic mean free path (IMFP) which neglects the elastic scattering and introduces an error of 10%-15% [68]. The IMFP for the different elements were calculated with the TPP2M model [122].

Note that Equation 6.2 consists of two terms: the surface contribution, which increases exponentially with thickness d, and the bulk contribution, which decreases exponentially with thickness d. This equation can be written more generally for any element x in the sample as

$$I_x = I_x^s \left[1 - \exp\left(\frac{-d}{\lambda_x \cos\theta}\right)\right] + I_x^b \exp\left(\frac{-d}{\lambda_x \cos\theta}\right).$$

In this experiment, the sample was placed orthogonally to the lenses of the analyzer, therefore $\theta = 0$. As a consequence, the ratio I_x/I_{Sn} between the element x and Sn is given by

$$R_{x,Sn} = \frac{I_x}{I_{Sn}} = \frac{I_x^s \left(1 - e^{-d/\lambda_x}\right) + I_x^b \cdot e^{-d/\lambda_x}}{I_{Sn}^s \left(1 - e^{-d/\lambda_{Sn}}\right) + I_{Sn}^b \cdot e^{-d/\lambda_{Sn}}}. \tag{6.3}$$

The mole fractions of I and Sn in the bulk are especially hard to estimate because there are no reference samples $MASnI_3$. However, by taking the chemical formula of $MASnI_3$ into account, one can use the values expected for the ratios of the mole fractions.

Defining, the ratio of the volume density of Sn in the bulk to that on the surface can be calculated by dividing the quantity of Sn present on the surface by the quantity of Sn in the bulk

$$\rho_{Sn} = \frac{I_{Sn}^s}{I_{Sn}^b} \Rightarrow I_{Sn}^s = \rho_{Sn} I_{Sn}^b \tag{6.4}$$

Furthermore, let R_{surf} be the ratio between the quantity of x and Sn at the surface and R_{bulk} the ratio between the quantity of x and Sn in the bulk. Then,

$$R_{surf} = \frac{I_x^s}{I_{Sn}^s} \Rightarrow I_x^s = R_{surf} I_{Sn}^s = R_{surf} \cdot \rho_{Sn} I_{Sn}^b \tag{6.5}$$

and

$$R_{bulk} = \frac{I_x^b}{I_{Sn}^b} \Rightarrow I_x^b = R_{bulk} I_{Sn}^b. \tag{6.6}$$

Here, the mole fractions in Eq. 6.3 can be replaced by results in Eq. 6.4, 6.5 and 6.6 so,

$$R_{x,Sn} = \frac{R_{surf} \cdot \rho_{Sn} I_{Sn}^b \left(1 - e^{-d/\lambda_x}\right) + R_{bulk} I_{Sn}^b \cdot e^{-d/\lambda_x}}{\rho_{Sn} I_{Sn}^b \left(1 - e^{-d/\lambda_{Sn}}\right) + I_{Sn}^b e^{-d/\lambda_{Sn}}} \tag{6.7}$$

By simplifying I_{Sn}^b,

$$R_{x,Sn} = \frac{R_{surf} \rho_{_{Sn}} \left(1 - e^{-d/\lambda_x}\right) + R_{bulk} \cdot e^{-d/\lambda_x}}{\rho_{_{Sn}} \left(1 - e^{-d/\lambda_{Sn}}\right) + e^{-d/\lambda_{Sn}}}. \tag{6.8}$$

This equation can be adapted to the different elements in $MASnI_3$. For iodide, given that the surface layer is SnI_2 and the bulk is $MASnI_3$, then $R_{surf} = 2$ and $R_{bulk} = 3$ therefore

$$R_{I,Sn} = \frac{2\rho_{_{Sn}} \left(1 - e^{-d/\lambda_I}\right) + 3e^{-d/\lambda_I}}{\rho_{_{Sn}} \left(1 - e^{-d/\lambda_{Sn}}\right) + e^{-d/\lambda_{Sn}}}. \tag{6.9}$$

Carbon and nitrogen are not present in the surface material, so $R_{surf} = 0$ and for the bulk, the ratio is $R_{bulk} = 1$, which implies

$$R_{C,Sn} = \frac{e^{-d/\lambda_C}}{\rho_{Sn}\left(1 - e^{-d/\lambda_{Sn}}\right) + e^{-d/\lambda_{Sn}}}. \tag{6.10}$$

and

$$R_{N,Sn} = \frac{e^{-d/\lambda_N}}{\rho_{Sn}\left(1 - e^{-d/\lambda_{Sn}}\right) + e^{-d/\lambda_{Sn}}}. \tag{6.11}$$

The ratio ρ_{Sn}, can be determined either from the tabulated values of the crystalline structures of SnI_2 and $MASnI_3$, or by fitting the data in Figure 6.4.

In order to fit the data with the derived equations 6.9, 6.10 and 6.11, it is necessary to find the dependence of d in time. Notice that the thickness d is a function of the illumination time t, because it was assumed that the sample degraded layer by layer. Additionally, since the sample was measured to be 300 nm, which is two orders of magnitude thicker than the SnI_2 layer, the content of $MASnI_3$ can be considered an infinite reservoir. Consequently, the degradation reaction was assumed to be linear in time and so [123], the thickness d also has a linear dependence on time: $d(t) = d(0) + b \cdot t$. Here, d(0) is the thickness of the SnI_2 at $t = 0$ and b is the decomposition rate of $MASnI_3$. The fitting was optimized such that $d(0)$, b and ρ_{Sn} would be free parameters, with the same value in all three data sets, i.e. I(1-)/Sn(tot), C/Sn(tot) and N_{high}/Sn(tot) as a function of light exposure time. Figures 6.5 (a) and (b) show the ratios fitted with the derived model and the thickness estimation in Figure 6.5 (c).

As a result of the fitting, the initial thickness of SnI_2 $d(0)$ was estimated to be $1.4 \pm 0.1 nm$ and increased at a rate of $b = 0.014 \pm 0.003 nm \cdot h^{-1}$. Furthermore, after $61h$ exposure to light, the SnI_2 thickness reached a value of $d(61h) = 2.3 \pm 0.3 nm$, which is only 1 nm more than the initial quantity. Finally, the ratio ρ_{Sn} was estimated to be 2.71 ± 0.33.

To verify this result, the ratio ρ_{Sn} can also be estimated with the tabulated values. The volume density of Sn atoms in the surface material can be defined as

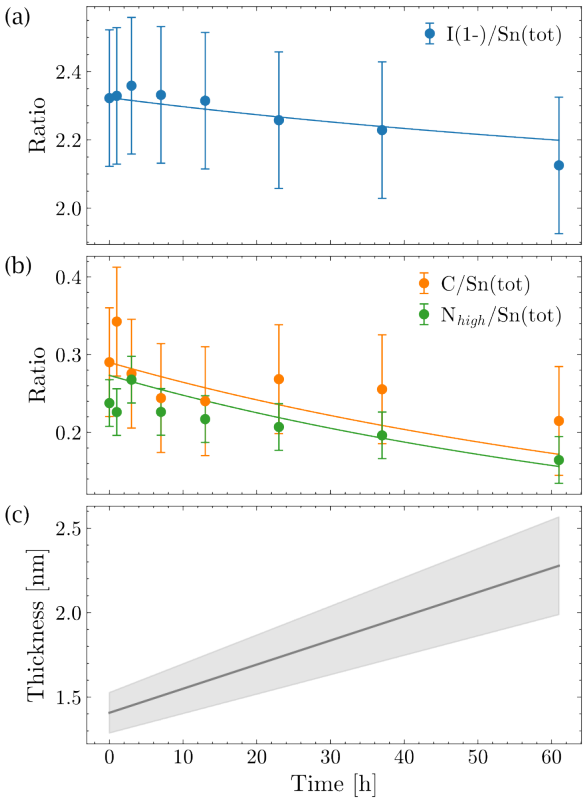

Figure 6.5: Fitting of evolution of (a) I(1-)/Sn(tot) (b), C/Sn(tot) and N_{high}/Sn(tot) with the bi-layer model. (c) Estimation of thickness of SnI_2 as a function of time.

$$\rho^s_{Sn} = \frac{N^s_{Sn}}{V^s_{Sn}} \tag{6.12}$$

With N^s_{Sn} the number of Sn atoms in a unit cell of the surface material and V^s_{Sn} the volume of a unit cell. If the mole fraction of tin I^s_{Sn} and ρ^s_{Sn} are proportional to each other, then

$$I^s_{Sn} = \alpha \cdot \rho^s_{Sn} = \alpha \cdot \frac{N^s_{Sn}}{V^s_{Sn}} \tag{6.13}$$

with α the proportionality factor. Assuming that the material at the surface of the film is monoclinic SnI_2, then from the XRD database for this crystalline structure it is possible

to extract $N^s_{Sn} = 6$ $V^s_{Sn} = 349.03$ Å^3 [124]. The value of N^s_{Sn} was obtained by simulating the crystalline structure in VESTA using the database file.

Using the same reasoning for the bulk material,

$$I^b_{Sn} = \alpha \cdot \rho^b_{Sn} = \alpha \cdot \frac{N^b_{Sn}}{V^b_{Sn}} \tag{6.14}$$

The bulk material is $MASnI_3$, was measured to be in the cubic crystalline structure (see Chapter 4), assuming the conventional unit cell, $N^b_{Sn} = 1$, and from the XRD database $V^b_{Sn} = 242.69$ Å^3 [125].

Finally, using equation 6.4,

$$\rho_{Sn} = \frac{I^s_{Sn}}{I^b_{Sn}} = \frac{\rho^s_{Sn}}{\rho^b_{Sn}} = \frac{N^s_{Sn} V^b_{Sn}}{V^s_{Sn} N^b_{Sn}} = 4.2. \tag{6.15}$$

Notice that this value is in the same order of magnitude of the value that was extracted from the fitting $\rho_{Sn} = 2.71 \pm 0.33$. Both values are very close considering the number of assumptions that were made in both calculations.

In this section the light-induced degradation of $MASnI_3$ was studied. It was shown that upon illumination $MASnI_3$ decomposes into MAI and SnI_2. A model was presented that can estimate the degradation rate and the thickness of the SnI_2 layer at the surface of the sample.

Notice that this degradation mechanism is very similar to the one observed for light-induced degradation Pb-based perovskites [34, 35, 121, 126–128]. Nevertheless, the decomposition of Pb-based perovskites was shown to occur in two steps. In the second step, PbI_2 would degrade to metallic Pb. Therefore, it is of great interest to study the light-induced degradation of SnI_2. The next section focuses on the light-induced degradation of SnI_2 and places it in perspective with the PbI_2 degradation.

6.2 Comparison of Pb and Sn-based perovskite light induced degradation

In the previous section it was shown that $MASnI_3$ degrades into the organic component (MAI) and the metal halide component (SnI_2), similarly to Pb-based perovskites [34, 35, 121, 126–128]. However, PbI_2 has been reported to further degrade to Pb(0). Interestingly, during the 61 h of illumination, the $MASnI_3$ film formed minimal amount of Sn(0) and no Sn(4+) was detected. To study the degradation of SnI_2, a freshly deposited SnI_2 film was illuminated for approximately 100 h. This was compared with a similar experiment on PbI_2, performed by Dr. Jeremy Hieulle, where the lamp for degradation and the measurement equipment were the same as those used in this thesis.

The ratios $Sn(0)/Sn(tot)$ and $Pb(0)/Pb(tot)$ are shown in Figure 6.6 as a function of illumination time. Notice that the content in Pb(0) increased to more than 40% of the total amount of Pb in the probed volume of the sample, while the Sn(0) remained neglectable for the full duration of the experiment. Meaning that, in vacuum, SnI_2 did not degrade to metallic Sn after 100 h of illumination.

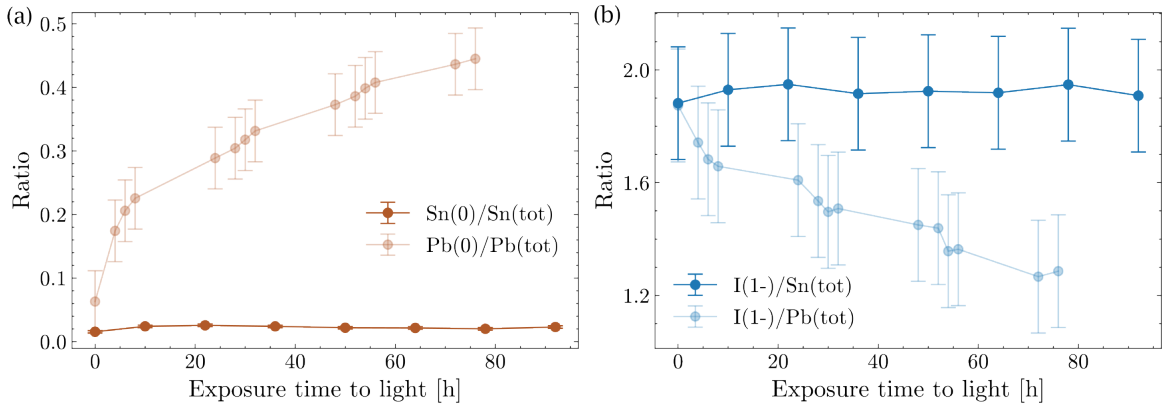

Figure 6.6: Comparison of light-induced degradation of SnI_2 and PbI_2 (a) formation of Sn(0) and Pb(0) (b) Changes in I(1-).

Similarly, for the iodide (Figure 6.6 (b)). Notice that both samples start with a similar iodide ratio, but in the case of SnI_2, the ratio remains constant, within the error bar for the

entire duration of the experiment, while for PbI_2 the ratio of I(1-)/Sn(tot) starts to decrease after only 4 h of exposure and continues to decrease for the duration of the experiment.

These results are surprising because, typically, the instability in Sn-based perovskites is attributed to the presence of Sn [62, 78, 79]. Nevertheless, here it was shown that SnI_2 is more stable than PbI_2 upon illumination in vacuum.

One point remains to be discussed. During light exposure of $MASnI_3$, a small quantity of Sn(0) was detected, but in this section, SnI_2 did not show any degradation to Sn(0). In the next section, the formation of Sn(0) in $MASnI_3$ is compared to the one in SnI_2, in order to understand what degraded into Sn(0).

6.3 Comparison of $MASnI_3$ and SnI_2 light induced degradation

Up to now, in this chapter, it has been shown that $MASnI_3$ degrades into SnI_2 upon illumination under UHV and that, in these conditions, SnI_2 is more stable than PbI_2. The question now is: Are the variations of Sn(0) in $MASnI_3$ and in SnI_2 comparable? More specifically, is $MASnI_3$ really forming Sn(0) as well?

Figure 6.7, shows the evolution of Sn(0) in SnI_2 and in $MASnI_3$ films after illumination. For SnI_2 the quantity of Sn(0) increases only during the first 10 h of exposure, and then remains constant. This quantity could either be a systematic fitting error or a small quantity of Sn(0) that is intrinsically present after synthesis. The last hypothesis would explain the increase in signal in the first 10 h, as this would be caused by the desorption of the contaminant layer as it was also observed in Figure 6.4.

On the other hand, for $MASnI_3$ the quantity of Sn(0) increases continuously. This indicates that indeed Sn(0) is formed in a small quantity when $MASnI_3$ is exposed to light and therefore the degradation mechanism is instead described by

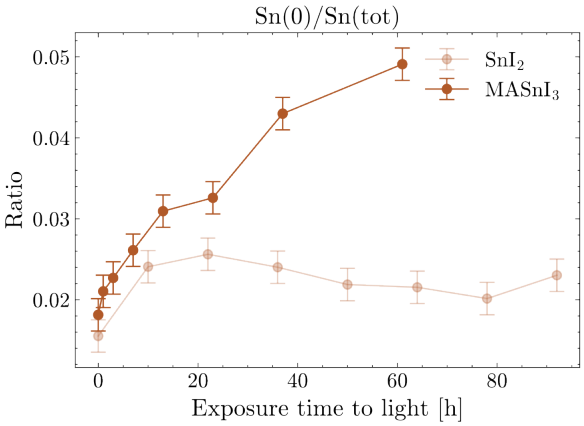

Figure 6.7: Evolution of Sn(0) in $MASnI_3$ and in SnI_2 with light exposure.

$$MASnI_3(s) \xrightarrow{h\nu} MAI(g) + A \cdot SnI_2(s) + (1 - A) \cdot [Sn(0)(s) + I_2(g)]. \tag{6.16}$$

where A is a probability factor between 0 and 1, which describes the probability that $MASnI_3$ decomposes in Sn(0) or in SnI_2.

In this section it was shown that Sn in $MASnI_3$ has a small probability of into Sn(0) when illuminated under vacuum. However, when $MASnI_3$ decomposes into SnI_2, it does not further reduce into metallic Sn.

6.4 Summary

In this chapter, light-induced degradation of $MASnI_3$ was studied using XPS and KPFM. It has been concluded that, upon illumination, SnI_2 and a small amount of metallic Sn are formed on the surface of the sample. More importantly, there was no formation of Sn(4+) during illumination in UHV. Furthermore, a bilayer model was derived as a function of time. This model was able to determine the thickness of the SnI_2 layer formed on the surface of the sample. In addition, light-induced degradation of SnI_2 and PbI_2 was also studied. SnI_2

showed no sign of light-induced degradation, while formation of Pb(0) was measured in PbI_2. This suggests that the light-induced degradation of $MASnI_3$ is not caused by the use of Sn or its tendency to oxidize. Instead, it was deduced that the light-induced degradation of $MASnI_3$ is caused by the MA^+ that has the tendency to break the bond it has in perovskite lattice and to leave the material. In order to improve the stability of Sn-based perovskites, it is important to use an organic cation that does not leave the sample.

Chapter 7

Water induced degradation of $MASnI_3$

In the previous chapter, it was shown that $MASnI_3$ forms SnI_2 when illuminated in UHV. However, light is only one of the many stresses that a solar cell can encounter in the field. In this chapter, another type of degradation is studied: water-induced degradation. More precisely, the degradation that $MASnI_3$ undergoes after exposure to liquid water or water vapor is studied.

The water-induced degradation of perovskites is still little understood, especially with regard to Sn-based perovskites. In this chapter, both water vapor and liquid water-induced degradation are studied. In the first part, Sn-perovskite films were degraded with a water layer and by being dipped in water and characterized using KPFM, XRD and XPS. Then, a detailed XPS analysis of the evolution of water vapor-induced degradation in $MASnI_3$ is studied as a function of time. With the exception of the sample that was dipped in water, all experiments and measurements were performed in a N_2 atmosphere or under vacuum, to avoid oxygen contamination of the samples from the air.

7.1 Liquid water induced degradation on $MASnI_3$ films

This section studies the degradation induced by liquid water in $MASnI_3$ samples. First, samples that were exposed to a thin layer of water, by spin coating with deionized (DI) water, were studied using AFM, KPFM and XPS. Then, a sample was dipped in DI water and measured in XRD.

Before exposing the sample to water, the freshly deposited $MASnI_3$ sample was measured in UHV using AFM and KPFM (Figures 7.1 (a) and (b)), and then transferred to the N_2 glovebox, where it was spin coated with 80 μl of DI water. Finally, the sample was transferred back to UHV, where it was again measured in KPFM (Figures 7.1 (c) and (d)). This sample was always transferred under high vacuum or in N_2 atmosphere. A reference sister sample was always present in the transfers of the water-exposed sample, which allowed the measurement of both samples in XPS; in this way, any effects due to transfer contamination would be visible in both samples and not taken into account in the interpretation.

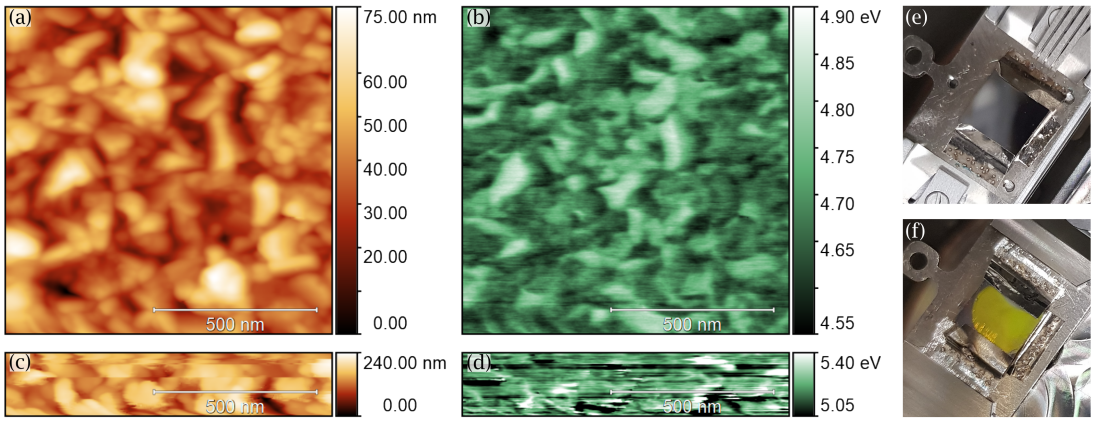

Figure 7.1: (a) Topography and (b) work function map of the pristine $MASnI_3$. (c) Topography and (d) work function map of the water-exposed sample. (e) Picture of pristine and (f) water-exposed samples on the UHV sample holder.

The topography of the pristine sample and its workfunction map are shown in Figures 7.1 (a) and (b). Similarly to the previous chapters (see Chapter 6), this sample showed the typical polycrystalline topography of halide perovskite, with grains of a few hundred

nanometers. Furthermore, the KPFM image (Figure 7.1 (b)) shows a facet-dependent work function, with an average value of 4.68 eV and a standard deviation of 0.05 eV, similar to the $MASnI_3$ samples studied in Chapter 6.

The measurements of the topography and the work function of the sample exposed to water (Figure 7.1 (c) and (d)) were unfortunately not stable enough to obtain a clean figure. Furthermore, the value of the work function is not considered trustworthy as the tip work function changed constantly during the measurement, due to material that got attached to the tip. Despite this, after exposure to water, the sample appears to be rougher with a maximum grain height of 240 nm instead of just 75 nm observed for the pristine sample (see Figures 7.1 (c) and (d), respectively).

Figures 7.1 (e) and (f) show a picture of the reference sister sample and a picture of the sample degraded by water. The sister sample shows the typical dark brown color of the $MASnI_3$ films [129], with a metallic sheen, a sign of good microscopic homogeneity. On the other hand, the sample exposed to water became yellow in the region touched by the water. This could be an indication that SnI_2 was formed, since SnI_2 is typically yellow. This aligns with the literature for Pb-based pervoskites, which have been shown to form PbI_2 upon water exposure [81, 87, 88]. Additionally, the sample does not exhibit the sheen that was visible for the pristine sample; this is probably due to the increased roughness of the sample, as observed in Figure 7.1 (b).

To confirm the presence of SnI_2 in the near-surface region, quantitative compositional measurements of the sample exposed to water and the reference sample were performed with XPS.

The Sn3d and I3d spectra are shown in Figure 7.2 (a) and (b), respectively. As expected for the reference sample (Figure 7.2 (a) (top)), the main component of Sn is Sn(2+). Sn(0) and Sn(4+) were also detected in small quantities, probably due to glovebox storage. Note that after exposure to water (Figure 7.2 (a) (bottom)), the main component remains Sn(2+), which is also expected when SnI_2 is formed.

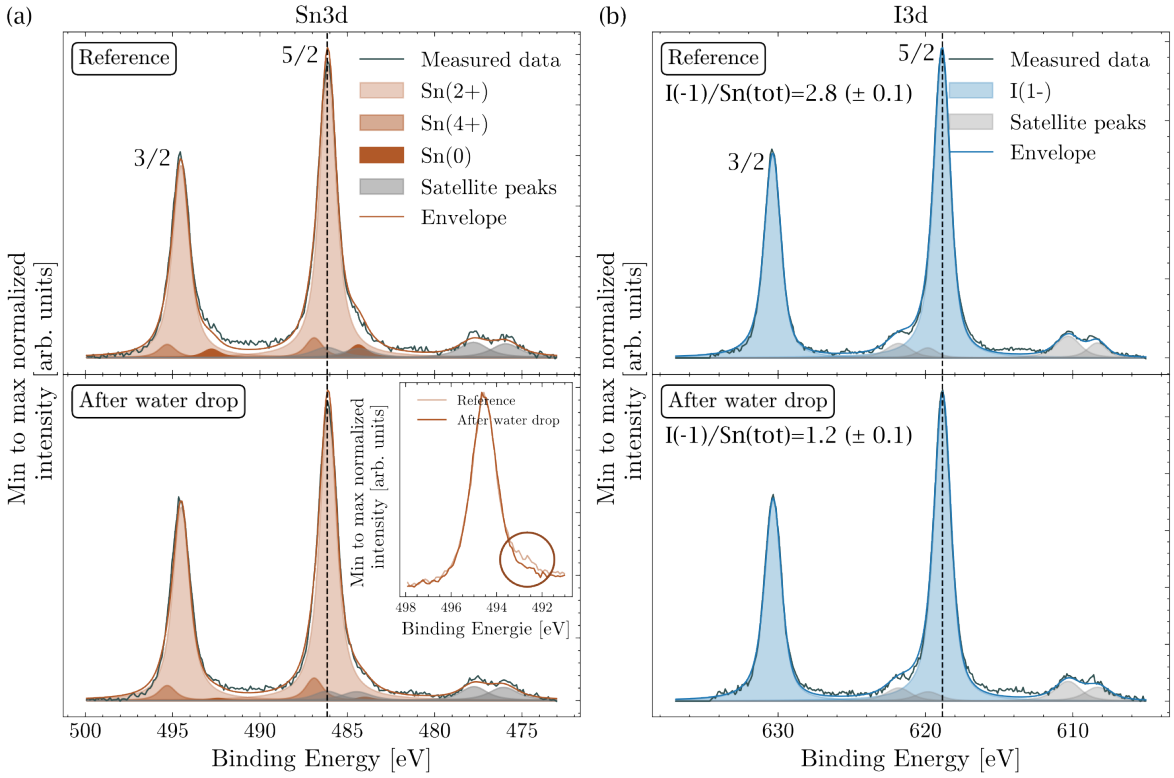

Figure 7.2: Detailed XPS spectra of the reference sample (top) and water drop degraded sample (bottom) in the (a) Sn3d and (b) I3d core level energies.

The content of Sn(4+) remained similar and varied only from 6% to 7%. This difference is within the error, suggesting that there is no oxidation of Sn(2+) to Sn(4+) with such a brief exposure to water. This is an unexpected result, as it shows a different behavior compared to the results reported in the literature [47].

Additionally, a small Sn(0) formation was observed for the sample that was exposed to the water drop. The inset in Figure 7.2 (a) shows the overlap of the Sn3d 3/2 spectra of the reference and water degraded samples, where it is clear that the reference sample has a larger shoulder on the lower energy side compared to the degraded sample. That is, the Sn(0) component decreased after exposure to water. This result can be caused by two mechanisms: 1. The metallic Sn, which is in the oxidation state Sn(0), bonded to water and was then washed away by the excess water during the spin coating; 2. The water oxidized Sn(0) into Sn(2+), forming SnO which would be an intermediate step to reach the more

thermodynamically favorable SnO_2 [130, 131]. X-ray diffraction (XRD) measurements of the degraded sample did not show the presence of SnO (see Figure A2), and therefore it is not possible to distinguish between the two cases. In fact, XRD only detects crystalline phases, but SnO could be amorphous. However, SnO formation upon exposure to water has previously been observed by Wang et al., with Fourier transform infrared (FTIR) spectroscopy measurements [47]. Furthermore, the formation of SnO_2 at this stage is excluded, because in SnO_2, tin is in the Sn(4+) oxidation state, which, as already mentioned, does not show a significant change in the ratio.

The binding energy of the iodine remained the same after exposure to water (Figure 7.2). However, the I/Sn(tot) ratio decreased from 2.8 to 1.2, which is considerably lower than the expected value for SnI_2, i.e. I/Sn=2. Such a low ratio can be justified by the presence of oxygen and eventually the formation of SnO and by the iodine which left the surface. Further investigation is possible by looking in more detail at the XPS spectra of O, C and N in Figure 7.3.

In general, oxygen is present in small amounts (close to the noise level) in the reference samples (Figure 7.3 (a)). This is possibly due to glovebox storage, as discussed in Chapter 4. In Figure 7.3 (a) (top), it is visible that although the oxygen peak has a low intensity compared to the noise level of the measurement, the peak is broad and the fitting must contain at least three peaks, corresponding to three oxygen components. Since the nature of these components is unclear, they were named according to their binding energy, which means that O_{low} is the peak with the lowest energy, O_{high} the peak with the highest energy and O_{middle} the peak in between. The FWHM of the peaks was estimated using the sample that was degraded by the water drop (7.3 (a) (bottom)). After water exposure, the O_{low} peak increased significantly, compared to O_{middle} and O_{high}, which helped to deconvolute it from the other two peaks.

Upon close inspection of the O_{low} peak in the reference sample and in the water-degraded sample, it is possible to see that both peaks are slightly shifted compared to each other. In fact, the O_{low} binding energy changes from 530.44 eV, in the reference sample, to 529.91 eV,

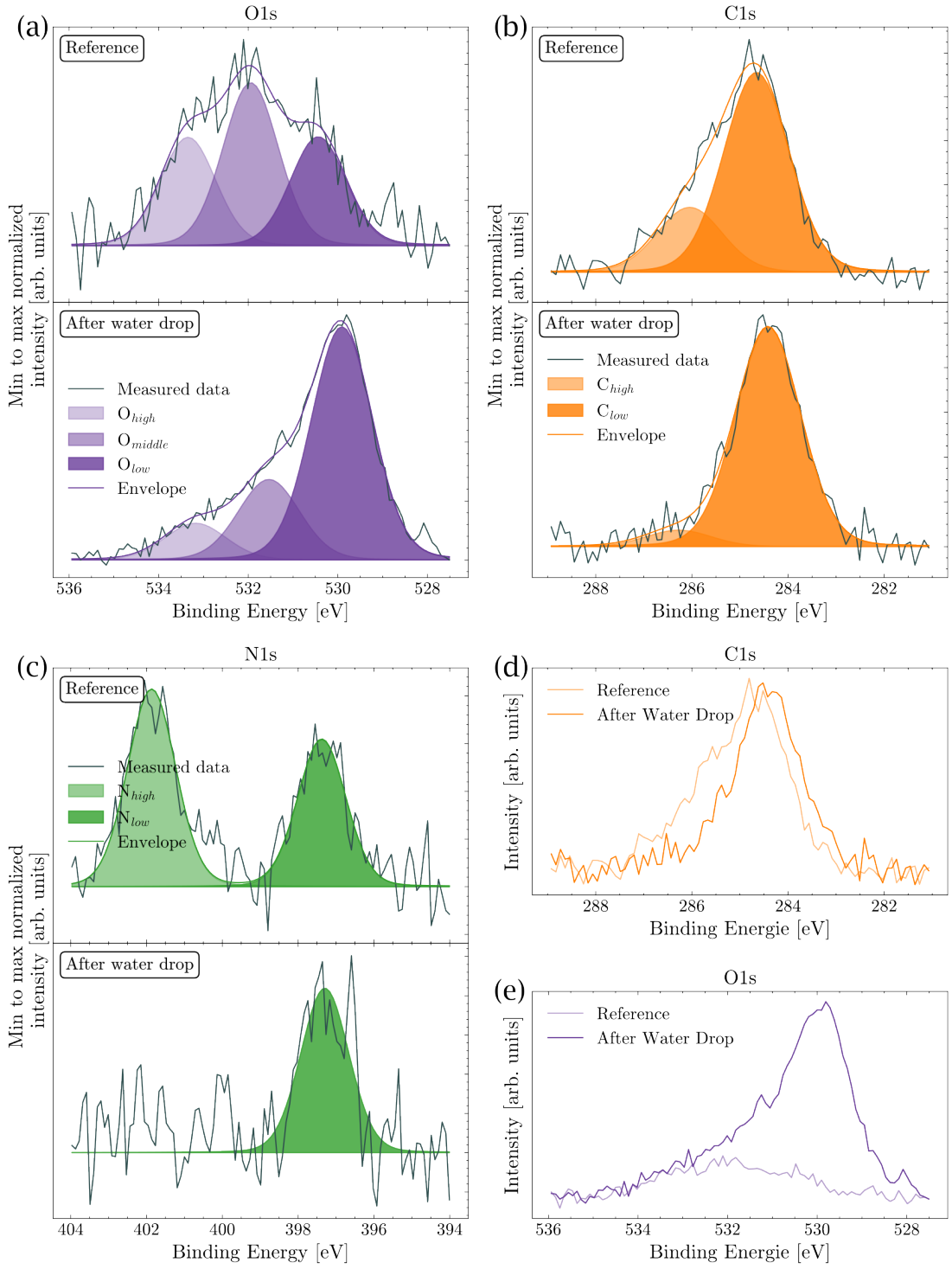

Figure 7.3: Detailed spectra of the reference sample (top) and water exposed sample (bottom) in the (a) O1s, (b) C1s and (c) N1s core energy levels. Overlap of the pristine and exposed sample on the (d) C1s and (e) O1s core energy levels.

in the degraded sample, which is a difference of only 0.53 eV. This difference is probably due to the fitting error caused by the high-level noise in the reference sample spectrum.

To explain the increase in O_{low}, one could hypothesize that O bonded to Sn, forming SnO, and allowing Sn to remain in the (2+) oxidation state. The consequence is that, in the spectrum of Sn3d in Figure 7.2 (a), the component Sn(2+) had two indistinguishable contributions: (1) the first contribution from the Sn bond with O, to form SnO and (2) the second contribution from the Sn that bonded to I (either forming SnI_2 or $MASnI_3$). As a consequence, the additional Sn(2+) contribution led to a ratio I/Sn that was considerably lower, as observed in Figure 7.2 (b). The corrected intensity of Sn(2+), is given by,

$$I_{Sn(2+)} = I_{Sn_O(2+)} + I_{Sn_I(2+)} \tag{7.1}$$

Where $I_{Sn(2+)}$ is the corrected intensity of Sn(2+), $I_{Sn_O(2+)}$ is the contribution of Sn that bonded to oxygen and $I_{Sn_I(2+)}$ is the contribution of Sn that bonded to iodide.

To verify this hypothesis, it is necessary to calculate the ratio I/Sn(2+), after subtracting the contribution $I_{Sn_O(2+)}$ from $I_{Sn(2+)}$. Assuming that all O_{low} bonded to Sn(2+) and because SnO has a ratio of Sn to O of $1:1$, then the corrected peak intensity of O_{low} ($I_{O_{low}}$) should be the same as $I_{Sn_O(2+)}$. That is

$$I_{O_{low}} = I_{Sn_O(2+)} \tag{7.2}$$

Using the definition equations 7.1 and 7.2. One can calculate the ratio of the I with the Sn taking into account only the contribution of Sn that is connected to I. This is,

$$\frac{I_I}{I_{Sn(2+)} - I_{Sn_O(2+)}} = \frac{I_I}{I_{Sn(2+)} - I_{O_{low}}} = 1.9 \tag{7.3}$$

where I_I is the corrected intensity of I. Note that the obtained ratio is 1.9, which, within the error bar, is the expected I/Sn ratio for SnI_2. Suggesting that no $MASnI_3$ was detected and the degradation of $MASnI_3$ with the water drop formed SnI_2. This confirms what was observed in Figure 7.1 (f).

To double check this result, the same reasoning can be applied for the O_{low}/Sn(2+) ratio. Knowing, from equation 7.3, that degradation with the water drop formed SnI_2, where an Sn atom is bonded to two I atoms, the corrected intensity of the iodide I_I is expected to be twice the intensity $I_{Sn_I(2+)}$, which can be written as

$$I_I = 2 \cdot I_{Sn_I(2+)} \tag{7.4}$$

Using the definition equations 7.1 and 7.4, it is possible to calculate the ratio of O_{low} to Sn, taking into account only the contribution of Sn that is connected to O, so

$$\frac{I_{O_{low}}}{I_{Sn(2+)} - I_{Sn_I(2+)}} = \frac{I_{O_{low}}}{I_{Sn(2+)} - I_I/2} = 0.8 \tag{7.5}$$

This ratio is very close to the expected ratio for SnO, which means O/Sn = 1. This confirms the initial assumption that O belonging to the O_{low} component forms SnO.

Looking at components C1s and N1s (Figure 7.3 (b) and (c) respectively), the components C_{high} and N_{high}, which were attributed to the presence of perovskite (see Chapter 3), vanish after the exposure to the water drop. Leaving only C_{low} and N_{low} that are contami-

nation from transfers and glovebox. This corroborates with the observation that no $MASnI_3$ is being measured, only SnI_2 and a small fraction of SnO.

Figures 7.3 (d) and (e) show the overlap of the pristine and water-exposed samples in the C1s and N1s core energy levels, respectively. For C1s, it is clear that the higher energy contribution is no longer present after the sample is exposed to water. In contrast, for oxygen, it is clear that the lower binding energy peak increased, while the other peaks remained approximately the same, confirming the observations made in Figure 7.3 (a).

XRD was used to measure the crystalline structure and confirm whether $MASnI_3$ forms SnI_2 when exposed to liquid water (SnO is usually amorphous and not visible in XRD). Because XRD is a bulk measurement technique, instead of using the water drop that was spin coated on the sample, the latter was dipped in a beaker containing DI water (see Figure 7.4 (a)-(f)). After degradation, the sample was dried in two steps, first with pressurized N_2 and then vacuum-dried in the glovebox antechamber. Both processes were done as fast as possible to minimize air exposure.

The advantage of this technique is that the change in color can be easily observed and the exposure time can be controlled with greater precision. However, this exposure had to be done in an ambient atmosphere due to the large amount of water required. This means that the technique is not adequate for surface-sensitive measurements like XPS or KPFM as the surface would get contaminated by the atmosphere, but it is acceptable for bulk measurements such as XRD.

The image sequence of the sample dipped in water (Figure 7.4 (a)-(f)) initially shows a dark brown sample (Figure 7.4 (a)), which instantly transformed into a brighter color when dipped in water (Figure 7.4 (b)). The color then became brighter and more yellow with time (Figure 7.4 (c)-(e)), until t=23 s where the sample was fully yellow (Figure 7.4 (f)).

The water dipped sample and a pristine sister sample were measured in XRD. Similarly, to what was seen in chapter 6, the pristine sample shows a cubic $MASnI_3$ crystalline structure

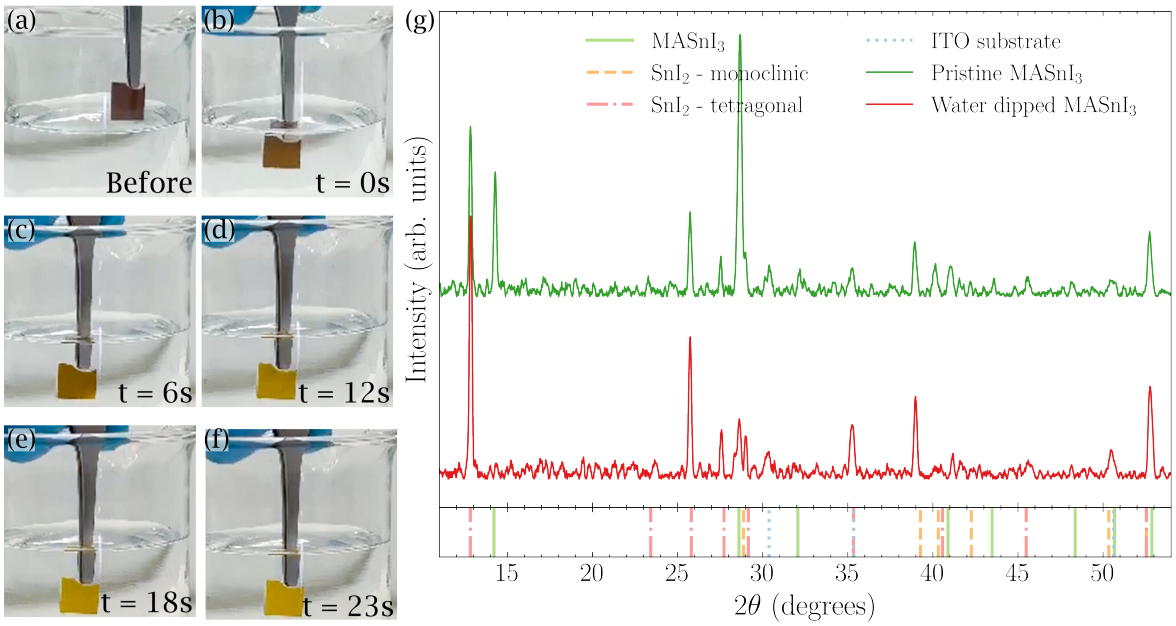

Figure 7.4: (a)-(f) Image sequence of $MASnI_3$ degradation while dipping the sample in DI water. These pictures were color edited such the white background would visually match for every picture. (g) XRD of a pristine $MASnI_3$ samples, the water degraded sample and of an SnI_2 film (PDF-00-064-0961, PDF-00-025-0975, 00-056-0088, [115]).

with predominant peaks at 2θ=14.3° and 2θ=28.7° and a SnI_2 secondary phase, mainly in at 2θ=12.8° and 2θ=25.7°. After exposure to water, all of the $MASnI_3$ related peaks vanished, except for the main peak in 2θ=28.7°, for which the intensity was strongly reduced. In contrast, the SnI_2 peaks increased, showing that SnI_2 formed during water-induced degradation.

In summary, this section shows that when exposed to water, the $MASnI_3$ film rapidly decomposes into SnI_2. In addition to SnI_2, the formation of SnO was also detected. The formation of these two decomposition products explains the significant loss in iodine content. Contrary to what was reported in literature [63, 92], no formation of Sn(4+) was measured, meaning that SnI_4, nor SnO_2 were detected. However, the question remains whether the degradation induced by liquid water is the same as the degradation induced by water vapor. Furthermore, in real-life applications and during large-scale production, the perovskites are more likely to be exposed to water vapor than to liquid water. Therefore, the degradation of $MASnI_3$ induced by water vapor is studied in the next section.

7.2 Degradation of $MASnI_3$ films induced by water vapor

Similarly to the experiments reported on $MAPbI_3$ [81, 85], water vapor-induced degradation is expected to also form SnI_2. However, this process should occur slower than that in the previous section, with liquid water, because the number of water molecules available for the reaction is lower. Therefore, this section focuses on the XPS measurements of a sample that was repeatedly exposed to water vapor for different intervals of time. The water vapor exposures were performed in a gas dosing system (more details are given in Chapter 3), which allowed to expose the sample to water without air exposure. The $MASnI_3$ sample was exposed to 20 mbar of water vapor during different intervals of time and measured in XPS between each interval. The total exposure time summed up to 16.5 h.

The 16.5 h water vapor degraded sample is shown in Figure 7.5 (a), where it was placed to the right of a pristine $MASnI_3$ sample. In the figure, it is visible that the degraded sample became yellow with transparent dots. The yellow phase could either be SnI_4 or SnI_2, whereas the transparent part could be SnO, SnO_2 or simply holes in the film. In order to understand what is the composition of the different phases, detailed XPS measurements are necessary. In Figure 7.5 (b), a mask was applied on the transparent spots of the sample. The area covered by the mask accounts for 16 % of the surface that is inside the black rectangle. Therefore, it is expected that the secondary phase that formed these shapes is also approximately 16 % of the composition of the sample.

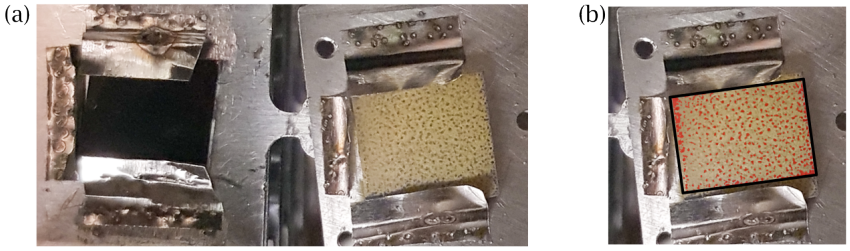

Figure 7.5: (a) Picture of a pristine $MASnI_3$ sample (left) next to the sample that was degraded with water vapor for 16.5 h (right), (b) degraded sample with mask.

Detailed scans of the orbital binding energies of Sn3d after 90 minutes and after 16.5 h exposure to water vapor are shown in Figure 7.8 (a) top and bottom, respectively. The choice of the 90 minutes curve as reference instead of the pristine one will be explained later in this section. The sample that was exposed to water vapor for 90 minutes shows no obvious signs of degradation, which means that the majority of the signal in the Sn3d orbital originates from the Sn(2+) oxidation state and only a small amount of Sn(4+) and Sn(0) was detected.

After 16.5 h of exposure, the main component remains Sn(2+), which corresponds to the oxidation state of Sn in $MASnI_3$ and also in SnI_2. Furthermore, no formation of Sn(0) was detected (Figure 7.6 (a) bottom). However, formation of Sn(+4) is visible (in Figures 7.6 (a) and (b)), reaching approximately 18% of the total amount of Sn. This was unexpected since no Sn(4+) formation was detected in the previous section, when the sample was exposed to liquid water. The oxidation state of Sn(4+) could be an indication of SnO_2 or SnI_4. Additionally, the presence of Sn(4+) in Sn-perovskite has also been associated with water degradation in the literature and was attributed to the formation of MA_2SnI_6 [47].

From the calculated I(-1)/Sn(tot) ratios, we can see that the amount of iodine on the surface of the sample tends to decrease. That is, it initially goes from 3.4 to 2.4 (the initial ratio is greater than 3 due to PEAI contamination, as explained in Chapter 6). The fact that the ratio I(-1)/Sn(tot) decreases, means that very probably the sample is not forming SnI_4 nor MA_2SnI_6, where the expected ratios would be 4 and 6 respectively.

When looking at the I3d peak shape, similarly to Sn3d, the I3d orbital does not show obvious signs of degradation (Figure 7.6 (c)) after 90 minutes exposure to water vapor, meaning that the iodine spectrum shows the same usual FWHM that is measured in pristine samples and the binding energy also matches the measured binding energy. However, after 16.5 h, the FWHM of the I3d orbital increased, suggesting a different environment for part of the iodine or even the formation of an additional iodine component. This is a surprising result because this is the first time a FWHM increase was observed in this work, and to the best of current knowledge, the literature contains no reports of XPS measurements showing an

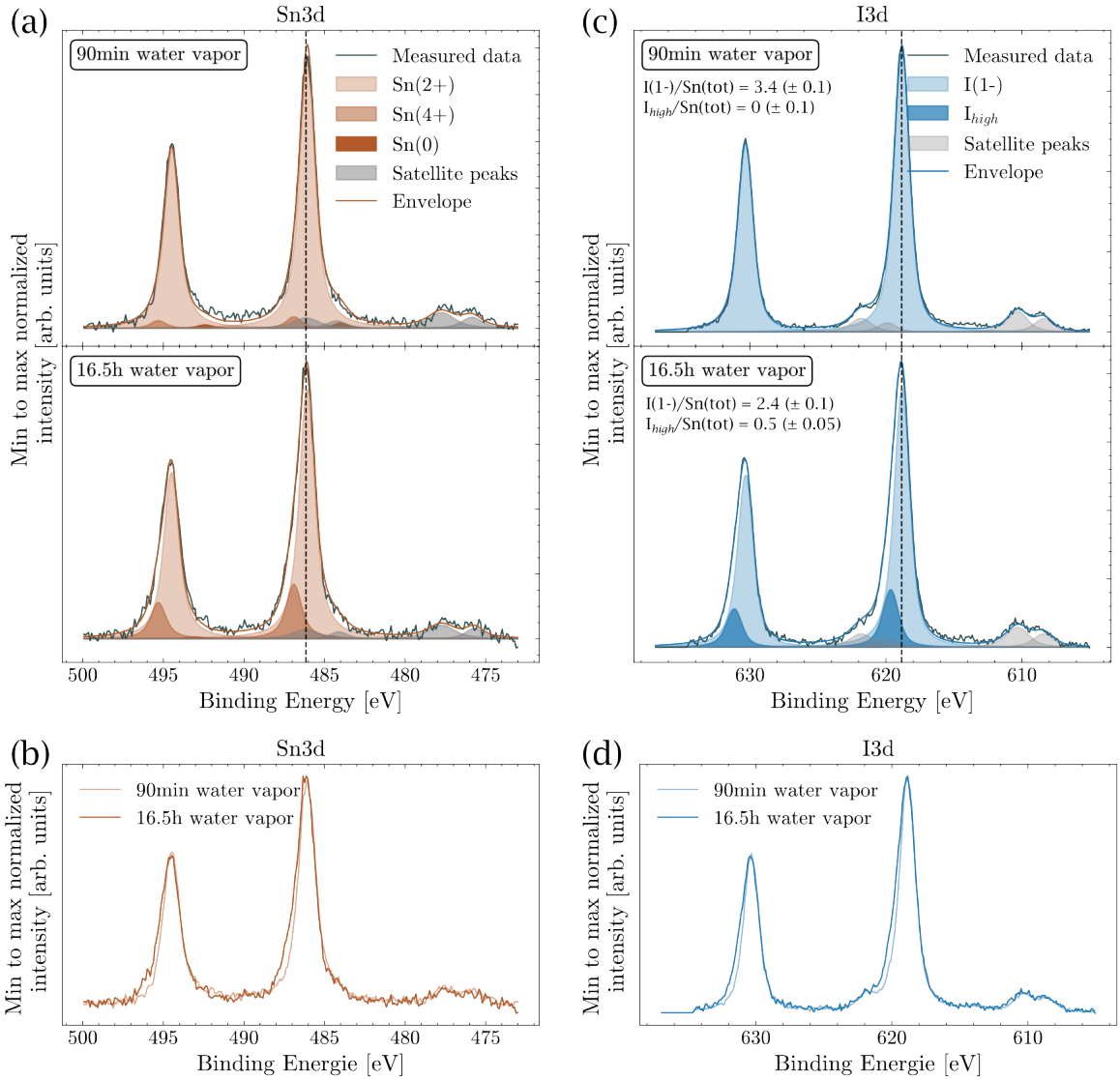

Figure 7.6: XPS measurement of $MASnI_3$ sample exposed to water vapor for 90 minutes and 16.5 h. Detailed scans in the Sn3d orbital (a) with components fitted (b) background subtracted raw data overlapped. Detailed scans in the I3d orbital (c) with components fitted (d) background subtracted raw data overlapped.

additional iodine component upon perovskite degradation. The difference in FWHM is easier to visualize when overlapping the minimum to maximum normalised detailed spectra after 90 minutes and after 16.5 h exposure to water vapor, as shown in Figure 7.6 (d) for orbital I3d.

Oxygen is the element that showed the most remarkable changes after exposure to water vapor. Although after 90 minutes of exposure to water vapor, the amount of oxygen is almost negligible (Figures 7.7 (a) and (b)), after 16.5 h the amount of oxygen increased significantly. As seen in the previous section, the O1s peak can be fit with three different components, namely O_{low}, O_{middle} and O_{high}. The greatest increase was observed for the O_{low} component, followed by O_{middle} and then O_{high}, which only increased slightly.

The C1s and N1s components are prone to be affected by sample transfers. Due to the amount of transfers in this section (16 in total), the values for these components are not reliable and are therefore not taken into account.

To understand what species are formed during exposure to water vapor, it is essential to study the evolution of the ratio of the different elements and components. The evolution of the I/Sn(tot) ratio as a function of the exposure time to water vapor is shown in Figure 7.8 (a). Here, we see that degradation appears to be separated in two stages. First, the iodine content increases during the first 90 minutes (shaded in gray), beyond which the iodine content started to decrease. In the second stage of degradation, a new I component (I_{high}) begins to form and its signal increases with the exposure time up to a ratio I_{high}/Sn(tot)=0.5. In contrast, the typical iodine component denoted I(1-) (usually associated with the presence of $MASnI_3$ and SnI_2) decreased to 2.4, which is close to the ratio of SnI_2. Furthermore, the sum of both iodine components (denoted I(tot)) decreased with exposure time, probably due to the iodine leaving the sample similarly to what was observed in the light degradation studies (Chapter 6). It is worth mentioning here that no collective shift was observed in the other elements (i.e. C1s and N1s), therefore the component I_{high} appears to be indeed an additional component and not the effect of charging or of a different workfunction.

Note that the two degradation stages are present in all three evolution ratio plots (Figures 7.8 (e)-(g)). In fact, the first phase is similar to what was observed in the Chapter 5, meaning that the changes in the ratios do not appear to be triggered by degradation, but rather by the desorption of a contaminant layer. This phenomenon could be due to the UHV environment,

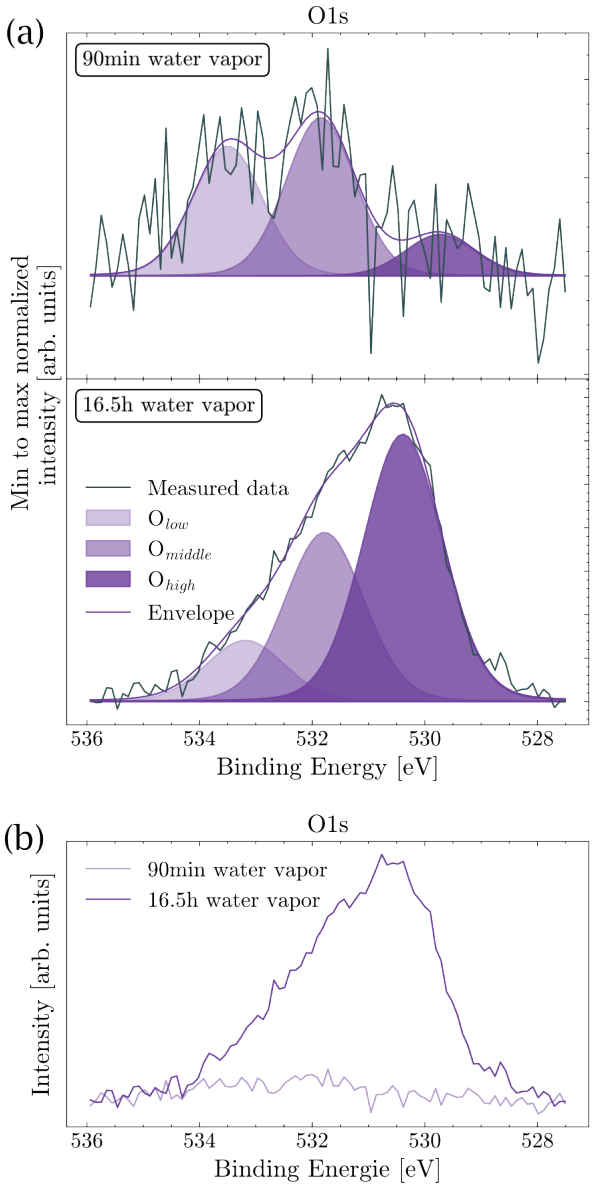

Figure 7.7: XPS measurement of $MASnI_3$ sample exposed to water vapor for 90 minutes and 16.5 h. Detailed scans in the O1s orbital (a) with components fitted (b) background subtracted raw data overlapped.

that the sample is in during the measurement. If this is the case, these results imply that $MASnI_3$ can be exposed to environments saturated with water vapor (here 20 mbar) for 90 minutes without changing its composition significantly. The fact that the contamination layer seems to desorb during the first 90 min and the fact that the sample does not seem to

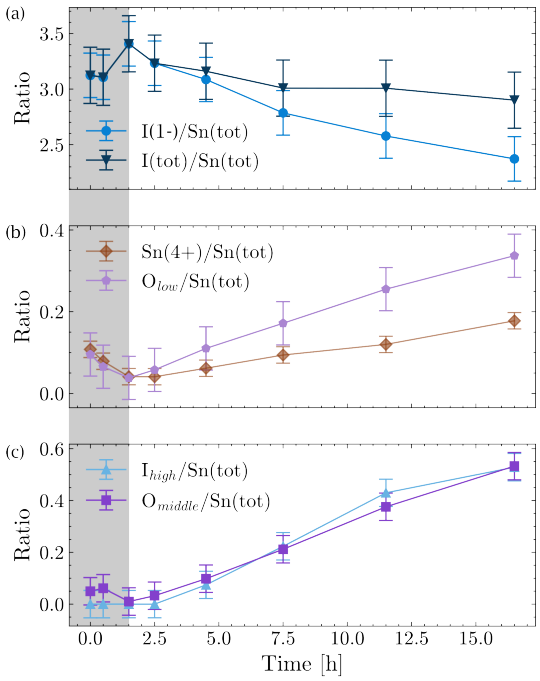

Time [h]	O_{low}/Sn(4+)
0	0.9
0.5	0.8
1.5	0.9
2.5	1.4
4.5	1.8
7.5	1.8
11.5	2.1
16.5	1.9

Figure 7.8: XPS measurement of water vapor degradation series of a $MASnI_3$ sample. (a) Evolution of the iodine component I(1-) and of I(tot).(b) Evolution of Sn(4+) and O_{low}. (c) Evolution of I_{high} and O_{middle}.

degradate during that period of time are the reason why it is more logical to plot the sample after 90 minutes: first, the sample seems cleaner when looking at the ratios, and second, the FWHM of the 90 min sample is smaller than for the pristine sample. The latter, also makes it easier to compare with the 16.5 h degraded sample and to visualize in the figures.

Focusing on Sn(4+) (Figure 7.8 (b)), the Sn(4+)/Sn(tot) ratio decreased during the first 90 minutes of exposure to water vapor, but after 16.5 h the ratio increased to 18 % of the total amount of Sn. It should be noted that for exposures greater than 90 min, the O_{low} component increased approximately twice as fast as Sn(4+). The ratio of O_{low}/Sn(4+) became 1.8 after 4.5 h of water vapor degradation and remained close to 2 for the rest of the experiment (see Figure 7.8 (b) (table)). This suggests the formation of SnO_2 after long exposure times. The fact that Sn(4+) was formed here, after a long exposure time and not with the fast degradation observed with liquid water (Section 7.1) suggests that degradation products containing Sn(4+), in this case SnO_2, need more time to form than products with

the oxidation state Sn(2+), such as SnO. In addition, one could speculate that the SnO observed in Section 7.1 is the product of the unfinished reaction that would have formed SnO_2. Abbasli et al. also observed three oxygen peaks upon perovskite degradation and assigned the lowest binding energy peak to SnO_2 [21].

Note that, in Figure 7.5 (b), it was discussed that the transparent spots accounted for approximatly 16 % of the surface of the sample. Here, it was shown that the Sn(4+) represented 18 % of the total Sn after degradation. These values are very close to each other, suggesting that the transparent spots that were visible in the picture were, in fact, SnO_2.

It is not clear whether there are multiple steps to degradation. For example, $MASnI_3$ could decompose into SnI_2, which decomposes into SnO and further degrades into SnO_2. Or, instead, degradation into SnI_2 and SnO_2 could occur simultaneously. However, up to now it was clear that $MASnI_3$ decomposes into SnI_2 and SnO_2.

The evolution of the second iodine component is monitored through the I_{high}/Sn(tot) ratio in Figure 7.8 (c). This component remains constant, close to 0, for the first 90 minutes of exposure, but continuously increases for larger exposure times. Surprisingly, an similar increase is observed for the evolution of the ratio O_{middle}/Sn(tot). This correlation could be caused by multiple phenomena, such as (i) the interaction of I, from the perovskite, and O from the water molecules that would cause a different chemical environment for I, which would translate into a binding energy peak shift, or (ii) the replacement of I by O in the $MASnI_3$ lattice upon the formation of I_2, or even (iii) the presence of iodine oxide (IO) gas that would be trapped in the $MASnI_3$ crystal [132]. However, this phenomenon has never been previously reported, and complementary measurements would be necessary to shed more light on this second iodine component.

7.3 Summary

In conclusion, in this chapter it was shown that liquid water and water vapor degrade $MASnI_3$ differently. When exposed to liquid water, the perovskite degrades in seconds, forming an SnI_2 film on the substrate. The degradation with water vapor occurs significantly slower, and the SnI_2 (for which the I/Sn ratio is 2) takes longer than 16.5 h of exposure to be reached. During this process, there was also the formation of SnO_2, which was not observed when the sample was exposed to liquid water. From this set of measurements, it is clear that water represents an important threat to $MASnI_3$.

Chapter 8

Synthetic air induced degradation of $MASnI_3$

In the previous chapter, the mechanism of degradation of $MASnI_3$ induced by the interaction with water was studied. However, water vapor is only present in a small fraction in air. Another stress that is usually associated with the degradation of $MASnI_3$ is O_2, which represents approximately 20 % of the air composition. Therefore, here the aim is to isolate the degradation induced by O_2, to do so, synthetic air, which does not contain water, is used. This chapter is divided into two main sections. First, a $MASnI_3$ sample is studied after being exposed to synthetic air (with a purity of 99.999 %). In the second part, the effects of synthetic air are compared to those of water vapor investigated in Chapter 7.

8.1 Synthetic air induced degradation of $MASnI_3$

In order to study the O_2-induced degradation in $MASnI_3$, a freshly deposited sample was exposed to approximately 1000 mbar of synthetic air for different intervals of time. Synthetic air consists in 20.5 Vol.% O_2 and 79.5 Vol.% N_2, with purity of 99.999 %. As N_2 is expected to

be inert, this equates to investigating the degradation of $MASnI_3$ induced by oxygen. After each exposure interval, the sample was moved in a vacuum suitcase to the XPS chamber, where composition measurements were performed.

Figure 8.1 shows a sequence of pictures taken after the sample was exposed to synthetic air for different intervals of time. For the first hour of exposure, the film remained dark and did not show much difference in appearance. Nevertheless, after 3 h of exposure, the sample became dark brown (instead of almost black), which means that it was becoming transparent and the sample holder was reflecting back light through the sample. After 5 h of exposure to synthetic air, the sample became light brown and finally, after 12 h it became almost fully transparent. Note that the sample exposed for 12 h was a sister sample and this explains the different sample holders visible in the pictures. Unlike the samples exposed to water (see Chapter 7), these did not become yellow but transparent. This is an indication that the O_2-induced degradation forms SnO_2, which is transparent, instead of SnI_2 or SnI_4, which would be yellow.

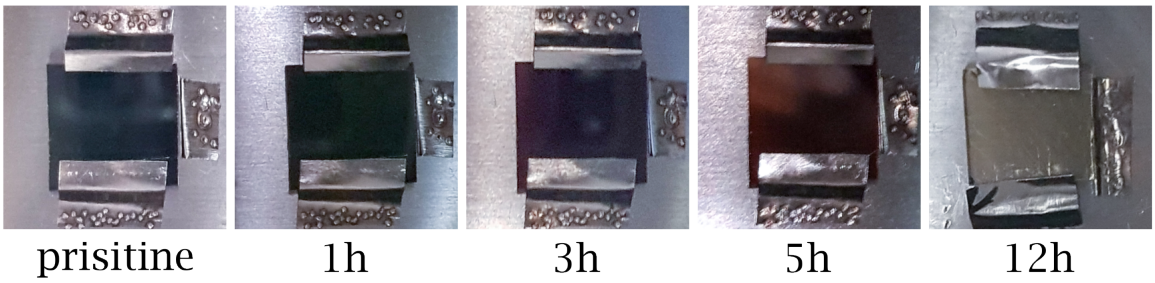

Figure 8.1: Picture sequence of $MASnI_3$ after different intervals of exposure to synthetic air. The pictures were color adjust so that the sample holders would have a similar color.

In the previous chapter, XPS measurements were used to confirm the presence of SnI_2 and other degradation products in the sample. There, the ratio $I/Sn(tot)$ played a critical role in proving the formation of SnI_2. Furthermore, a second peak of iodine was found at higher binding energies and was denoted I_{high}. This chapter takes a similar approach, in the sense that quantitative XPS measurements were performed on the sample after each exposure interval. The C and N contributions are not discussed in this chapter because they

are prone to have been affected by the multiple sample transfers that were performed during this experiment.

Thus, in this case, iodine is of particular interest. In fact, if the film formed SnO_2 instead of SnI_2, more iodine in the form of I_2 should have left the sample. As a consequence, the ratio I(1-)/Sn(tot) is expected to reach a value lower than 2. Here, the evolution of iodine is discussed first, and the variation in tin is discussed later. A summary of the evolution of both iodide components in the sample upon exposure to synthetic air is shown in Figure 8.2. Notice that in total the sample was exposed to synthetic air for 5 h. This was because charging was observed for longer exposure times (see Chapter 3), which significantly complexifies the analysis. In fact, the charging in the sample could be another indication of the presence of SnO_2 in the sample, as this phase has a quite high bandgap (around 3.6 eV) [133].

As expected, from Chapter 4, the I3d spectrum of the pristine sample shows a single peak for each of the spin orbit coupling peaks (see Figure 8.2 (a) (top)), as was also observed in Chapter 3. Furthermore, the 5/2 peak has a $E_{binding} = 618.8\,\text{eV}$ which aligns with the expected value for this peak, as discussed in Chapter 3. After 5 h exposure to synthetic air, part of the iodide in the oxidation state (1-) was converted to a higher binding energy, here denoted I_{high}. This is represented by the darker blue peak visible in Figure 8.2 (a) at the bottom. The impact of this additional contribution I_{high} in the peak shape can be seen in Figure 8.2 (b), where the I3d spectra of the pristine sample and of the 5 h air exposed sample were plotted. Here, the FWHM of the iodide peak clearly increased after 5 h of exposure, suggesting that the iodine formed a different compound or is in a different environment. The additional iodine component I_{high} was also observed in the previous chapter (see Chapter 7), when the $MASnI_3$ sample was exposed to water vapor. The I_{high} peaks, from both degradation processes, are compared in Section 8.2.

The evolution of the iodide ratios I(1-)/Sn(tot) and $I_{high}/Sn(tot)$ as a function of the exposure time to synthetic air are shown in Figure 8.2 (c). The ratio of the total amount of iodide $I(tot)/Sn(tot)$ decreased from 3.6 to 1.7. This led to two observations: First, the

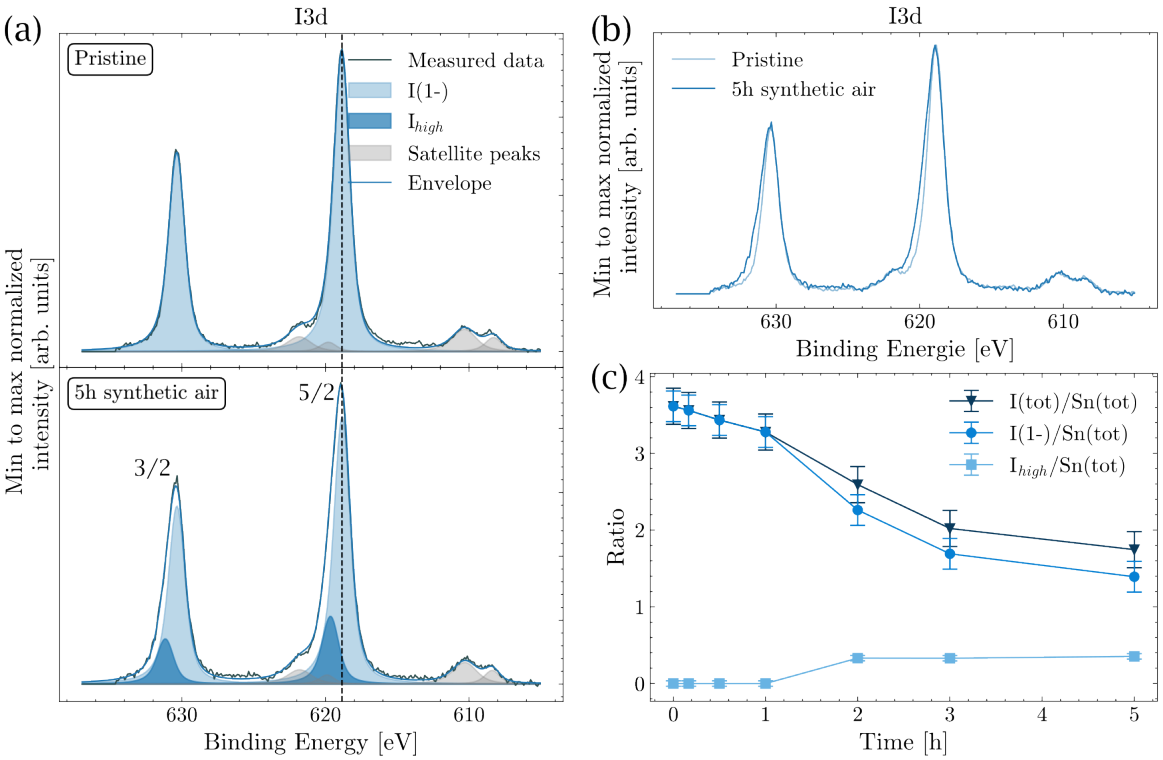

Figure 8.2: Evolution of iodide in $MASnI_3$ as a function of exposure time to synthetic air. (a) I3d peaks of the pristine sample (top) and the sample exposed to synthetic air for 5 h (bottom), fitted with corresponding peak model. (b) Minimum to maximum normalized I3d peaks of both samples overlapped. (c) Evolution of the ratio I/Sn as a function of the exposure time.

initial ratio was larger than the stoichiometric ratio $I/Sn = 3$ expected for $MASnI_3$, because this sample suffered from cross-contamination with PEAI (see Chapter 4). Second, the ratio of 1.7 was lower than the ratio $I/Sn = 2$, which is lower than the stoichiometric ratio of SnI_2, i.e. $I/Sn = 2$. Notice that, in the SnI_2 phase the iodine is in the oxidation state (-1), which also corresponds to the oxidation state of $MASnI_3$ (see Chapter 3). Therefore, one should only consider this component for the ratio, that is $I(-1)/Sn(tot)$, doing so leads to an even lower value, as $I(-1)/Sn(tot) = 1.4$. This argument suggests that the end product of this degradation is not SnI_2 and therefore Sn must bond with other elements. This is supported by the transparent color of the sample, discussed in Figure 8.1, as SnI_2 should have a yellow appearance. Furthermore, the XRD measurement on the sample (see Figure A3) does not show the presence of any additional crystalline phase.

Having excluded the formation of SnI_2, it is hypothesized that the measured iodide, in the oxidation state (-1), is part of the remaining $MASnI_3$. Note that the evolution of the sample's appearance (in Figure 8.1) to light brown is consistent with the presence of $MASnI_3$ in the film. To check if this hypothesis is reasonable, one needs to first look at the Sn ratios, shown in Figure 8.3 (c), and compare them to those of I.

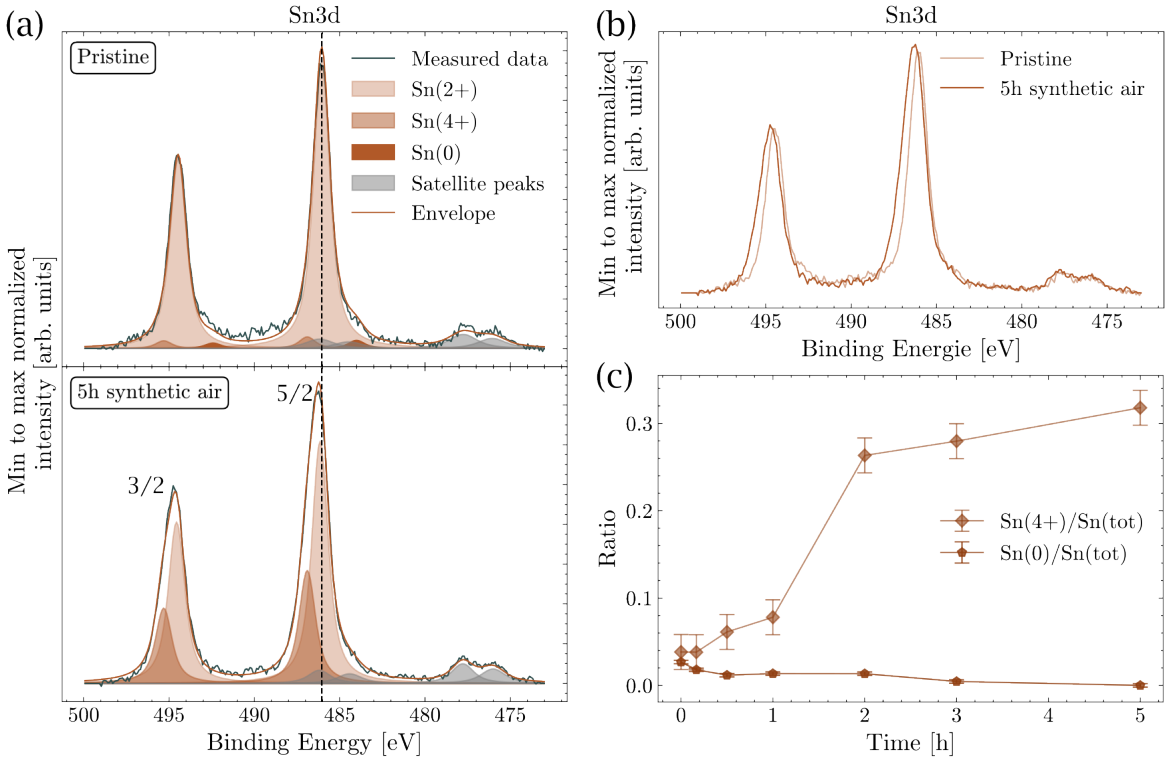

Figure 8.3: Evolution of tin in $MASnI_3$ as a function of exposure time to synthetic air. (a) Sn3d peaks of the pristine sample (top) and the sample exposed to 5 h synthetic air (bottom), fitted with the corresponding peak model. (b) Minimum to maximum normalized Sn3d peaks of both samples overlapped. (c) Evolution of the Sn(0)/Sn(tot) and Sn(4+)/Sn(tot) as a function of the exposure time.

Focusing on the pristine $MASnI_3$ spectrum, in the Sn3d energy region, the sample mostly contained Sn(2+) and only small quantities of Sn(0) and Sn(4+), probably due to contamination in the glovebox (see Figure 8.3 (a) (top)). Upon exposure to synthetic air, part of the Sn(2+) oxidized to Sn(4+), which is visible from the fitting in Figure 8.3 (a) (bottom) and also from the increase in the FWHM of the exposed sample towards higher binding energies,

in Figure 8.3 (b). Note that there was no Sn(0) formation, quite the opposite: the small amount of Sn(0) present in the pristine sample (represented by dark brown peaks) vanished after 5 h of exposure to synthetic air. This probably happened because the Sn(0) oxidized into Sn(2+) or Sn(4+).

The time evolution of the ratios Sn(0)/Sn(tot) and Sn(4+)/Sn(tot) are shown in Figure 8.3 (c). While Sn(4+) increased rapidly to 32 %, which is roughly 1/3 of the total amount of Sn, Sn(0) decreased from 3 % to 0 % or below the equipment's detection limit. In contrast, the ratio Sn(2+)/Sn(tot) decreases when the sample is exposed 5 h to synthetic air, going from 0.9 to 0.7 (see Figure 8.4).

With this information, it is now possible to assess whether the remaining Sn(2+) was forming $MASnI_3$. Assuming that all remaining I(1-) formed stoichiometric perovskite, each Sn atom in the oxidation state (2+) was bonded to three iodides in the oxidation state (1-). Therefore, the following should be verified:

$$\frac{Sn(2+)}{Sn(tot)} = 3 \cdot \frac{I(1-)}{Sn(tot)} \tag{8.1}$$

However, based on the ratios of the degraded sample, it actually contains an excess of Sn(2+), which is defined here as follows:

$$\frac{Sn(2+)_{excess}}{Sn(tot)} = \frac{Sn(2+)}{Sn(tot)} - 3 \cdot \frac{I(1-)}{Sn(tot)} \tag{8.2}$$

The evolution of the ratios Sn(2+)/Sn(tot) and $Sn(2+)_{excess}$/Sn(tot) is shown in Figure 8.4. As mentioned earlier, the $Sn(2+)/Sn(tot)$ ratio decreased from around 0.95 to 0.68. On the other hand, the $Sn(+2)_{excess}/Sn(tot)$ started negative (due to PEASI contamination) and after 5 h of exposure to synthetic air, the ratio reached 0.21. An excess of Sn (i.e. $Sn(+2)_{excess}/Sn(tot)$) of 0.21 implies that: all the iodide, in the oxidation state (-1), is

bonded to Sn(2+) to form $MASnI_3$ and that 0.21 (out of the total 0.68 of Sn(2+)) must be connected to another element.

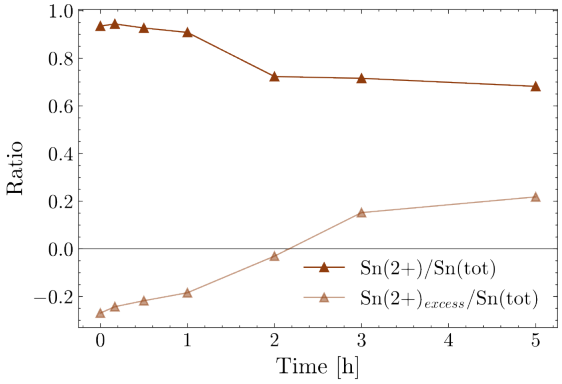

Figure 8.4: Evolution of the ratio Sn(+2)/Sn(tot) and of $Sn(2+)_{excess}$ as a function of the exposure time.

The remaining measured elements to which Sn_{excess} could have bonded are oxygen (bonded as O_{middle} and/or O_{low} and iodide (in the oxidation state I_{high}). One possibility would be to form SnO (Sn in (2+) and O in O_{low}), as previously observed, when the sample was degraded with a drop of water (see Chapter 7). To verify this, it is important to look at the evolution of oxygen with exposure to synthetic air, which is shown in Figure 8.5.

In terms of oxygen, the pristine sample started with a relatively low amount of oxygen, as demonstrated in Figures 8.5 (a) (top) and (b), but increased significantly after 5 h of exposure to synthetic air. Similarly to the exposure to water, only $O_{low}/Sn(tot)$ and $O_{middle}/Sn(tot)$ increased with time, while $O_{high}/Sn(tot)$ remained mostly constant within the error bars (see Figure 8.5 (c)).

Notice that the ratios associated with the degradation products, that is, $I_{high}/Sn(tot)$, $Sn(4+)/Sn(tot)$, $O_{low}/Sn(tot)$ and $O_{middle}/Sn(tot)$, increased at similar rates. By only considering the degradation of synthetic air, it is extremely challenging to disentangle different compounds such as SnO, SnO_2 and SnI_2. For this reason, it is necessary to use what was learned in the chapter on water degradation (Chapter 7). To do so, one must first compare

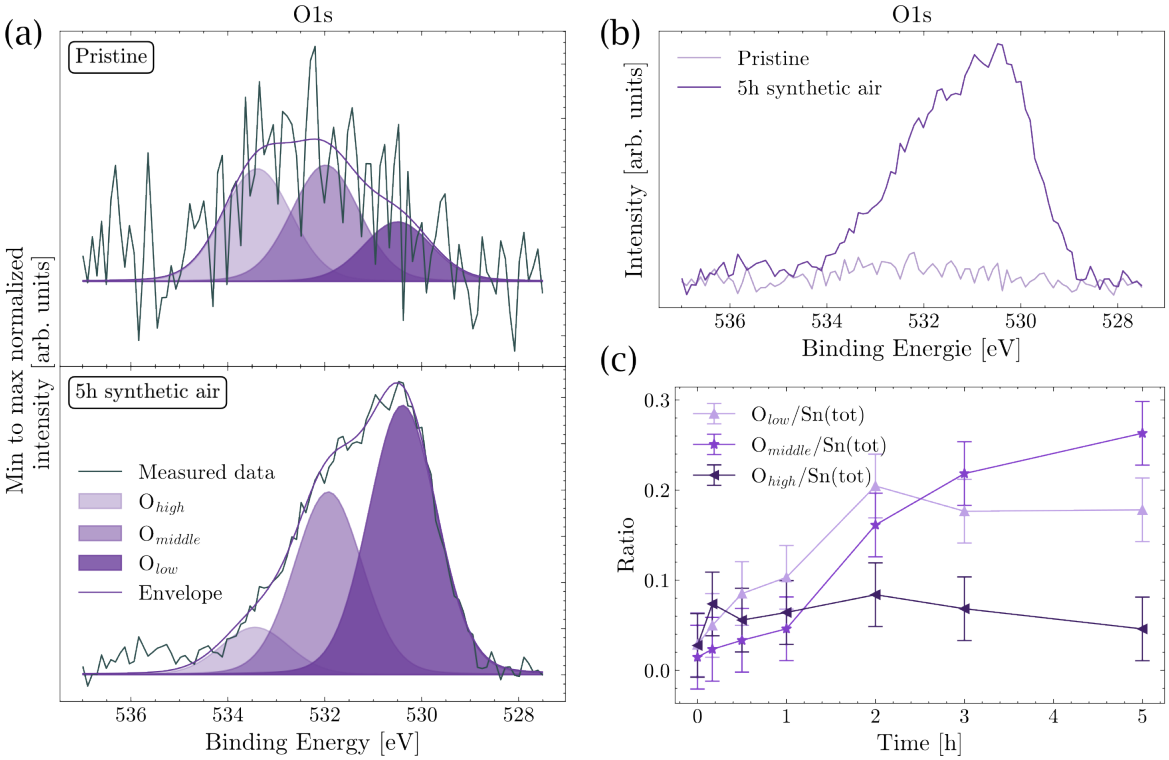

Figure 8.5: Evolution of oxygen in $MASnI_3$ as a function of exposure time to synthetic air. (a) O1s peaks of the pristine sample (top) and the sample exposed to 5 h synthetic air (bottom), fitted with corresponding peak model. (b) Non-normalized O1s peaks of both samples overlapped. (c) Evolution of the O_{low}/Sn(tot), O_{middle}/Sn(tot) and O_{high}/Sn(tot) ratios as a function of the exposure time.

the binding energy of the peaks. By doing so, we ensure that the measured chemical elements have a similar oxidation state and a similar chemical environment.

To do so, a summary of the XPS spectra of Sn3d, I3d, and O1s is shown in Figures 8.6 (a), (b) and (c), respectively. For each figure, the top spectrum corresponds to the pristine sample, the middle spectrum to the sample degraded with synthetic air, and the bottom spectrum shows the sample that was exposed to water vapor.

For all three measurements, the binding energies of Sn(2+) and Sn(4+) were the same (see Figure 8.6 (a)). This is also indicated by the vertical dashed lines in the figures. Similarly, the I3d spectra, in Figure 8.6 (b), I(1-) had the same binding energy in the three spectra, and I_{high} also coincided for both degraded samples. In the O1s spectra, the binding energies

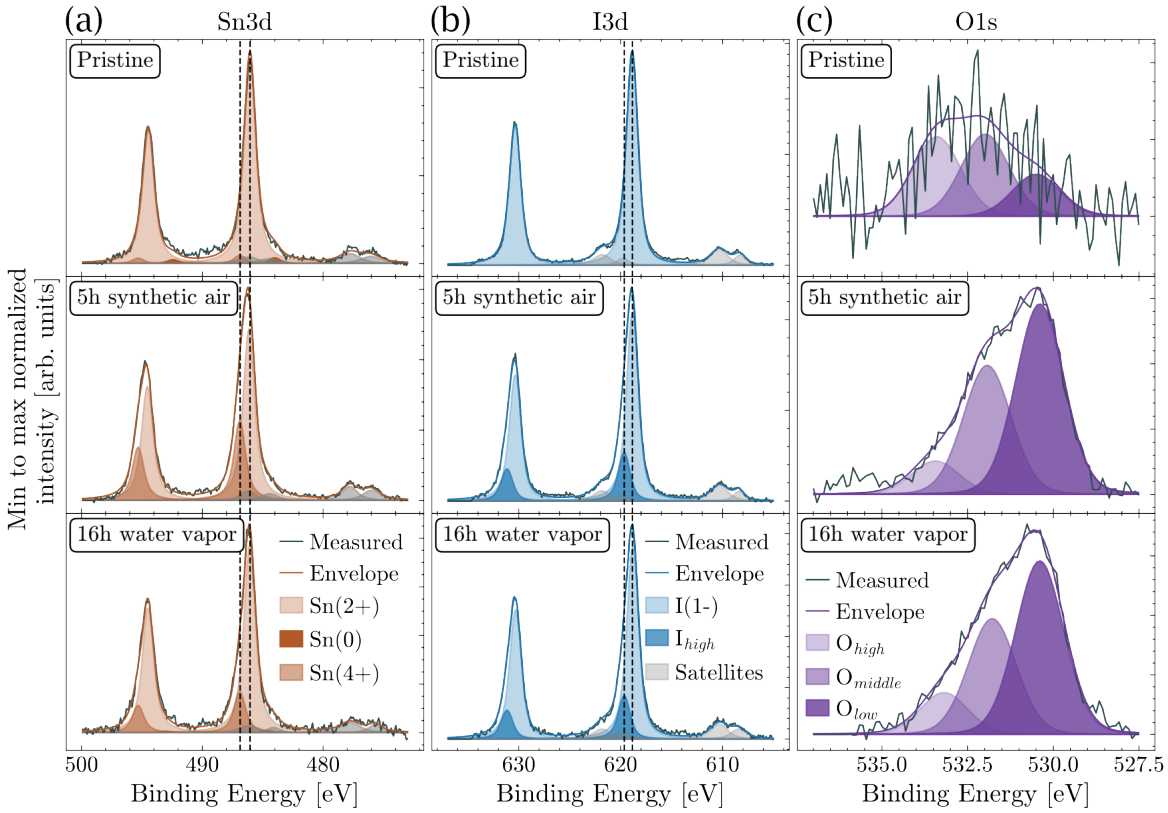

Figure 8.6: Spectra of (a) Sn3d, (b) I3d, (c) O1s of the pristine sample (top), the synthetic air degraded sample (middle) and the water vapor degraded sample.

of the pristine sample tended to differ from the binding energies of the degraded samples. This is because oxygen was present in a very low amount and there was a considerable amount of noise in the measurement. Otherwise, when it comes to the degraded samples, the binding energies of O_{low}, O_{middle}, and O_{high} also coincided for both samples. This means that the degradation products from synthetic air-induced degradation are in an oxidation state / chemical environment similar to that of the degradation products from the water degradation in the chapter 7.

There, it was concluded that O_{low} can either form SnO, where Sn is in the oxidation state (2+) or SnO_2, where O_{low} bonds to Sn(4+). In Figure 8.7 (a) the ratios of O_{low}, Sn(4+) and $Sn(2+)_{excess}$ are plotted. As visible, the amounts of $Sn(2+)_{excess}$ and O_{low} are similar, while the amount of Sn(4+) is almost twice as large. Therefore, it is reasonable to deduce that O_{low} forms SnO with Sn_{excess}.

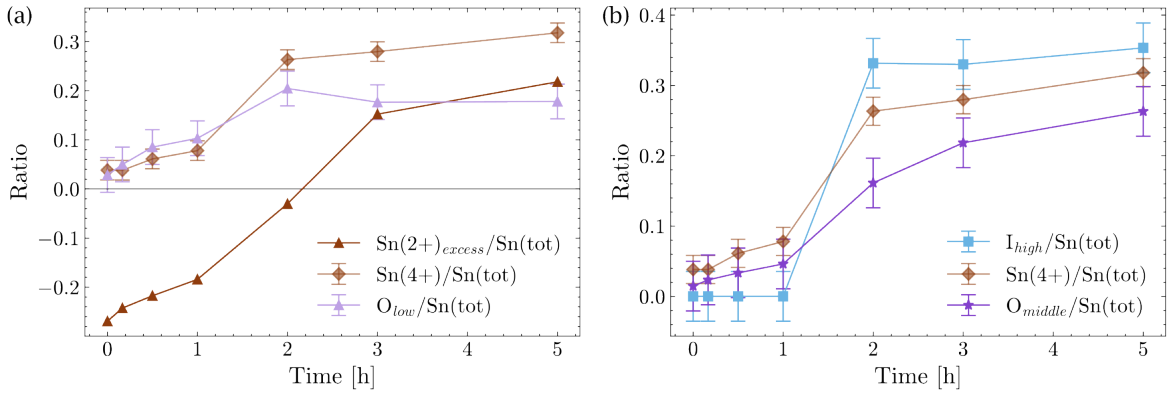

Figure 8.7: (a) Ratio evolution of $Sn(2+)_{excess}$/Sn(tot), Sn(4+)/Sn(tot) and O_{low}/Sn(tot). (b) Ratio evolution of I_{high}/Sn(tot), Sn(4+)/Sn(tot) and O_{middle}/Sn(tot).

The remaining components are therefore Sn(4+), I_{high} and O_{middle} (shown in Figure 8.7 (b)). In chapter 7, a close correlation was observed between the O_{middle} and the I_{high} components. However, here, this was not the case, because $O_{middle}/Sn(tot) = 0.26$, was lower than $I_{high}/Sn(tot) = 0.35$, which means that there was excess I_{high} compared to O_{middle}. This was probably because both components were still interacting with each other, but they also participated in the formation of other products. For example, they could form $Sn(I_x,O_y)$.

In this case, both SnO and $Sn(I_x,O_y)$ would be intermediary compounds before reaching the thermodynamically more stable SnO_2.

It should be noted that most of the components, namely O_{low}, O_{high}, I_{high}, $Sn(4+)$ and $Sn(2+)$ follow a three-phase evolution. This is shown in Figures 8.8 (a) and (b), where phase I is highlighted in darker gray, phase II in lighter gray, and phase III in white. Phase I occurred during the first hour of exposure, and the ratios of the different components hardly changed. In phase II, which occurred during the second hour of exposure, all components changed rapidly. Finally, in phase III, there was a saturation, and the ratios evolved slowly. There could be two distinct reasons for this degradation behavior, which are schematized in Figure 8.8 (c):

1. The O_2 molecules (represented in purple in Figure 8.8 (c) (top)) had a lower sticking coefficient on the pristine $MASnI_3$ surface was low and therefore some time was needed until enough molecules adsorbed onto the surface for the reaction to start. This would have led to slower degradation in phase I. In phase II, oxygen infiltrated the bulk, and the perovskite degraded faster (represented with a purple layer). Finally, in phase III, the degradation occurred mainly beyond 8 nm or 10 nm, which is approximately the XPS probing depth, and as a result the degradation appeared to be slower in the XPS measurement.

2. As already mentioned, this sample is contaminated with PEAI. PEAI is known to form 2D perovskites, such as phenethylammonium tin iodide ($(PEA)_2SnI_4$), which can help improving the stability of normal 3D perovskites [134]. Assuming that $(PEA)_2SnI_4$ made the few top monolayers of the perovskite film (represented in light blue in Figure 8.8 (c) bottom), then phase I was due to a slower reaction of the O_2 molecules with $(PEA)_2SnI_4$. In that case, phase II corresponded to the moment when the oxygen reached the $MASnI_3$ layer in the bulk, and therefore the reaction occurred considerably faster. Finally, like in the previous case, phase III corresponds to the degradation that occurred deeper in the bulk, beyond the XPS probing depth.

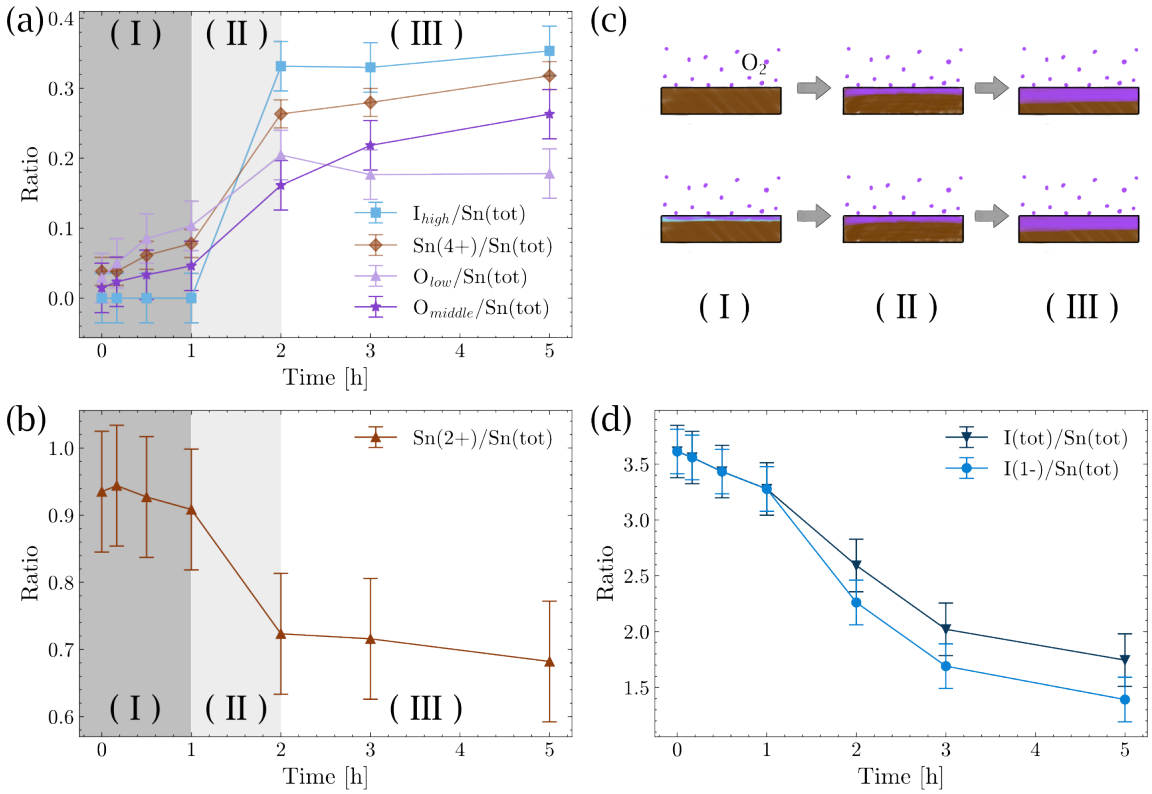

Figure 8.8: Three phase evolution of the ratios of (a) I_{high}, Sn(4+), O_{low}, O_{middle}, and (b) Sn(4+). (c) Schematized representation of the two hypothesis for the existence of three phases. (d) Evolution of the ratios of I(tot) and I(-1).

Unfortunately, the measurements do not allow to distinguish between the two hypotheses. However, it should be noted that the $I(-1)/Sn(tot)$ ratio did not follow the three-phase evolution (see Figure 8.8 (d)). Instead, it shows a slow decrease in the first hour, beyond which the decrease is more pronounced; however, it did not saturate after the second hour. This can be explained by diffusion of ions in the bulk. Most probably, I(1-) was diffusing towards the surface, where it then left the sample.

So far, synthetic air-induced degradation of $MASnI_3$ has been shown to result in the formation of the same oxidation states as the water vapor degradation. However, the ratios of the different components change differently in both degradations, indicating that the degradation products are different. The most obvious difference is that there was no evidence of SnI_2 formation. Furthermore, the XPS ratios had a very different evolution for the synthetic air-induced degradation, which indicated a different degradation mechanism. It was concluded that during degradation SnO and $Sn(O_x,I_y)$ formed as an intermediate decomposition step to form SnO_2, which is more thermodynamically stable.

It is still impossible to compare these two kinds of degradation. Namely, the pressures used during each degradation series were significantly different and therefore the degradation cannot be compared in time. The next section addresses this point by utilizing the flux of oxygen and water molecules interacting with the sample surface.

8.2 Comparison of $MASnI_3$ degradation with water vapor and synthetic air

It is not possible to compare the degradation induced by oxygen and the degradation induced by synthetic air by simply comparing the changes in the ratio as a function of time, because for each experiment the number of molecules in contact with the sample was different. Hence, the flux of molecules hitting the surface of the sample should be considered. In the case of a gas at low pressure, the flux Φ can be expressed as [49],

$$\Phi = \frac{p}{\sqrt{2\pi m k_B T}} \tag{8.3}$$

Where p is the gas pressure, m the molecular mass, k_B the Boltzmann constant and T the temperature. This equation was originally derived by Hertz and is the basis of the Hertz-Knudsen equation (eq. 2.4). Furthermore, in general, by definition, a flux of molecules represents the number of molecules N, divided by the time t and the area A, so,

$$\Phi = \frac{N}{A \cdot t} \tag{8.4}$$

Therefore, the number of molecules per unit area that hit the sample's surface after a time t is given by

$$\frac{N}{A} = \frac{p}{\sqrt{2\pi m k_B T}} \cdot t \tag{8.5}$$

Note that equation 8.3 has multiple assumptions, such as ideal gas, low pressure, no interaction between the gas molecules. None of which is respected here. This is a rough estimate for comparison of the synthetic air- and water-induced degradation. The idea is to understand which of the stresses degrades the perovskite faster. In addition, for air, it is assumed that N_2 and O_2 behave independently of each other; therefore, the mass of oxygen and the partial pressure of oxygen are taken into account independently.

The evolution of the ratios as a function of the molecules that hit the sample's surface is summarized in Figure 8.9. Solid lines represent the degradation caused by O_2, whereas dashed lines represent the degradation caused by water molecules. Interestingly, both oxygen components increased faster when the sample interacted with water than with O_2 (see 8.9 (a)). Similarly, $I_{high}/Sn(tot)$ was formed faster with water 8.9 (b)).

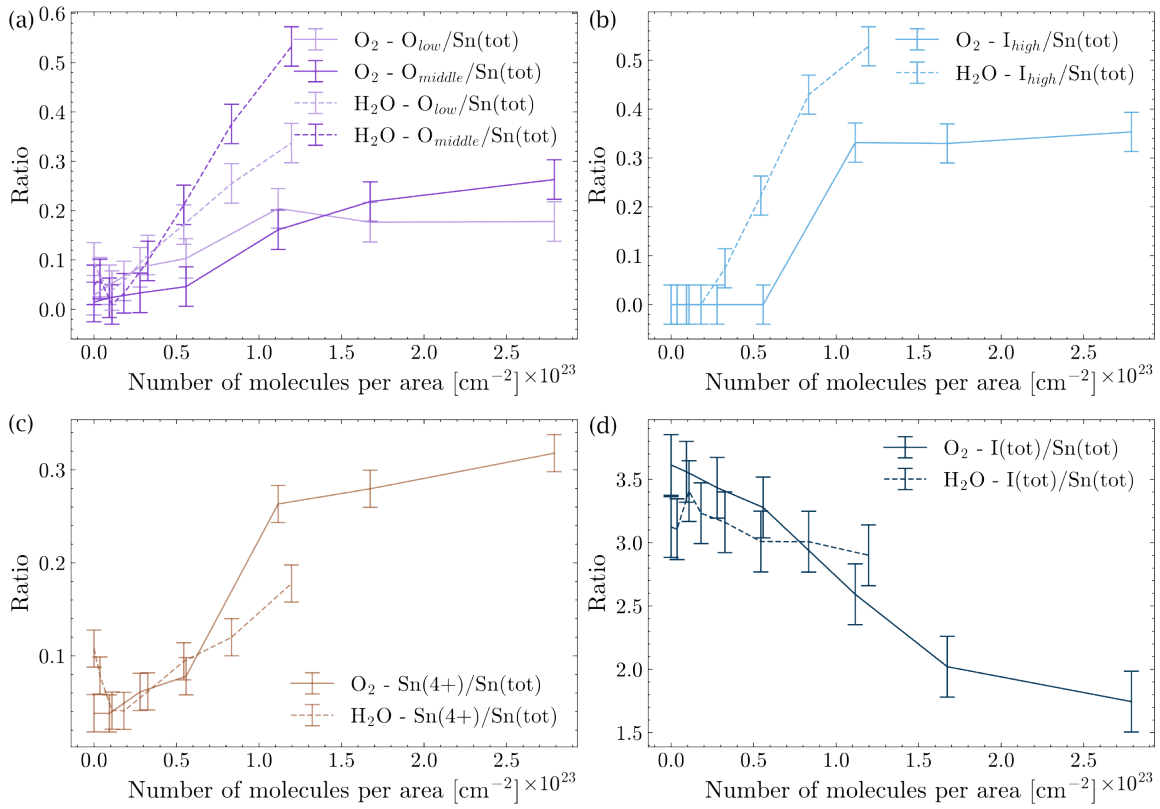

Figure 8.9: Composition ratios as a function of number of collisions of molecules as of water (dashed line) and O_2 (solid line) for (a) O_{low}, O_{middle}, (b) I_{high}, (c) Sn(4+) and (d) I(tot).

However, $Sn(4+)/Sn(tot)$ formed faster with O_2 (see Figure 8.9 (c)) and I(tot) decreased faster with O_2 (Figure 8.9 (d)), which means that iodine evaporated faster. This could happen because O_2 replaced iodine in the crystal, making iodine evaporate faster and oxidizing Sn(2+) into Sn(4+). However, water molecules did not trigger such a fast evaporation of iodine, because an important quantity of SnI_2 was formed during degradation.

Once again, Figure 8.9 highlights that when $MASnI_3$ is exposed to synthetic air and water, it results in different degradation mechanisms and it is important to protect the perovskite film against both. Nevertheless, it is important to note that here the number of molecular interactions with the surface was considered. However, the number of water molecules in the air is significantly lower than the number of O_2 molecules. For example, at 100 % humidity, the number of water molecules in the air is only around 3 % of the air composition. This is important because in the field the perovskite would be less exposed to water molecules than to O_2 molecules.

8.3 Summary

In this chapter, it was shown that exposure to synthetic air degrades $MASnI_3$ films. The degradation mechanism is different from the one observed during exposure to water. Namely, exposure to synthetic air did not form SnI_2, but SnO and an additional phase, which was assumed to contain Sn, O and I (denoted $Sn(O_x,I_y)$). Furthermore, the degradation of water and synthetic air were compared. The quantity of O_{low} and I_{high} was shown to increase faster with the number of molecules O_2 molecules in contact with the sample. Nevertheless, the oxidation of Sn into Sn(4+) and the evaporation of I occurred faster during exposure to water vapor. This was evidence that different mechanisms occur in the samples at different rates depending on the source of the external stress. In any case, both water and oxygen were shown to contribute to the perovskite degradation. Therefore, chemically stabilizing the film is essential through additives, and complementing it with air- and water-tight encapsulation.

Chapter 9

Conclusion

In this thesis, $MASnI_3$ was synthesized using PVD and exposed to different stresses in an effort to determine the degradation pathways of the material.

In a first step, the impact of the deposition parameters and the use of different precursor powders was studied. The crystalline structure of $MASnI_3$ was shown to vary strongly depending on the ratio of MAI vapor to evaporated SnI_2. Furthermore, XRD measurements showed that the crystalline signal of the samples strongly depends on the MAI precursor powder used during the deposition. It was also shown that preconditioning of the PVD chamber is essential to avoid contamination of the samples when other materials are deposited in the same set-up. Finally, a stability study upon storage was conducted and samples were observed to remain stable when stored in an N_2-filled glovebox for up to 15 days. Longer storage significantly increases the risk that the samples are contaminated by impurities in the glovebox.

Second, the impact of UHV and XPS measurements on the sample was studied. Using KPFM and XPS, it was shown that the sample initially contained a contamination layer, probably due to storage in the glovebox, which desorbs when the sample is placed in UHV. Furthermore, when measured in XPS repeatedly, $MASnI_3$ tends to evaporate, without chang-

ing the sample composition significantly. PL measurements suggested that the regions of the sample where $MASnI_3$ evaporated were more prone to degrade; this was translated by a change in the PL peak position of the measurement in the region of the sample exposed to X-rays, compared to that of the region that was not exposed.

Third, a study of the degradation mechanism induced by light was performed in UHV. It was shown that upon illumination, the $MASnI_3$film formed SnI_2 and a small amount of Sn(0). The carbon and nitrogen content also decreased, which was interpreted as MAI or fragments of MAI that evaporated from the surface. A bi-layer model was proposed to describe this system in order to estimate the thickness of the SnI_2 layer that was forming at the surface. Furthermore, the light-induced degradation of SnI_2 and PbI_2 was studied and compared. PbI_2 has shown low stability when exposed to light, whereas no significant changes were observed in the composition of SnI_2. This means that the main cause for the light-induced $MASnI_3$ degradation in UHV is not the use of Sn, but rather the evaporation of the MAI.

Fourth, water-induced degradation of $MASnI_3$ was studied and was found to mainly form SnI_2, independently of whether the sample was exposed to liquid water or water vapor. In addition, the formation of SnO and SnO_2 was detected.

Finally, the last degradation study consisted of exposing $MASnI_3$ to synthetic air. Unlike the previous two degradation studies, here the sample did not show any sign of SnI_2 formation. From the trends of the composition ratios, it was concluded that the sample formed SnO and another product that contained tin, iodine, and oxygen. Furthermore, degradation induced by water and by oxygen were compared by taking into account the number of molecules that interacted with the sample. From this analysis, it was concluded that both stresses degrade $MASnI_3$ but with different degradation mechanisms. That is, the quantity of oxygen contamination and of the secondary iodine component increased faster with exposure to O_2. However, the oxidation of tin into (4+) and iodine evaporation was faster with water exposure.

It is important to note that the formation of SnI_4 was not detected in any of the degradation studies, contrary to the solvent-based synthesis reports in the literature. Therefore, it is highly probable that the formation of SnI_4 is precisely caused by the use of solvents in the synthesis of Sn-based perovskites. Thus, a solution to avoid the formation of SnI_4 is to avoid the use of solvents or replace them with alternatives that do not oxidize the perovskite.

Chapter 10

Appendix

10.1 Composition evolution of $MASnI_3$ in vacuum

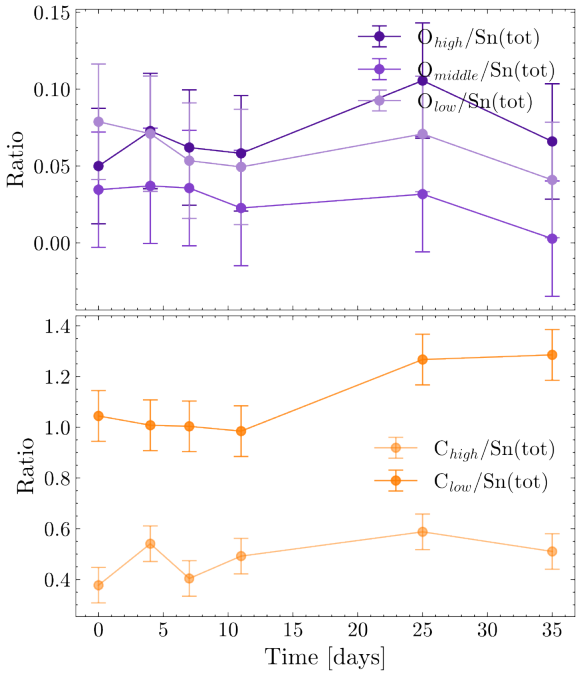

Figure A1: Evolution of the ratios of O/Sn and C/Sn at the $MASnI_3$ surface, as a function of time in vacuum.

10.2 Crystalline structure of $MASnI_3$ after degradation with a water drop

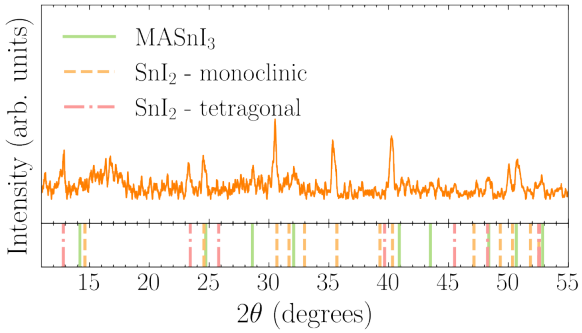

Figure A2: XRD of $MASnI_3$ after degradation with a water drop

10.3 Crystalline structure of $MASnI_3$ after 5h degradation with synthetic air

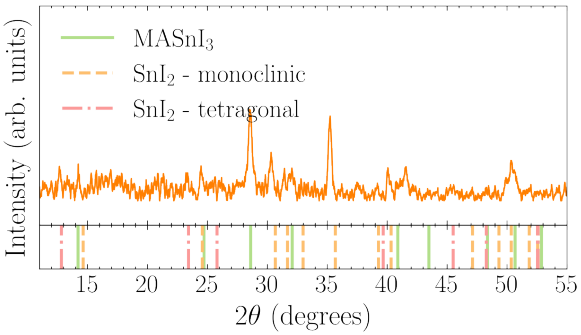

Figure A3: XRD of $MASnI_3$ after 5h exposure to synthetic air

References

[1] National Renewable Energy Laboratory (NREL). *Best Research-Cell Efficiency Chart.* Accessed: 2024-05-28. 2024. URL: https://www.nrel.gov/pv/cell-efficiency.html.

[2] *Energy Institute - Statistical Review of World Energy (2024); Smil (2017) – with major processing by Our World in Data. "Primary energy from biofuels" [dataset]. Energy Institute, "Statistical Review of World Energy"; Smil, "Energy Transitions: Global and National Perspectives" [original data].* Accessed: 2024-09-24. URL: https://ourworldindata.org/energy.

[3] *Global Carbon Budget (2023); Population based on various sources (2023) – with major processing by Our World in Data. "Consumption-based emissions per capita – Global Carbon Project" [dataset]. Global Carbon Project, "Global Carbon Budget"; Various sources, "Population" [original data].* Accessed: 2024-09-24. URL: https://ourworldindata.org/worlds-energy-problem.

[4] *IPCC, 2023: Sections. In: Climate Change 2023: Synthesis Report. Contribution of Working Groups I, II and III to the Sixth Assessment Report of the Intergovernmental Panel on Climate Change [Core Writing Team, H. Lee and J. Romero (eds.)]. IPCC, Geneva, Switzerland, pp. 35-115, doi: 10.59327/IPCC/AR6-9789291691647.*

[5] World Meteorological Organization (WMO). *WMO confirms that 2023 smashes global temperature record.* Accessed: 2024-09-24. URL: https://wmo.int/news/media-centre/wmo-confirms-2023-smashes-global-temperature-record.

[6] Justyna Pastuszak and Paweł Wegierek. "Photovoltaic Cell Generations and Current Research Directions for Their Development". In: *Materials* 15.16 (Aug. 2022), p. 5542. ISSN: 1996-1944. DOI: 10.3390/ma15165542. URL: https://www.mdpi.com/1996-1944/15/16/5542.

[7] Seiji Hayashi, Ryozo Aoki, and Tetsurö Nakamura. "Metallic conductivity in perovskite-type compounds AMoO3 (A = Ba, Sr, Ca) down to 2.5K". In: *Materials Research Bulletin* 14.3 (Mar. 1979), pp. 409–413. ISSN: 00255408. DOI: 10.1016/0025-5408(79)90107-7. URL: https://linkinghub.elsevier.com/retrieve/pii/0025540879901077.

[8] Jerry B. Torrance et al. "Simple and perovskite oxides of transition-metals: Why some are metallic, while most are insulating". In: *Journal of Solid State Chemistry* 90.1 (Jan. 1991), pp. 168–172. ISSN: 00224596. DOI: 10.1016/0022-4596(91)90182-H. URL: https://linkinghub.elsevier.com/retrieve/pii/002245969190182H.

[9] A. M. Gabovich, D. P. Moiseev, and A. S. Shpigel. "Nature of superconductivity in $BaPb_{(1-x)}Bi_xO_3$ solid solutions with perovskite structure. Role of dielectrization of the electron spectrum". In: *Soviet physics, JETP* 56.4 (1982), pp. 795–798.

[10] J Provost et al. "The oxygen defect perovskites $Ba_3La_3Cu_6O_{14+y}$: A progressive transition from semi-conductive to semi-metallic properties. I. Structural aspects and energy levels". In: *Synthetic Metals* 4.2 (1981), pp. 147–155.

[11] Akihiro Kojima et al. "Organometal Halide Perovskites as Visible-Light Sensitizers for Photovoltaic Cells". In: *Journal of the American Chemical Society* 131.17 (May 2009), pp. 6050–6051. ISSN: 0002-7863. DOI: 10.1021/ja809598r. URL: https://pubs.acs.org/doi/10.1021/ja809598r.

[12] University of Science and Technology of China (USTC). *USTC Set New Record in Perovskite Cell Efficiency*. Accessed: 2024-06-01. 2023. URL: https://en.ustc.edu.cn/info/1007/4676.htm.

[13] Zheng Liang et al. “Homogenizing out-of-plane cation composition in perovskite solar cells”. In: *Nature* 624.7992 (Dec. 2023), pp. 557–563. ISSN: 0028-0836. DOI: 10.1038/s41586-023-06784-0. URL: https://www.nature.com/articles/s41586-023-06784-0.

[14] LONGi. *LONGi Sets a New World Record of* 27.09% *for the Efficiency of Silicon Heterojunction Back-Contact (HBC) Solar Cells*. Accessed: 2024-06-01. 2023. URL: https://www.longi.com/en/news/heterojunction-back-contact-battery/.

[15] Eugene A. Katz. “Perovskite: Name Puzzle and German-Russian Odyssey of Discovery”. In: *Helvetica Chimica Acta* 103.6 (June 2020). ISSN: 0018-019X. DOI: 10.1002/hlca.202000061. URL: https://onlinelibrary.wiley.com/doi/10.1002/hlca.202000061.

[16] Gustav Rose. “Beschreibung einiger neuen Mineralien des Urals”. In: *Annalen der Physik* 126.8 (Jan. 1840), pp. 652–656. ISSN: 0003-3804. DOI: 10.1002/andp.18401260807. URL: https://onlinelibrary.wiley.com/doi/10.1002/andp.18401260807.

[17] Lei Chen et al. “On the Durability of Tin-Containing Perovskite Solar Cells”. In: *Advanced Science* 11.1 (Jan. 2024), pp. 1–22. ISSN: 2198-3844. DOI: 10.1002/advs.202304811. URL: https://onlinelibrary.wiley.com/doi/10.1002/advs.202304811.

[18] Nam-gyu Park, Michael Grätzel, and Tsutomu Miyasaka, eds. *Organic- Inorganic Halide Perovskite Photovoltaics - From Fundamental to Device Architectures*. Cham: Springer International Publishing, 2016. ISBN: 978-3-319-35112-4. DOI: 10.1007/978-3-319-35114-8. URL: http://link.springer.com/10.1007/978-3-319-35114-8.

[19] Javier García-Ben et al. “Narrowing the tolerance factor limits for hybrid organic-inorganic dicyanamide-perovskites”. In: *Journal of Solid State Chemistry* 316.June (2022). ISSN: 1095726X. DOI: 10.1016/j.jssc.2022.123635.

[20] Hui-Seon Kim et al. “Lead Iodide Perovskite Sensitized All-Solid-State Submicron Thin Film Mesoscopic Solar Cell with Efficiency Exceeding 9%”. In: *Scientific Reports* 2.1 (Aug. 2012), p. 591. ISSN: 2045-2322. DOI: 10.1038/srep00591. URL: https://www.nature.com/articles/srep00591.

[21] Madad Abbasli et al. “Tin Halide Perovskite Epitaxial Films on Gold Surfaces: Atomic Structure and Stability”. In: *Advanced Functional Materials* 2403680 (May 2024), pp. 1–8. ISSN: 1616-301X. DOI: 10.1002/adfm.202403680. URL: https://onlinelibrary.wiley.com/doi/10.1002/adfm.202403680.

[22] Eran Edri et al. “Chloride Inclusion and Hole Transport Material Doping to Improve Methyl Ammonium Lead Bromide Perovskite-Based High Open-Circuit Voltage Solar Cells”. In: *The Journal of Physical Chemistry Letters* 5.3 (Feb. 2014), pp. 429–433. ISSN: 1948-7185. DOI: 10.1021/jz402706q. URL: https://pubs.acs.org/doi/10.1021/jz402706q.

[23] Constantinos C. Stoumpos, Christos D. Malliakas, and Mercouri G. Kanatzidis. “Semiconducting Tin and Lead Iodide Perovskites with Organic Cations: Phase Transitions, High Mobilities, and Near-Infrared Photoluminescent Properties”. In: *Inorganic Chemistry* 52.15 (Aug. 2013), pp. 9019–9038. ISSN: 0020-1669. DOI: 10.1021/ic401215x. URL: https://pubs.acs.org/doi/10.1021/ic401215x.

[24] Thirumal Krishnamoorthy et al. “Lead-free germanium iodide perovskite materials for photovoltaic applications”. In: *Journal of Materials Chemistry A* 3.47 (2015), pp. 23829–23832. ISSN: 2050-7488. DOI: 10.1039/C5TA05741H. URL: https://xlink.rsc.org/?DOI=C5TA05741H.

[25] Giles E. Eperon et al. “Formamidinium lead trihalide: a broadly tunable perovskite for efficient planar heterojunction solar cells”. In: *Energy & Environmental Science* 7.3 (2014), p. 982. ISSN: 1754-5692. DOI: 10.1039/c3ee43822h. URL: https://xlink.rsc.org/?DOI=c3ee43822h.

[26] Jun Hong Noh et al. “Chemical Management for Colorful, Efficient, and Stable Inorganic–Organic Hybrid Nanostructured Solar Cells”. In: *Nano Letters* 13.4 (Apr. 2013),

pp. 1764–1769. ISSN: 1530-6984. DOI: 10.1021/nl400349b. URL: https://pubs.acs.org/doi/10.1021/nl400349b.

[27] Ian C. Smith et al. "A Layered Hybrid Perovskite Solar-Cell Absorber with Enhanced Moisture Stability". In: *Angewandte Chemie* 126.42 (Oct. 2014), pp. 11414–11417. ISSN: 0044-8249. DOI: 10.1002/ange.201406466. URL: https://onlinelibrary.wiley.com/doi/10.1002/ange.201406466.

[28] Yehao Deng et al. "Scalable fabrication of efficient organolead trihalide perovskite solar cells with doctor-bladed active layers". In: *Energy & Environmental Science* 8.5 (2015), pp. 1544–1550. ISSN: 1754-5692. DOI: 10.1039/C4EE03907F. URL: https://xlink.rsc.org/?DOI=C4EE03907F.

[29] Yue Yu et al. "Thermally evaporated methylammonium tin triiodide thin films for lead-free perovskite solar cell fabrication". In: *RSC Advances* 6.93 (2016), pp. 90248–90254. ISSN: 2046-2069. DOI: 10.1039/C6RA19476A. URL: https://xlink.rsc.org/?DOI=C6RA19476A.

[30] Matthew R. Leyden et al. "High performance perovskite solar cells by hybrid chemical vapor deposition". In: *J. Mater. Chem. A* 2.44 (2014), pp. 18742–18745. ISSN: 2050-7488. DOI: 10.1039/C4TA04385E. URL: https://xlink.rsc.org/?DOI=C4TA04385E.

[31] Jiantao Wang et al. "Enhancing Photostability of Sn-Pb Perovskite Solar Cells by an Alkylammonium Pseudo-Halogen Additive". In: *Advanced Energy Materials* 13.15 (Apr. 2023), pp. 1–8. ISSN: 1614-6832. DOI: 10.1002/aenm.202204115. URL: https://onlinelibrary.wiley.com/doi/10.1002/aenm.202204115.

[32] Ziyuan Chen et al. "Perovskite Grain-Boundary Manipulation Using Room-Temperature Dynamic Self-Healing "Ligaments" for Developing Highly Stable Flexible Perovskite Solar Cells with 23.8% Efficiency". In: *Advanced Materials* 35.18 (May 2023), pp. 1–10. ISSN: 0935-9648. DOI: 10.1002/adma.202300513. URL: https://onlinelibrary.wiley.com/doi/10.1002/adma.202300513.

[33] Lu Yang et al. “25.24%-Efficiency FACsPbI3 Perovskite Solar Cells Enabled by Intermolecular Esterification Reaction of DL-Carnitine Hydrochloride”. In: *Advanced Materials* 35.16 (Apr. 2023), pp. 1–10. ISSN: 0935-9648. DOI: 10.1002/adma.202211545. URL: https://onlinelibrary.wiley.com/doi/10.1002/adma.202211545.

[34] Jeremy Hieulle et al. “Understanding and decoupling the role of wavelength and defects in light-induced degradation of metal-halide perovskites”. In: *Energy & Environmental Science* 17.1 (2023), pp. 284–295. ISSN: 1754-5692. DOI: 10.1039/D3EE03511E. URL: https://xlink.rsc.org/?DOI=D3EE03511E.

[35] Xiaofeng Tang et al. “Photoinduced degradation of methylammonium lead triiodide perovskite semiconductors”. In: *Journal of Materials Chemistry A* 4.41 (2016), pp. 15896–15903. ISSN: 2050-7488. DOI: 10 . 1039 / C6TA06497C. URL: https://xlink.rsc.org/?DOI=C6TA06497C.

[36] Joong Il Jake Choi et al. “Pathways of Water-Induced Lead-Halide Perovskite Surface Degradation: Insights from In Situ Atomic-Scale Analysis”. In: *ACS Nano* 17.24 (Dec. 2023), pp. 25679–25688. ISSN: 1936-0851. DOI: 10 . 1021 / acsnano . 3c10611. URL: https://pubs.acs.org/doi/10.1021/acsnano.3c10611.

[37] Edoardo Mosconi, Jon M Azpiroz, and Filippo De Angelis. “Ab Initio Molecular Dynamics Simulations of Methylammonium Lead Iodide Perovskite Degradation by Water”. In: *Chemistry of Materials* 27.13 (July 2015), pp. 4885–4892. ISSN: 0897-4756. DOI: 10 . 1021 / acs . chemmater . 5b01991. URL: https : //pubs . acs . org/doi/10 . 1021/acs.chemmater.5b01991.

[38] Yang Bai et al. “Decoupling light- and oxygen-induced degradation mechanisms of Sn–Pb perovskites in all perovskite tandem solar cells”. In: *Energy & Environmental Science* (2024). ISSN: 1754-5692. DOI: 10.1039/D4EE02427C. URL: https://xlink.rsc.org/?DOI=D4EE02427C.

[39] Guo Xie et al. “Insight into the reaction mechanism of water, oxygen and nitrogen molecules on a tin iodine perovskite surface”. In: *Journal of Materials Chemistry A*

7.10 (2019), pp. 5779–5793. ISSN: 2050-7488. DOI: 10.1039/C8TA11705E. URL: https://xlink.rsc.org/?DOI=C8TA11705E.

[40] Dominik J. Kubicki et al. "Local Structure and Dynamics in Methylammonium, Formamidinium, and Cesium Tin(II) Mixed-Halide Perovskites from 119Sn Solid-State NMR". In: *Journal of the American Chemical Society* 142.17 (Apr. 2020), pp. 7813–7826. ISSN: 0002-7863. DOI: 10.1021/jacs.0c00647. URL: https://pubs.acs.org/doi/10.1021/jacs.0c00647.

[41] William Shockley and Hans J. Queisser. "Detailed Balance Limit of Efficiency of p-n Junction Solar Cells". In: *Journal of Applied Physics* 32.3 (Mar. 1961), pp. 510–519. ISSN: 0021-8979. DOI: 10.1063/1.1736034. URL: https://pubs.aip.org/jap/article/32/3/510/505950/Detailed-Balance-Limit-of-Efficiency-of-p-n.

[42] Koji Yamada et al. "127I-NQR , 119Sn Mössbauer Effect, and Electrical Conductivity of $MSnI_3$". In: *Zeitschrift für Naturforschung* 45A (1990), p. 307.

[43] D.B. Mitzi et al. "Transport, Optical, and Magnetic Properties of the Conducting Halide Perovskite $CH_3NH_3SnI_3$". In: *Journal of Solid State Chemistry* 114.1 (Jan. 1995), pp. 159–163. ISSN: 00224596. DOI: 10.1006/jssc.1995.1023. URL: https://linkinghub.elsevier.com/retrieve/pii/S0022459685710237.

[44] Feng Hao et al. "Lead-free solid-state organic–inorganic halide perovskite solar cells". In: *Nature Photonics* 8.6 (June 2014), pp. 489–494. ISSN: 1749-4885. DOI: 10.1038/nphoton.2014.82. URL: https://www.nature.com/articles/nphoton.2014.82.

[45] Bin-Bin Yu et al. "Heterogeneous 2D/3D Tin-Halides Perovskite Solar Cells with Certified Conversion Efficiency Breaking 14%". In: *Advanced Materials* 33.36 (Sept. 2021), pp. 1–10. ISSN: 0935-9648. DOI: 10.1002/adma.202102055. URL: https://onlinelibrary.wiley.com/doi/10.1002/adma.202102055.

[46] Gengling Liu et al. "Synergic Electron and Defect Compensation Minimizes Voltage Loss in Lead-Free Perovskite Solar Cells". In: *Angewandte Chemie International Edition* 62.39 (Sept. 2023). ISSN: 1433-7851. DOI: 10.1002/anie.202305551. URL: https://onlinelibrary.wiley.com/doi/10.1002/anie.202305551.

[47] Feng Wang et al. “Organic Cation-Dependent Degradation Mechanism of Organotin Halide Perovskites”. In: *Advanced Functional Materials* 26.20 (May 2016), pp. 3417–3423. ISSN: 1616-301X. DOI: 10.1002/adfm.201505127. URL: https://onlinelibrary.wiley.com/doi/10.1002/adfm.201505127.

[48] Luis Lanzetta et al. “Degradation mechanism of hybrid tin-based perovskite solar cells and the critical role of tin (IV) iodide”. In: *Nature Communications* 12.1 (May 2021), p. 2853. ISSN: 2041-1723. DOI: 10.1038/s41467-021-22864-z. URL: https://www.nature.com/articles/s41467-021-22864-z.

[49] K. S. Sree Harsha. *Principles of Physical Vapor Deposition of Thin Films*. Elsevier, 2016, pp. 1–23. ISBN: 2013206534.

[50] Ivan V. Markov. *Crystal Growth For Beginners - Fundamentals of Nucleation, Crystal Growth and Epitaxy*. 2nd Editio. World Scientific, 2003. ISBN: 9812382453.

[51] James E. Bishop et al. “Fully Spray-Coated Triple-Cation Perovskite Solar Cells”. In: *Scientific Reports* 10.1 (Apr. 2020), p. 6610. ISSN: 2045-2322. DOI: 10.1038/s41598-020-63674-5. URL: http://dx.doi.org/10.1038/s41598-020-63674-5%20https://www.nature.com/articles/s41598-020-63674-5.

[52] Florian Mathies et al. “Multipass inkjet printed planar methylammonium lead iodide perovskite solar cells”. In: *Journal of Materials Chemistry A* 4.48 (2016), pp. 19207–19213. ISSN: 2050-7488. DOI: 10.1039/C6TA07972E. URL: https://xlink.rsc.org/?DOI=C6TA07972E.

[53] Liguo Tan et al. “Combined Vacuum Evaporation and Solution Process for High-Efficiency Large-Area Perovskite Solar Cells with Exceptional Reproducibility”. In: *Advanced Materials* 35.13 (Mar. 2023), pp. 1–9. ISSN: 0935-9648. DOI: 10.1002/adma.202205027. URL: https://onlinelibrary.wiley.com/doi/10.1002/adma.202205027.

[54] Tobias Abzieher et al. “Vapor phase deposition of perovskite photovoltaics: short track to commercialization?” In: *Energy & Environmental Science* 17.5 (2024), pp. 1645–

1663. ISSN: 1754-5692. DOI: 10.1039/D3EE03273F. URL: https://xlink.rsc.org/?DOI=D3EE03273F.

[55] D. B. Mitzi, M. T. Prikas, and K. Chondroudis. "Thin Film Deposition of Organic-Inorganic Hybrid Materials Using a Single Source Thermal Ablation Technique". In: *Chemistry of Materials* 11.3 (Mar. 1999), pp. 542–544. ISSN: 0897-4756. DOI: 10.1021/cm9811139. URL: https://pubs.acs.org/doi/10.1021/cm9811139.

[56] Woojun Yoon et al. "Vapor deposition of organic-inorganic hybrid perovskite thin-films for photovoltaic applications". In: *2014 IEEE 40th Photovoltaic Specialist Conference (PVSC)*. IEEE, June 2014, pp. 1577–1580. ISBN: 978-1-4799-4398-2. DOI: 10.1109/PVSC.2014.6925219. URL: http://ieeexplore.ieee.org/document/6925219/.

[57] Adrian Llanos, Emmanuel S. Thibau, and Zheng-Hong Lu. "Abnormal thin film structures in vapor-phase deposited methylammonium lead iodide perovskite". In: *Journal of Vacuum Science & Technology A: Vacuum, Surfaces, and Films* 34.6 (Nov. 2016), pp. 1–6. ISSN: 0734-2101. DOI: 10.1116/1.4963071. URL: https://pubs.aip.org/jva/article/34/6/060601/244970/Abnormal-thin-film-structures-in-vapor-phase.

[58] Tobias Abzieher et al. "From Groundwork to Efficient Solar Cells: On the Importance of the Substrate Material in Co-Evaporated Perovskite Solar Cells". In: *Advanced Functional Materials* 31.42 (Oct. 2021). ISSN: 1616-301X. DOI: 10.1002/adfm.202104482. URL: https://onlinelibrary.wiley.com/doi/10.1002/adfm.202104482.

[59] Thibaut Gallet et al. "Co-evaporation of CH3NH3PbI3: How Growth Conditions Impact Phase Purity, Photostriction, and Intrinsic Stability". In: *ACS Applied Materials & Interfaces* 13.2 (Jan. 2021), pp. 2642–2653. ISSN: 1944-8244. DOI: 10.1021/acsami.0c19038. URL: https://pubs.acs.org/doi/10.1021/acsami.0c19038.

[60] Karl L. Heinze et al. "Importance of methylammonium iodide partial pressure and evaporation onset for the growth of co-evaporated methylammonium lead iodide absorbers". In: *Scientific Reports* 11.1 (July 2021), p. 15299. ISSN: 2045-2322. DOI: 10.

1038/s41598-021-94689-1. URL: https://www.nature.com/articles/s41598-021-94689-1.

[61] Heinz-Helmut Perkampus. *UV-VIS Spectroscopy and Its Applications*. Springer Berlin, Heidelberg, 1992.

[62] Azat F. Akbulatov et al. "Comparative Intrinsic Thermal and Photochemical Stability of Sn(II) Complex Halides as Next-Generation Materials for Lead-Free Perovskite Solar Cells". In: *The Journal of Physical Chemistry C* 123.44 (Nov. 2019), pp. 26862–26869. ISSN: 1932-7447. DOI: 10.1021/acs.jpcc.9b09200. URL: https://pubs.acs.org/doi/10.1021/acs.jpcc.9b09200.

[63] Tomas Leijtens et al. "Mechanism of Tin Oxidation and Stabilization by Lead Substitution in Tin Halide Perovskites". In: *ACS Energy Letters* 2.9 (Sept. 2017), pp. 2159–2165. ISSN: 2380-8195. DOI: 10.1021/acsenergylett.7b00636. URL: https://pubs.acs.org/doi/10.1021/acsenergylett.7b00636.

[64] Daniel Abou-ras, Thomas Kirchartz, and Uwe Rau, eds. *Advanced Characterization Techniques for Thin Film Solar Cells*. 2011. ISBN: 9783527408573.

[65] Xiaofeng Tang et al. "Local Observation of Phase Segregation in Mixed-Halide Perovskite". In: *Nano Letters* 18.3 (Mar. 2018), pp. 2172–2178. ISSN: 1530-6984. DOI: 10.1021/acs.nanolett.8b00505. URL: https://pubs.acs.org/doi/10.1021/acs.nanolett.8b00505.

[66] Thilo Glatzel Sascha Sadewasser. *Kelvin Probe Force Microscopy, From Single Charge Detection to Device Characterization*. Springer Cham, 2018.

[67] Jae Sung Yun et al. "Humidity-Induced Degradation via Grain Boundaries of $HC(NH_2)_2PbI_3$ Planar Perovskite Solar Cells". In: *Advanced Functional Materials* 28.11 (Mar. 2018), pp. 1–8. ISSN: 1616-301X. DOI: 10.1002/adfm.201705363. URL: https://onlinelibrary.wiley.com/doi/10.1002/adfm.201705363.

[68] Siegfried Hofmann. *Auger- and X-Ray Photoelectron Spectroscopy in Materials Science*. Vol. 49. Springer Series in Surface Sciences. Berlin, Heidelberg: Springer Berlin

Heidelberg, 2013. ISBN: 978-3-642-27380-3. DOI: 10.1007/978-3-642-27381-0. URL: https://link.springer.com/10.1007/978-3-642-27381-0.

[69] Jue Gong et al. "Suppressed Oxidation and Photodarkening of Hybrid Tin Iodide Perovskite Achieved with Reductive Organic Small Molecule". In: *ACS Applied Energy Materials* 4.5 (May 2021), pp. 4704–4710. ISSN: 2574-0962. DOI: 10.1021/acsaem.1c00316. URL: https://pubs.acs.org/doi/10.1021/acsaem.1c00316.

[70] Yvonne J. Hofstetter et al. "Vacuum-Induced Degradation of 2D Perovskites". In: *Frontiers in Chemistry* 8.February (Feb. 2020), pp. 1–10. ISSN: 2296-2646. DOI: 10.3389/fchem.2020.00066. URL: https://www.frontiersin.org/article/10.3389/fchem.2020.00066/full.

[71] Junke Liu et al. "Origins and Suppression of Sn(II)/Sn(IV) Oxidation in Tin Halide Perovskite Solar Cells". In: *Advanced Energy Materials* 13.23 (June 2023). ISSN: 1614-6832. DOI: 10.1002/aenm.202300696. URL: https://onlinelibrary.wiley.com/doi/10.1002/aenm.202300696.

[72] Damiano Ricciarelli et al. "Instability of Tin Iodide Perovskites: Bulk p-Doping versus Surface Tin Oxidation". In: *ACS Energy Letters* 5.9 (Sept. 2020), pp. 2787–2795. ISSN: 2380-8195. DOI: 10.1021/acsenergylett.0c01174. URL: https://pubs.acs.org/doi/10.1021/acsenergylett.0c01174.

[73] Makhsud I. Saidaminov et al. "Conventional Solvent Oxidizes Sn(II) in Perovskite Inks". In: *ACS Energy Letters* 5.4 (Apr. 2020), pp. 1153–1155. ISSN: 2380-8195. DOI: 10.1021/acsenergylett.0c00402. URL: https://pubs.acs.org/doi/10.1021/acsenergylett.0c00402.

[74] M. V. Gavrilin, G. V. Sen'chukova, and E. V. Kompantseva. "Structure of chemical compounds, methods of analysis and process control: Methods for the synthesis and analysis of dimethyl sulfoxide (a review)". In: *Pharmaceutical Chemistry Journal* 34.9 (Sept. 2000), pp. 35–38. ISSN: 0091150X. URL: https://link.springer.com/10.1007/s11094-011-0546-6.

[75] Zhihao Zhang et al. “Mechanistic Understanding of Oxidation of Tin-based Perovskite Solar Cells and Mitigation Strategies”. In: *Angewandte Chemie* 135.45 (Nov. 2023). ISSN: 0044-8249. DOI: 10.1002/ange.202308093. URL: https://onlinelibrary.wiley.com/doi/10.1002/ange.202308093.

[76] Luis Huerta Hernandez et al. “The role of A-site composition in the photostability of tin–lead perovskite solar cells”. In: *Sustainable Energy & Fuels* 6.20 (2022), pp. 4605–4613. ISSN: 2398-4902. DOI: 10.1039/D2SE00663D. URL: https://xlink.rsc.org/?DOI=D2SE00663D.

[77] Chongwen Li et al. “Low-bandgap mixed tin–lead iodide perovskites with reduced methylammonium for simultaneous enhancement of solar cell efficiency and stability”. In: *Nature Energy* 5.10 (Oct. 2020), pp. 768–776. ISSN: 2058-7546. DOI: 10.1038/s41560-020-00692-7. URL: https://www.nature.com/articles/s41560-020-00692-7.

[78] Xiao Liu et al. “Efficient and stable tin perovskite solar cells enabled by amorphous-polycrystalline structure”. In: *Nature Communications* 11.1 (May 2020), p. 2678. ISSN: 2041-1723. DOI: 10.1038/s41467-020-16561-6. URL: https://www.nature.com/articles/s41467-020-16561-6.

[79] Jesús Sanchez-Diaz et al. “Tin perovskite solar cells with >1,300 h of operational stability in N_2 through a synergistic chemical engineering approach”. In: *Joule* 6.4 (Apr. 2022), pp. 861–883. ISSN: 25424351. DOI: 10.1016/j.joule.2022.02.014. URL: https://linkinghub.elsevier.com/retrieve/pii/S2542435122000952.

[80] Qihua Li et al. “Compositional effect on water adsorption on metal halide perovskites”. In: *Applied Surface Science* 538.October 2020 (Feb. 2021), p. 148058. ISSN: 01694332. DOI: 10.1016/j.apsusc.2020.148058. URL: https://linkinghub.elsevier.com/retrieve/pii/S0169433220328154.

[81] Jarvist M. Frost et al. “Atomistic Origins of High-Performance in Hybrid Halide Perovskite Solar Cells”. In: *Nano Letters* 14.5 (May 2014), pp. 2584–2590. ISSN: 1530-6984. DOI: 10.1021/nl500390f. URL: https://pubs.acs.org/doi/10.1021/nl500390f.

[82] Bertrand Philippe et al. “Chemical and Electronic Structure Characterization of Lead Halide Perovskites and Stability Behavior under Different Exposures—A Photoelectron Spectroscopy Investigation”. In: *Chemistry of Materials* 27.5 (Mar. 2015), pp. 1720–1731. ISSN: 0897-4756. DOI: 10.1021/acs.chemmater.5b00348. URL: https://pubs.acs.org/doi/10.1021/acs.chemmater.5b00348.

[83] Youzhen Li et al. “Degradation by Exposure of Coevaporated $CH_3NH_3PbI_3$ Thin Films”. In: *The Journal of Physical Chemistry C* 119.42 (Oct. 2015), pp. 23996–24002. ISSN: 1932-7447. DOI: 10.1021/acs.jpcc.5b07676. URL: https://pubs.acs.org/doi/10.1021/acs.jpcc.5b07676.

[84] Jinli Yang et al. “An Investigation of $CH_3NH_3PbI_3$ Degradation Rates and Mechanisms in Controlled Humidity Environments Using in Situ Techniques”. In: *ACS Nano* 9.2 (Feb. 2015), pp. 1955–1963. ISSN: 1936-0851. DOI: 10.1021/nn506864k. URL: https://pubs.acs.org/doi/10.1021/nn506864k.

[85] Aurélien M. A. Leguy et al. “Reversible Hydration of $CH_3NH_3PbI_3$ in Films, Single Crystals, and Solar Cells”. In: *Chemistry of Materials* 27.9 (May 2015), pp. 3397–3407. ISSN: 0897-4756. DOI: 10.1021/acs.chemmater.5b00660. URL: https://pubs.acs.org/doi/10.1021/acs.chemmater.5b00660.

[86] Yue Lu et al. “Surface Termination Layer Dominates the Moisture Degradation Pathway in $CH_3NH_3PbI_3$ Perovskite Film”. In: *Chemistry – A European Journal* 27.11 (Feb. 2021), pp. 3729–3736. ISSN: 0947-6539. DOI: 10.1002/chem.202003121. URL: https://chemistry-europe.onlinelibrary.wiley.com/doi/10.1002/chem.202003121.

[87] Fengzhu Li et al. “A Cation-Exchange Approach for the Fabrication of Efficient Methylammonium Tin Iodide Perovskite Solar Cells”. In: *Angewandte Chemie International Edition* 58.20 (May 2019), pp. 6688–6692. ISSN: 1433-7851. DOI: 10.1002/anie.201902418. URL: https://onlinelibrary.wiley.com/doi/10.1002/anie.201902418.

[88] Bekele Hailegnaw et al. “Rain on Methylammonium Lead Iodide Based Perovskites: Possible Environmental Effects of Perovskite Solar Cells”. In: *The Journal of Physical Chemistry Letters* 6.9 (May 2015), pp. 1543–1547. ISSN: 1948-7185. DOI: 10.1021/acs.jpclett.5b00504. URL: https://pubs.acs.org/doi/10.1021/acs.jpclett.5b00504.

[89] Ran Li et al. “Study on influencing factors and countermeasures of humidity stability of tin-lead perovskite solar cells”. In: *Nano Energy* 126.April (July 2024), p. 109664. ISSN: 22112855. DOI: 10.1016/j.nanoen.2024.109664. URL: https://linkinghub.elsevier.com/retrieve/pii/S2211285524004129.

[90] Asim Aftab and Md Imteyaz Ahmad. “A review of stability and progress in tin halide perovskite solar cell”. In: *Solar Energy* 216.October 2020 (Mar. 2021), pp. 26–47. ISSN: 0038092X. DOI: 10.1016/j.solener.2020.12.065. URL: https://linkinghub.elsevier.com/retrieve/pii/S0038092X20313244.

[91] Waldemar Kaiser et al. “Stability of Tin- versus Lead-Halide Perovskites: Ab Initio Molecular Dynamics Simulations of Perovskite/Water Interfaces”. In: *The Journal of Physical Chemistry Letters* 13.10 (Mar. 2022), pp. 2321–2329. ISSN: 1948-7185. DOI: 10.1021/acs.jpclett.2c00273. URL: https://pubs.acs.org/doi/10.1021/acs.jpclett.2c00273.

[92] Qi Wei, Youqi Ke, and Zhijun Ning. “Theoretical Study of Using Kinetics Strategy to Enhance the Stability of Tin Perovskite”. In: *ENERGY & ENVIRONMENTAL MATERIALS* 3.4 (Dec. 2020), pp. 541–547. ISSN: 2575-0356. DOI: 10.1002/eem2.12075. URL: https://onlinelibrary.wiley.com/doi/10.1002/eem2.12075.

[93] Alessandra Alberti et al. “Similar Structural Dynamics for the Degradation of $CH_3NH_3PbI_3$ in Air and in Vacuum”. In: *ChemPhysChem* 16.14 (Oct. 2015), pp. 3064–3071. ISSN: 1439-4235. DOI: 10.1002/cphc.201500374. URL: https://chemistry-europe.onlinelibrary.wiley.com/doi/10.1002/cphc.201500374.

[94] Jie Wang et al. “Profiling photo-induced degradation for operationally perovskite solar cells in space environment”. In: *Journal of Power Sources* 512.August (Nov. 2021),

p. 230520. ISSN: 03787753. DOI: 10.1016/j.jpowsour.2021.230520. URL: https://linkinghub.elsevier.com/retrieve/pii/S0378775321010211.

[95] Yan Jiang et al. "Mitigation of Vacuum and Illumination-Induced Degradation in Perovskite Solar Cells by Structure Engineering". In: *Joule* 4.5 (May 2020), pp. 1087–1103. ISSN: 25424351. DOI: 10.1016/j.joule.2020.03.017. URL: https://linkinghub.elsevier.com/retrieve/pii/S254243512030132X.

[96] Renjun Guo et al. "Degradation mechanisms of perovskite solar cells under vacuum and one atmosphere of nitrogen". In: *Nature Energy* 6.10 (Oct. 2021), pp. 977–986. ISSN: 2058-7546. DOI: 10.1038/s41560-021-00912-8. URL: https://www.nature.com/articles/s41560-021-00912-8.

[97] Michael E. Stuckelberger et al. "Effects of X-rays on Perovskite Solar Cells". In: *The Journal of Physical Chemistry C* 124.33 (Aug. 2020), pp. 17949–17956. ISSN: 1932-7447. DOI: 10.1021/acs.jpcc.0c04645. URL: https://pubs.acs.org/doi/10.1021/acs.jpcc.0c04645.

[98] Guillaume Vidon et al. "The Impact of X-Ray Radiation on Chemical and Optical Properties of Triple-Cation Lead Halide Perovskite: from the Surface to the Bulk". In: *Advanced Functional Materials* 33.45 (Nov. 2023), pp. 1–11. ISSN: 1616-301X. DOI: 10.1002/adfm.202304730. URL: https://onlinelibrary.wiley.com/doi/10.1002/adfm.202304730.

[99] Maryline Ralaiarisoa et al. "Influence of X-Ray Irradiation During Photoemission Studies on Halide Perovskite-Based Devices". In: *Small Methods* 7.11 (Nov. 2023), pp. 1–10. ISSN: 2366-9608. DOI: 10.1002/smtd.202300458. URL: https://onlinelibrary.wiley.com/doi/10.1002/smtd.202300458.

[100] Yeeun Kim et al. "Reversible Oxidative p-Doping in 2D Tin Halide Perovskite Field-Effect Transistors". In: *ACS Energy Letters* 9.4 (Apr. 2024), pp. 1725–1734. ISSN: 2380-8195. DOI: 10.1021/acsenergylett.4c00497. URL: https://pubs.acs.org/doi/10.1021/acsenergylett.4c00497.

[101] Michael Saliba et al. “How to Make over 20% Efficient Perovskite Solar Cells in Regular (n–i–p) and Inverted (p–i–n) Architectures”. In: *Chemistry of Materials* 30.13 (July 2018), pp. 4193–4201. ISSN: 0897-4756. DOI: 10.1021/acs.chemmater.8b00136. URL: https://pubs.acs.org/doi/10.1021/acs.chemmater.8b00136.

[102] John F. Moulder et al. *Handbook of X-ray Photoelectron Spectroscopy*. 1992. ISBN: 9780470014226. DOI: 10.1002/0470014229.ch22.

[103] Fred A. Stevie and Carrie L. Donley. “Introduction to x-ray photoelectron spectroscopy”. In: *Journal of Vacuum Science & Technology A: Vacuum, Surfaces, and Films* 38.6 (Dec. 2020). ISSN: 0734-2101. DOI: 10.1116/6.0000412. URL: https://pubs.aip.org/jva/article/38/6/063204/1024200/Introduction-to-x-ray-photoelectron-spectroscopy.

[104] Grzegorz Greczynski and Lars Hultman. “A step-by-step guide to perform x-ray photoelectron spectroscopy”. In: *Journal of Applied Physics* 132.1 (July 2022). ISSN: 0021-8979. DOI: 10.1063/5.0086359. URL: https://pubs.aip.org/jap/article/132/1/011101/2837063/A-step-by-step-guide-to-perform-x-ray.

[105] *U.S. National Institute of Standards and Technology (NIST) X-ray Photoelectron Spectroscopy Database*. Accessed: 2024-09-20. URL: https://srdata.nist.gov/xps/ElmComposition.

[106] J.H. Scofield. “Hartree-Slater subshell photoionization cross-sections at 1254 and 1487 eV”. In: *Journal of Electron Spectroscopy and Related Phenomena* 8.2 (Jan. 1976), pp. 129–137. ISSN: 03682048. DOI: 10.1016/0368-2048(76)80015-1. URL: https://linkinghub.elsevier.com/retrieve/pii/0368204876800151.

[107] Ajay Singh et al. “Coevaporation Stabilizes Tin-Based Perovskites in a Single Sn-Oxidation State”. In: *Nano Letters* 22.17 (Sept. 2022), pp. 7112–7118. ISSN: 1530-6984. DOI: 10.1021/acs.nanolett.2c02204. URL: https://pubs.acs.org/doi/10.1021/acs.nanolett.2c02204.

[108] Casa Software Ltd. “CasaXPS Manual 2.3.15 XPS AES ToF MS SNMS Dynamic SIMS”. In: (2009).

[109] Casa Software Ltd. *Test Peak Model: A Tool for Estimating Line Shape*. Accessed: 2024-11-12. URL: http://www.casaxps.com/casaxps-training/bgn_course/Test%20Peak%20Model.pdf.

[110] Meysam Pazoki, Anders Hagfeldt, and Tomas Edvinsson. *Characterization Techniques for Perovskite Solar Cell Materials*. Ed. by Meysam Pazoki, Anders Hagfeldt, and Tomas Edvinsson. Elsevier, 2020, pp. 1–264. ISBN: 9780128147276. DOI: 10.1016/C2017-0-01993-6. URL: https://linkinghub.elsevier.com/retrieve/pii/C20170019936.

[111] *Crystallography Open Database*. Accessed: 2024-09-06. URL: https://www.crystallography.net/cod/index.php.

[112] David J. Whitehouse. *Handbook of Surface and Nanometrology*. 2nd ed. CRC, 2010. ISBN: 9781420082012.

[113] Aubin JC M. Prot et al. "Composition variations in Cu(In,Ga)(S,Se)$_2$ solar cells: Not a gradient, but an interlaced network of two phases". In: *APL Materials* 11.10 (Oct. 2023). ISSN: 2166-532X. DOI: 10.1063/5.0165546. URL: https://pubs.aip.org/apm/article/11/10/101120/2917305/Composition-variations-in-Cu-In-Ga-S-Se-2-solar.

[114] Diego Di Girolamo et al. "Energy Distribution in Tin Halide Perovskite". In: *Solar RRL* 6.8 (Aug. 2022). ISSN: 2367-198X. DOI: 10.1002/solr.202100825. URL: https://onlinelibrary.wiley.com/doi/10.1002/solr.202100825.

[115] Kevin G. Stamplecoskie, Joseph S. Manser, and Prashant V. Kamat. "Dual nature of the excited state in organic–inorganic lead halide perovskites". In: *Energy & Environmental Science* 8.1 (2015), pp. 208–215. ISSN: 1754-5692. DOI: 10.1039/C4EE02988G. URL: https://xlink.rsc.org/?DOI=C4EE02988G.

[116] Claudiu Mortan et al. "Preparation of Methylammonium Tin Iodide ($CH_3NH_3SnI_3$) Perovskite Thin Films via Flash Evaporation". In: *physica status solidi (a)* 216.18 (Sept. 2019), p. 1900209. ISSN: 1862-6300. DOI: 10.1002/pssa.201900209. URL: https://onlinelibrary.wiley.com/doi/10.1002/pssa.201900209.

[117] Marcel Roß, Marvin B Stutz, and Steve Albrecht. "Revealing the Role of Methylammonium Iodide Purity on the Vapor-Phase Deposition Process of Perovskites". In: *Solar RRL* 6.10 (Oct. 2022), pp. 1–9. ISSN: 2367-198X. DOI: 10.1002/solr.202200500. URL: https://onlinelibrary.wiley.com/doi/10.1002/solr.202200500.

[118] Antoine Kahn. "Fermi level, work function and vacuum level". In: *Materials Horizons* 3.1 (2016), pp. 7–10. ISSN: 2051-6347. DOI: 10.1039/C5MH00160A. URL: https://xlink.rsc.org/?DOI=C5MH00160A.

[119] Evandro Martin Lanzoni et al. "The impact of Kelvin probe force microscopy operation modes and environment on grain boundary band bending in perovskite and Cu(In,Ga)Se_2 solar cells". In: *Nano Energy* 88.April (Oct. 2021), p. 106270. ISSN: 22112855. DOI: 10.1016/j.nanoen.2021.106270. URL: https://linkinghub.elsevier.com/retrieve/pii/S2211285521005255.

[120] Luis Lanzetta, Nicholas Aristidou, and Saif A. Haque. "Stability of Lead and Tin Halide Perovskites: The Link between Defects and Degradation". In: *The Journal of Physical Chemistry Letters* 11.2 (Jan. 2020), pp. 574–585. ISSN: 1948-7185. DOI: 10.1021/acs.jpclett.9b02191. URL: https://pubs.acs.org/doi/10.1021/acs.jpclett.9b02191.

[121] Norbert H. Nickel et al. "Unraveling the Light-Induced Degradation Mechanisms of $CH_3NH_3PbI_3$ Perovskite Films". In: *Advanced Electronic Materials* 3.12 (Dec. 2017), pp. 1–9. ISSN: 2199-160X. DOI: 10.1002/aelm.201700158. URL: https://onlinelibrary.wiley.com/doi/10.1002/aelm.201700158.

[122] S. Tanuma, C. J. Powell, and D. R. Penn. "Calculations of electron inelastic mean free paths. V. Data for 14 organic compounds over the 50–2000 eV range". In: *Surface and Interface Analysis* 21.3 (Mar. 1994), pp. 165–176. ISSN: 0142-2421. DOI: 10.1002/sia.740210302. URL: https://analyticalsciencejournals.onlinelibrary.wiley.com/doi/10.1002/sia.740210302.

[123] Ralph H. Petrucci et al. *General Chemistry: Principles and Modern Applications*. 11th. Toronto: Pearson, 2017. ISBN: 9780132931281.

[124] R. A. Howie, W. Moser, and I. C. Trevena. "The crystal structure of tin(II) iodide". In: *Acta Crystallographica Section B Structural Crystallography and Crystal Chemistry* 28.10 (Oct. 1972), pp. 2965–2971. ISSN: 05677408. DOI: 10.1107/S0567740872007290. URL: https://scripts.iucr.org/cgi-bin/paper?S0567740872007290.

[125] Koji Yamada et al. "Tunable Perovskite Semiconductor $CH_3NH_3SnX_3$ (X: Cl, Br, or I) Characterized by X-ray and DTA". In: *Bulletin of the Chemical Society of Japan* 84.9 (Sept. 2011), pp. 926–932. ISSN: 0009-2673. DOI: 10.1246/bcsj.20110075. URL: https://academic.oup.com/bcsj/article/84/9/926/7343370.

[126] Jianming Yang et al. "Unraveling Photostability of Mixed Cation Perovskite Films in Extreme Environment". In: *Advanced Optical Materials* 6.20 (Oct. 2018), pp. 1–8. ISSN: 2195-1071. DOI: 10.1002/adom.201800262. URL: https://onlinelibrary.wiley.com/doi/10.1002/adom.201800262.

[127] Wei-Chun Lin et al. "In situ XPS investigation of the X-ray-triggered decomposition of perovskites in ultrahigh vacuum condition". In: *npj Materials Degradation* 5.1 (Apr. 2021), p. 13. ISSN: 2397-2106. DOI: 10.1038/s41529-021-00162-9. URL: https://www.nature.com/articles/s41529-021-00162-9.

[128] Sebastian Svanström et al. "X-ray stability and degradation mechanism of lead halide perovskites and lead halides". In: *Physical Chemistry Chemical Physics* 23.21 (2021), pp. 12479–12489. ISSN: 1463-9076. DOI: 10.1039/D1CP01443A. URL: https://xlink.rsc.org/?DOI=D1CP01443A.

[129] Thomas R. Arend et al. "Physical vapor deposition of methylammonium tin iodide thin films". In: *physica status solidi (a)* 214.6 (June 2017). ISSN: 1862-6300. DOI: 10.1002/pssa.201600796. URL: https://onlinelibrary.wiley.com/doi/10.1002/pssa.201600796.

[130] *Data retrieved from the Materials Project for SnO (mp-545820) from database version v2023.11.1.* Accessed: 2024-09-12. URL: https://next-gen.materialsproject.org/p.

[131] *Data retrieved from the Materials Project for SnO_2 (mp-856) from database version v2023.11.1.* Accessed: 2024-09-12. URL: https://next-gen.materialsproject.org/p.

[132] Robert E. Huie et al. "The Atmospheric Chemistry of Iodine Monoxide". In: *Halon Replacements. Technology and Science*. American Chemical Society, 1995. Chap. 4, pp. 311–322. ISBN: 0-8412-3327-6. URL: https://www.nist.gov/system/files/documents/el/fire_research/R0000232.pdf.

[133] Mohamed Karmaoui et al. "One-Step Synthesis, Structure, and Band Gap Properties of SnO_2 Nanoparticles Made by a Low Temperature Nonaqueous Sol–Gel Technique". In: *ACS Omega* 3.10 (Oct. 2018), pp. 13227–13238. ISSN: 2470-1343. DOI: 10.1021/acsomega.8b02122. URL: https://pubs.acs.org/doi/10.1021/acsomega.8b02122.

[134] Mingyang Wei et al. "Combining Efficiency and Stability in Mixed Tin–Lead Perovskite Solar Cells by Capping Grains with an Ultrathin 2D Layer". In: *Advanced Materials* 32.12 (Mar. 2020), pp. 1–8. ISSN: 0935-9648. DOI: 10.1002/adma.201907058. URL: https://onlinelibrary.wiley.com/doi/10.1002/adma.201907058.